

This content has been downloaded from IOPscience. Please scroll down to see the full text.

Download details:

IP Address: 115.156.134.88

This content was downloaded on 03/11/2017 at 10:43

Please note that terms and conditions apply.

You may also be interested in:

Principles and Applications of Fourier Optics: Imaging systems and aberrations

R K Tyson

Principles and Applications of Fourier Optics: Enabling applications

R K Tyson

Unconventional methods of imaging: computational microscopy and compact implementations

Euan McLeod and Aydogan Ozcan

Saturated pattern-illuminated fourier ptychography microscopy

Yue Fang, Youhua Chen, Cuifang Kuang et al.

Theoretical analysis of focus wedge mark for best-focus determination in photolithography

Kyoichi Suwa, Satoshi Yashiki and Shigeru Hirukawa

Holography-techniques and applications

I Weingartner

Determination of the transfer function for optical surface topography measuring instruments--a

review

Matthew R Foreman, Claudiu L Giusca, Jeremy M Coupland et al.

Electron holography—basics and applications

Hannes Lichte and Michael Lehmann

Ultra-high resolution electron microscopy

Mark P Oxley, Andrew R Lupini and Stephen J Pennycook

Fourier Ptychographic Imaging

A MATLAB[®] tutorial

Fourier Ptychographic Imaging

A MATLAB[®] tutorial

Guoan Zheng

University of Connecticut, Storrs, CT, USA

Morgan & Claypool Publishers

Copyright © 2016 Morgan & Claypool Publishers

All rights reserved. No part of this publication may be reproduced, stored in a retrieval system or transmitted in any form or by any means, electronic, mechanical, photocopying, recording or otherwise, without the prior permission of the publisher, or as expressly permitted by law or under terms agreed with the appropriate rights organization. Multiple copying is permitted in accordance with the terms of licences issued by the Copyright Licensing Agency, the Copyright Clearance Centre and other reproduction rights organisations.

Rights & Permissions

To obtain permission to re-use copyrighted material from Morgan & Claypool Publishers, please contact info@morganclaypool.com.

ISBN 978-1-6817-4273-1 (ebook)

ISBN 978-1-6817-4272-4 (print)

ISBN 978-1-6817-4275-5 (mobi)

DOI 10.1088/978-1-6817-4273-1

Version: 20160501

IOP Concise Physics

ISSN 2053-2571 (online)

ISSN 2054-7307 (print)

A Morgan & Claypool publication as part of IOP Concise Physics

Published by Morgan & Claypool Publishers, 40 Oak Drive, San Rafael, CA, 94903, USA

IOP Publishing, Temple Circus, Temple Way, Bristol BS1 6HG, UK

To my family for all their love and support

Contents

Preface	ix
Acknowledgements	x
Author biography	xi
1 Basic concepts in Fourier optics	1-1
1.1 Coherent imaging system	1-1
1.2 Incoherent imaging system	1-4
1.3 Modeling aberrations	1-6
Bibliography	1-8
2 Imaging procedures of Fourier ptychography	2-1
2.1 Forward imaging model	2-2
2.2 Recovery process	2-6
2.3 Aberration correction in FP	2-13
2.3.1 Correcting known aberrations in FP	2-13
2.3.2 Correcting unknown aberrations in FP	2-15
2.4 Sampling requirements of FP	2-19
2.4.1 Sampling in the spatial domain	2-20
2.4.2 Sampling in the Fourier domain	2-24
2.5 Optimal updating sequence for FP: energy criteria	2-28
2.6 State-multiplexing in FP	2-30
Bibliography	2-36
3 Experimental implementations and imaging modalities of Fourier ptychography	3-1
3.1 Experimental implementations	3-1
3.1.1 LED-array illumination	3-1
3.1.2 Liquid crystal display (LCD) for illumination modulation	3-3
3.1.3 Aperture-scanning FP for holographic imaging and remote sensing	3-6
3.1.4 Other implementations	3-8
3.2 Imaging modalities of FP	3-8
3.2.1 Bright-field, phase, and phase-gradient imaging	3-8
3.2.2 Dark-field imaging	3-9

3.2.3	Reflective imaging	3-11
3.2.4	Multi-slice imaging	3-13
	Bibliography	3-13
4	Extending Fourier ptychography for incoherent imaging	4-1
4.1	Pattern-illuminated FP	4-1
4.2	Resolution doubling using 4 frames	4-7
4.3	Recovering higher dimensional data	4-10
	Bibliography	4-17
5	Summary and outlook	5-1
	Bibliography	5-3

Preface

Fourier ptychography is a new imaging technique that bypasses the resolution limit of the employed optics. In particular, it transforms the general challenge of high-throughput, high-resolution imaging from one that is coupled to the physical limitations of the optics to one that is solvable through computation. This book began as a collection of lecture notes and MATLAB® simulation examples on the Fourier ptychography technique. In teaching this technique in a graduate course, I found that the students were able to develop a better conceptual understanding using simulation examples. Following the same line of reasoning, this book demonstrates the concept of Fourier ptychography in a tutorial form and provides many MATLAB simulation examples for the reader. It also discusses the experimental implementation and recent developments of the technique. This book will be of interest to researchers and engineers learning simulation techniques for Fourier optics and the Fourier ptychography concept.

The book begins in chapter 1 with a short review of imaging concepts in Fourier optics. It provides simulation examples on coherent and incoherent imaging systems. It also covers the modeling of Zernike aberrations in imaging systems.

Chapter 2 covers the imaging procedures of the Fourier ptychography technique. In particular, it provides simulation examples on the forward imaging model, the iterative recovery process, and the aberration-correction scheme. It also discusses the sampling requirement, the optimal updating order, and the decomposition of state-mixture in Fourier ptychography.

Chapter 3 covers different experimental implementations of the Fourier ptychography technique, including the LED-array approach, the liquid-crystal-display approach, and the aperture-scanning implementation. It also discusses different coherent imaging modalities using Fourier ptychography, including bright-field, dark-field, phase, phase-gradient, reflective, and multi-slice imaging.

Chapter 4 extends the Fourier ptychography framework to incoherent imaging settings. It provides simulation examples on the pattern-illuminated Fourier ptychography scheme. It also covers the 4-frame resolution-doubling scheme and the multiplexed structured illumination approach.

Chapter 5 summarizes the book and provides the directions for future developments.

For more information on the Fourier ptychography technology, please refer to Smart Imaging Lab @ UConn: <https://sites.google.com/site/gazheng/>.

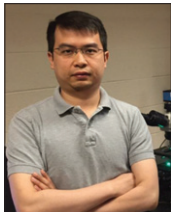
Guoan Zheng
December 2015

Acknowledgements

I would like to thank my students Siyuan Dong and Kaikai Guo for their developments of some simulation examples in this book. I would also like to thank Professor Changhuei Yang, Professor Rongguang Liang, Professor Charles DiMarzio, Dr Roarke Horstmeyer, and Dr Xiaoze Ou for their helpful discussions over the past few years. The development of the Fourier ptychography technology in my lab is currently supported by NSF CBET 1510077. Lastly and most importantly, I want to express my gratitude to my wife and my parents. I could not have finished this book without their unconditional support.

Author biography

Guoan Zheng



Dr Guoan Zheng is an Assistant Professor at University of Connecticut, with a joint appointment from the Biomedical Engineering Department and the Electrical Engineering Department. His primary field of expertise lies in microscopy, optical engineering, biophotonics, computational imaging, and lab-on-a-chip devices. His current research interests include Fourier ptychography, high-throughput imaging technologies, super-resolution imaging, phase retrieval techniques, and the development of optofluidics and chip-scale imaging solutions. He earned his MSc and PhD in Electrical Engineering from Caltech. He received the \$30 000 Lemelson-MIT Caltech Student Prize in 2011 for his development of chip-scale microscopy solutions. He got the Caltech Demetriades Thesis Prize in 2013 for his development of the Fourier ptychography technology. His research has resulted in more than 50 peer-reviewed publications and 15 issued/pending patents, four of which have been extensively reported and highlighted by national media agencies.

Fourier Ptychographic Imaging

A MATLAB® tutorial
Guoan Zheng

Chapter 1

Basic concepts in Fourier optics

In this chapter, we will briefly review the basic concepts in Fourier optics. The operation of conventional imaging systems can be modeled by two steps, as shown in figure 1.1: 1) the low-pass filtering process of the imaging system, and 2) the discrete sampling process of the image sensor.

In step 1, the employed optical system acts like a low-pass filter, with a cutoff frequency determined by the numerical aperture (NA) of the lens. Only the spatial-frequency components within the passband can be collected by the optical system and form an image at the detector plane. Such a low-pass filtering process imposes a resolution limit on the imaging platform. For coherent imaging, the resolution limit for the complex light field is λ/NA , where λ is the wavelength of the incident light. For incoherent imaging, the resolution limit for the intensity signal is $\lambda/(2NA)$.

In step 2, the light signal is sampled by the image sensor. The pixel size of the image sensor needs to satisfy the Nyquist limit, i.e., at least two samples are made for the smallest feature of the signal. If the pixel size of the image sensor is too large, it would introduce the aliasing problem to the final captured image, as shown in figure 1.1 (bottom right). A smaller pixel size of the image sensor helps to address the aliasing problem; however, it may also impose limitations on the dynamic range and the signal-to-noise ratio of the sensor chip.

In the following, we will discuss the coherent and incoherent imaging systems from the transfer-function point of view. We will also discuss how to model optical aberrations in imaging systems. Materials in this chapter are useful for understanding the concept of Fourier ptychography (FP). The interested reader can also refer to [1–3] for more details on Fourier optics.

1.1 Coherent imaging system

We first consider a coherent imaging system where a spatially coherent light source is used for sample illumination (we will refer to it as coherent illumination in the future). Under coherent illumination condition, the phasor amplitudes of the light

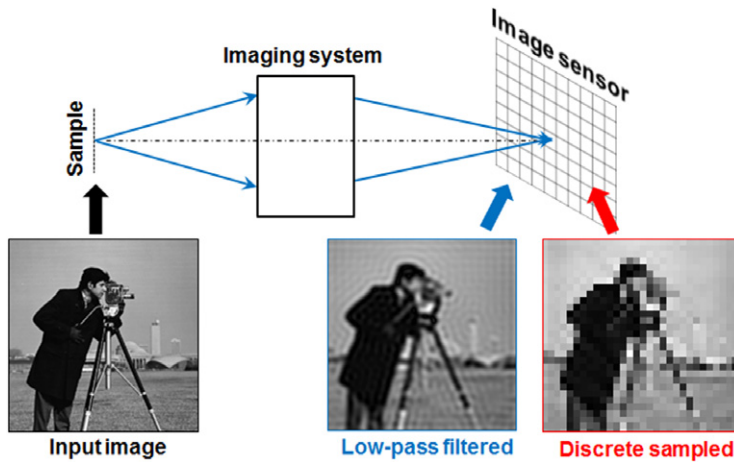


Figure 1.1. The operation of conventional imaging systems. The light field from the object (bottom left) is low-pass filtered by the imaging system (bottom middle) and discretely sampled by the image sensor (bottom right).

field vary in unison at all spatial points. Therefore, a coherent imaging system is linear in complex amplitude:

$$A_{\text{output}}(x, y) = h(x, y) \otimes A_{\text{input}}(x, y) \quad (1.1)$$

In equation (1.1), A_{input} and A_{output} represent the input and output complex amplitudes of the light field, $h(x, y)$ represents the coherent point spread function in the spatial domain, and ‘ \otimes ’ represents 2D convolution. We can transform equation (1.1) to the spatial-frequency (Fourier) domain and obtain:

$$G_{\text{coh_output}}(k_x, k_y) = H_{\text{coh}}(k_x, k_y)G_{\text{coh_input}}(k_x, k_y) \quad (1.2)$$

In equation (1.2), $G_{\text{coh_input}}$ and $G_{\text{coh_output}}$ represent the input and output Fourier spectrums of the complex amplitudes. $H_{\text{coh}}(k_x, k_y)$ is the Fourier transform of $h(x, y)$ and it is commonly referred to as coherent transfer function.

Coherent illumination condition can be obtained when the light waves come from a single point source. The common light sources for coherent illumination are laser diodes and spatially-confined LEDs. We can also add a small pinhole in front of an extended light source to obtain the coherent illumination condition (the pinhole can be treated as a single point source in this case). In this case, however, the achievable brightness would be much weaker than the case of laser diode. Strictly speaking, there is no real point source for coherent illumination; even for laser diode, the light emitting area has a certain size. Rigorous treatment of the coherent illumination condition is beyond the scope of this book. The interested reader can refer to the theory of partial coherence in [2].

To simulate the imaging process of a coherent imaging system, we consider a microscope example with a $1\times$ magnification, 0.2 NA objective lens. The incident wavelength is $0.5 \mu\text{m}$ and the final image is sampled by an image sensor with a $0.5 \mu\text{m}$ pixel size. In the following, we will first create a high-resolution input object

(lines 1–4) and set up the coherent imaging system (lines 5–9). We will then simulate the low-pass filtering process of the imaging system (lines 10–21). Finally, we will obtain the output complex amplitude and intensity images of the simulated object (lines 22–26).

```

1  %% simulate a high-resolution object
2  objectIntensity = double(imread('cameraman.tif'));
3  objectAmplitude = sqrt(objectIntensity);
4  imshow(objectAmplitude,[]);title('Input object (amplitude)');
5  %% set up the parameters for the coherent imaging system
6  waveLength = 0.5e-6;
7  k0=2*pi/waveLength;
8  pixelSize = 0.5e-6;
9  NA = 0.1; cutoffFrequency = NA*k0;
10 %% set up the low-pass filter
11 objectAmplitudeFT=fftshift(fft2(objectAmplitude));
12 [m n]=size(objectAmplitude);
13 kx=-pi/pixelSize:2*pi/(pixelSize*(n-1)):pi/pixelSize;
14 ky=-pi/pixelSize:2*pi/(pixelSize*(n-1)):pi/pixelSize;
15 [kxm kym]=meshgrid(kx,ky);
16 CTF=((kxm.^2+kym.^2)<cutoffFrequency^2); % the coherent transfer function
17 imshow(CTF,[]);title('CTF in the spatial frequency domain');
18 %% the filtering process
19 outputFT=CTF.*objectAmplitudeFT;
20 imshow(log(abs(outputFT)),[]);
21 title('Filtered spectrum in the spatial frequency domain');
22 %% output amplitude and intensity
23 outputAmplitude = ifft2(fftshift(outputFT));
24 outputIntensity = abs(outputAmplitude).^2;
25 figure;imshow(outputAmplitude,[]);
26 title('Output object (amplitude)');

```

In line 2, we simulate a high-resolution intensity object. We assume the phase of the object is a constant and we convert the intensity to complex amplitude in line 3. In lines 5–9, we set up the parameters for the coherent imaging system. In particular, we define the wave number in line 7 and the cutoff frequency in line 9. In lines 11–17, we set up the low-pass filter (i.e. the coherent transfer function) in the spatial-frequency domain. The low-pass filtering process is performed in line 19, where we transform the object's complex amplitude to the spatial-frequency domain using fast Fourier transform and multiply it with the coherent transfer function. The filtered spectrum is then transformed back to the spatial domain using the inverse fast Fourier transform in line 23. The final output amplitude and intensity can be obtained in lines 23 and 24.

The results of this simulation study are shown in figure 1.2, where we compare the input and output amplitude in both the spatial and spatial-frequency domains (spatial-frequency domain will be referred to as Fourier domain in the future). We note that, a coherent imaging system is linear in complex amplitude, and thus, the filtering process in line 19 is for the complex amplitude of the light field, not the intensity. Once we obtain the output complex amplitude, we can convert it back to intensity, as shown in line 24. We also note that, conventional image sensors can only detect light intensity; the complex phase information is lost in the measuring process. In order to detect the complex amplitude information, we can use phase retrieval [4–12] or holographic approaches [13–15] to recover the lost phase information from intensity measurements. In particular, Fourier ptychography is

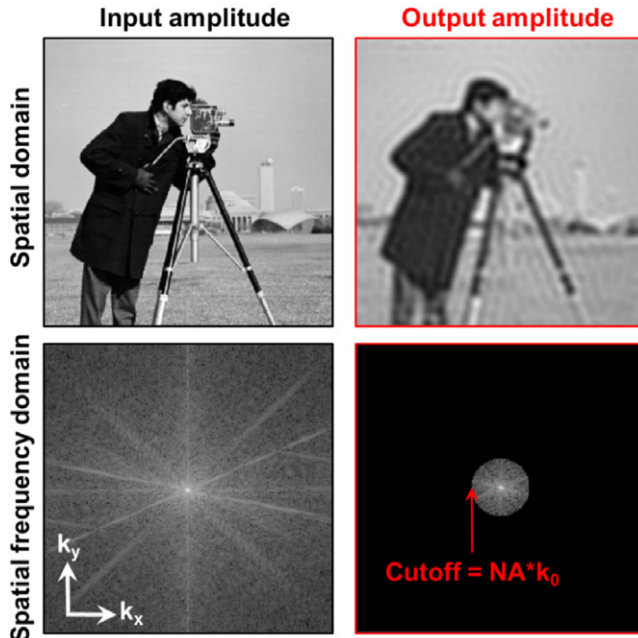


Figure 1.2. The low-pass filtering process of a coherent imaging system.

a coherent phase-retrieval approach. In the recovery process of FP, the acquired intensity images under different incident angles are used to recover the complex amplitude of the object and improve the resolution beyond the cutoff frequency of the employed optics [16].

1.2 Incoherent imaging system

In a coherent imaging system, the illumination light waves come from a point source and the phasor amplitudes of the light waves vary in unison at all spatial points. Here, we consider another illumination condition with the opposite property such that the phasor amplitudes at different points vary in a totally uncorrelated manner. Such an illumination condition is called spatially incoherent (we will simply refer to it as incoherent in the future). The most common example for incoherent imaging is the Köhler illumination in microscope settings, where samples are illuminated by uncorrelated plane waves from different incident angles.

For an incoherent imaging system, the impulse responses at different spatial points vary in an uncorrelated manner. As such, they must be added on an intensity basis instead of the complex amplitude basis. It follows that an incoherent imaging system is linear in intensity and the point spread function is the squared magnitude of the coherent point spread function:

$$I_{\text{output}}(x, y) = |h(x, y)|^2 \otimes I_{\text{input}}(x, y) \quad (1.3)$$

In equation (1.3), I_{input} and I_{output} represent the input and output intensity images, and $h(x, y)$ is the coherent point spread function in the spatial domain. The impulse

response $|h(k_x, k_y)|^2$ is commonly known as incoherent point spread function. We can also transform equation (1.3) to the Fourier domain and obtain:

$$G_{\text{incoh_output}}(k_x, k_y) = H_{\text{incoh}}(k_x, k_y) G_{\text{incoh_input}}(k_x, k_y) \quad (1.4)$$

In equation (1.4), $G_{\text{incoh_input}}$ and $G_{\text{incoh_output}}$ represent the input and output Fourier spectrums of the intensity images, and $H(k_x, k_y)$ is the Fourier transform of $|h(x, y)|^2$ and known as incoherent transfer function.

In the following, we will use the same microscope imaging example ($1\times$ magnification, 0.1 NA objective lens, 0.5 μm wavelength, and 0.5 μm pixel size) to demonstrate the incoherent imaging process. The key idea of this simulation is to generate the incoherent transfer function and perform the low-pass filtering process in the Fourier domain.

```

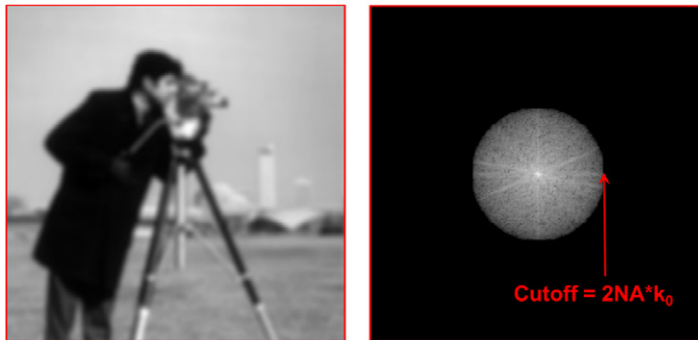
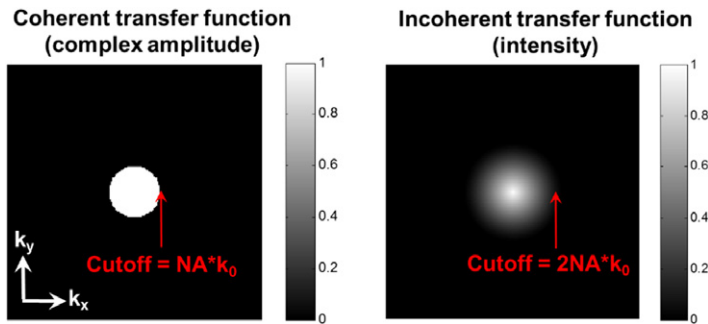
1 %% simulate an incoherent imaging system
2 objectIntensity=double(imread('cameraman.tif'));
3 imshow(objectIntensity,[],title('Input object (intensity)');
4 %% set up the parameters for the coherent imaging system
5 waveLength = 0.5e-6;
6 k0=2*pi/waveLength;
7 pixelSize = 0.5e-6;
8 NA = 0.1;
9 cutoffFrequency = NA*k0;
10 %% set up the coherent transfer function in the Fourier domain
11 objectIntensityFT=fftshift(fft2(objectIntensity));
12 [m n]=size(objectIntensity);
13 kx=-pi/pixelSize:2*pi/(pixelSize*(n-1)):pi/pixelSize;
14 ky=-pi/pixelSize:2*pi/(pixelSize*(n-1)):pi/pixelSize;
15 [kxm kym]=meshgrid(kx,ky);
16 CTF=((kxm.^2+kym.^2)<cutoffFrequency.^2); % pupil function circ(kmax)
17 imshow(CTF,[],title('Coherent transfer function in the Fourier domain');
18 %% set up the incoherent transfer function
19 cpsf=fftshift(ifft2(ifftshift(CTF))); % coherent PSF
20 ipsf=(abs(cpsf)).^2; % incoherent PSF
21 OTF=abs(fftshift(fft2(ifftshift(ipsf)))); % incoherent transfer function
22 OTF=OTF./max(max(OTF));
23 figure;imshow(abs(OTF),[]);
24 title('Incoherent transfer function in the Fourier domain');
25 %% perform low-pass filtering and generate the output intensity image
26 outputFT=OTF.*objectIntensityFT;
27 imshow(log(abs(objectIntensityFT)),[]);
28 title('Filtered spectrum in the Fourier domain');
29 outputIntensity = ifft2(ifftshift(outputFT));
30 figure;imshow(outputIntensity,[]);title('Output object (intensity)');

```

Similar to the coherent imaging case, we generate the coherent transfer function in line 16. We then transform the coherent transfer function to the spatial domain and obtain the coherent point spread function in line 19. Next, we take the squared magnitude of the coherent point spread function to obtain the incoherent point spread function in line 20. Finally, we transform the incoherent point spread function back to the Fourier domain to obtain the incoherent transfer function in line 21. The low-pass filtering process is performed in line 26, similar to the case of coherent imaging. The final low-pass filtered intensity output is obtained in line 29 and it is shown in figure 1.3.

Figure 1.4 shows the comparison between the coherent and incoherent transfer functions. We can see that the cutoff frequency of the incoherent transfer function is

Output intensity and Fourier spectrum for incoherent imaging

**Figure 1.3.** The simulated output intensity and Fourier spectrum in an incoherent imaging setting.**Figure 1.4.** The comparison between the coherent and incoherent transfer functions.

twice the cutoff frequency of the coherent transfer function. However, it does not follow that incoherent illumination yields a better resolution than coherent illumination, as we are comparing image intensity to complex amplitude. In fact, which type of illumination is better strongly depends on the sample property, and in particular on the phase distribution of the object. The interested reader can refer to chapter 6 in [1] for more details.

1.3 Modeling aberrations

In previous sections, we assume the imaging system does not contain any optical aberration. Such a system is called a diffraction-limited system, where the achievable resolution is only determined by the NA. We now consider the effect of optical aberration, which imposes practical limits on resolution performance. In particular, we will model the aberrations using the transfer-function approach. We note that, a treatment of various types of aberrations and their effects on frequency response is beyond the scope of this chapter. The interested reader can refer to, for example, [17].

To model aberrations in the imaging process, we can simply introduce a phase term in the coherent transfer function (CTF) as follows:

$$\text{CTF}(k_x, k_y) = \text{circ}(NA \cdot k_0) \cdot e^{i \cdot W(k_x, k_y)}, \quad (1.5)$$

where the circle function ‘circ’ generates a circular mask with a radius of $NA \cdot k_0$, and $W(k_x, k_y)$ represents the wavefront aberration of the system. We can further decompose the wavefront aberration into a summation of different Zernike modes $Z(m, n)$ as follows:

$$W(k_x, k_y) = \sum a_{(m,n)} Z(m, n), \quad (1.6)$$

where $a_{(m,n)}$ represents the coefficient for the Zernike mode $Z(m, n)$. As an example, we have the second-order defocus aberration $W(k_x, k_y) = a_{(2,0)}Z(2, 0)$, where $a_{(2,0)}$ represents the amount of defocus aberration. Similarly, $a_{(2,2)}$ and $a_{(2,-2)}$ represent the amounts of second-order astigmatism aberrations along two directions; $a_{(3,1)}$ and $a_{(3,-1)}$ represent the amounts of third-order coma aberrations along two directions; $a_{(4,0)}$ represents the amount of fourth-order spherical aberration. In short, equations (1.5) and (1.6) provide a means to model different aberrations in the imaging process. In the simulation code, we only need to add the following lines to model them in the coherent transfer function:

```

1   W = 2*gzn(pixelNumber,pixelNumberAperture,2,0) +
     4*gzn(pixelNumber,pixelNumberAperture,4,0);
2   CTF=exp(i.*W).*((kxm.^2+kym.^2)<cutoffFrequency^2);
3   imshow(angle(CTF),[]);title('Coherent transfer function with aberrations');

```

In line 1, we model the wavefront aberration $W(k_x, k_y)$ as the summation of the second-order defocus and the fourth-order spherical aberrations. We use the ‘gzn’ function to generate different Zernike modes (similar Zernike functions can be found on the MATLAB File Exchange site). This function takes four parameters from left to right: the width of the input image, the diameter of the pupil aperture, and the two indexes of the Zernike mode. In particular, we have $a_{(2,0)} = 2$ and $a_{(4,0)} = 4$ in the simulation code. In line 2, we model the coherent transfer function using equation (1.5). Once we get the coherent transfer function with aberrations, we can use the coherent imaging procedures in section 1.1 to obtain the output complex amplitude.

To model aberrations in an incoherent imaging system, we need to convert the coherent transfer function (with aberrations) to the incoherent transfer function using the procedures in section 1.2. We can then apply the incoherent transfer function in the filtering process to generate the output intensity image. In figure 1.5, we show two different aberrations in the Fourier domain and their corresponding coherent and incoherent outputs. We can see that the achievable resolution degrades when wavefront aberrations are presented in the imaging system.

Aberration plays a critical role in the design of an imaging platform. As an example, a conventional microscope has a tradeoff between resolution and field of view. A better resolution usually implies a smaller field of view, limiting the imaging throughput of the microscope platform. The tradeoff between resolution and field of view, in fact, comes from aberrations of the objective lens. The common strategy to expand the field of view is to scale up the lens’s size [18]. However, simple

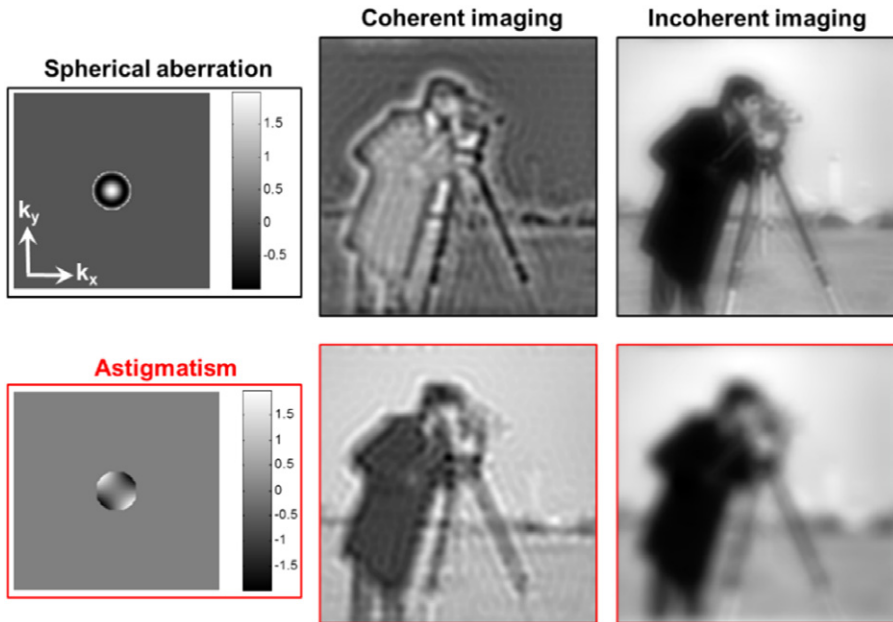


Figure 1.5. Modeling aberrations in the coherent and incoherent imaging systems. Top row: the simulated coherent and incoherent images with spherical aberration ($a_{(4,0)}=2$). Bottom row: the simulated coherent and incoherent images with astigmatism aberration ($a_{(2,2)}=4$).

size-scaling would introduce aberrations to the system. To compensate for these aberrations, we need to introduce more optical surfaces to increase the degrees of freedom in lens optimization. With the optomechanical constraints of a conventional microscope platform, expanding field of view without compromising the achievable resolution is considered very challenging in the design of high-resolution objective lenses.

Bibliography

- [1] Goodman J W 2005 *Introduction to Fourier optics* (Austin, TX: Roberts and Company)
- [2] Goodman J W 2015 *Statistical optics* (Wiley: New York)
- [3] Voelz D G 2011 *Computational fourier optics: a MATLAB tutorial* (Bellingham, WA: SPIE Optical Engineering Press)
- [4] Fienup J R 1982 Phase retrieval algorithms: a comparison *Appl. Opt.* **21** 2758–69
- [5] Elser V 2003 Phase retrieval by iterated projections *JOSA A* **20** 40–55
- [6] Faulkner H M L and Rodenburg J M 2004 Movable aperture lensless transmission microscopy: A novel phase retrieval algorithm *Phys. Rev. Lett.* **93** 023903
- [7] Maiden A M and Rodenburg J M 2009 An improved ptychographical phase retrieval algorithm for diffractive imaging *Ultramicroscopy* **109** 1256–62
- [8] Gonsalves R 1976 Phase retrieval from modulus data *JOSA* **66** 961–4
- [9] Fienup J R 1987 Reconstruction of a complex-valued object from the modulus of its Fourier transform using a support constraint *JOSA A* **4** 118–23

- [10] Candes E J, Strohmer T and Voroninski V 2013 Phaselift: Exact and stable signal recovery from magnitude measurements via convex programming *Comm. Pure Appl. Math.* **66** 1241–74
- [11] Candes E J, Eldar Y C, Strohmer T and Voroninski V 2015 Phase retrieval via matrix completion *SIAM Review* **57** 225–51
- [12] Waldspurger I, d'Aspremont A and Mallat S 2015 Phase recovery, maxcut and complex semidefinite programming *Math. Program.* **149** 47–81
- [13] Schnars U and Jueptner W 2005 *Digital Holography* (Berlin: Springer)
- [14] Cuche E, Marquet P and Depeursinge C 2000 Spatial filtering for zero-order and twin-image elimination in digital off-axis holography *Appl. Opt.* **39** 4070–75
- [15] Yamaguchi I and Zhang T 1997 Phase-shifting digital Holography *Opt. Lett.* **22** 1268–70
- [16] Zheng G, Horstmeyer R and Yang C 2013 Wide-field, high-resolution Fourier ptychographic microscopy *Nature Photonics* **7** 739–45
- [17] Williams C S and Becklund O A 1989 *Introduction to the optical transfer function* vol. 112 (Bellingham, WA: SPIE Optical Engineering Press)
- [18] Lohmann A W 1989 Scaling laws for lens systems *Appl. Opt.* **28** 4996–98

Fourier Ptychographic Imaging

A MATLAB® tutorial
Guoan Zheng

Chapter 2

Imaging procedures of Fourier ptychography

In imaging system design, we use an important concept called space-bandwidth product (SBP) to characterize the total resolvable pixels of the system [1]. SBP represents the information content transmitted by the imaging system and it can be calculated based on the total imaging area and the smallest resolvable feature size. The SBPs of conventional microscope platforms are on the order of 10 megapixels, regardless of the magnification factors or numerical apertures (NAs) of the employed objective lens. As an example, a standard 20 \times , 0.4 NA Olympus microscope objective lens has a resolution of \sim 0.8 μm and an imaging field of view 1.1 mm in diameter, corresponding to a SBP of approximately 8 megapixels. To increase the SBP, one can scale up the size of the lens to increase the imaging field of view. However, as the size of a lens increases, so does its associated optical aberrations. It follows that we need to introduce more optical surfaces to increase the degrees of freedom in lens optimization. One example for achieving high SBP by scaling up the size is the photolithography system in the semiconductor industry. Such systems have a large field of view and high resolution for projecting patterns on silicon wafer. However, they are expensive to produce, difficult to align, and impractical for microscopy applications.

The original motivation of Fourier ptychography (FP) was to tackle the SBP problem from the computational imaging perspective. FP brings together two innovations in classical optics to bypass the SBP barrier of conventional microscope platforms [2–4]. The first innovation is the phase retrieval technique [5–13] originally developed for electron imaging. It is well known that light detectors, such as CCDs and photographic plates, can only measure intensity variations of the light wave. Phase information, which is related to how much the light wave is delayed through propagation, is lost during the recording process. To address this problem, phase retrieval technique is used to recover the lost phase information using intensity-only measurements. As with many inverse problems, a common formulation of phase retrieval is to seek a solution that is consistent with intensity

measurements. It typically consists of alternating enforcement of the known information of the object in the spatial and/or Fourier domains. The second innovation employed in FP is the aperture synthesis technique [14–20]. This technique was originally developed for radio astronomy, aiming at bypassing the resolution limit of a single radio telescope [21]. The basic idea of this technique is to combine images from a collection of telescopes in the Fourier domain to improve the resolution. However, the data fusion process of this technique requires the knowledge of both intensity and phase information of the incoming light wave. In the optical region, most synthetic-aperture implementations employ delicate interferometry setups for complex light field recording and precise mechanical actuations, imposing a challenge for microscopy applications [14, 15, 17, 18, 20, 22–30].

By integrating the phase retrieval and aperture synthesis techniques, FP facilitates microscopy imaging well beyond the cutoff frequency of the employed objective lens. The recovered complex image using FP contains both the intensity and phase information of the sample, a complete picture of the entire light field. A typical FP platform consists of an LED matrix and a conventional microscope with a low-NA objective lens, as shown in figure 2.1. The use of low-NA objective lens allows a large field-of-view to be captured at the expense of low spatial resolution. The LED matrix, on the other hand, is used to successively illuminate the sample from multiple angles. At each illumination angle, FP records a low-resolution sample image through the low-NA objective lens. The objective's coherent transfer function imposes a well-defined constraint in the Fourier domain. This constraint is digitally panned across the Fourier space to reflect the angular variation of its illumination. FP converges to a high-resolution complex sample solution by alternatively constraining its amplitude to match the acquired low-resolution image sequence, and its spectrum to match the panning Fourier constraint. Therefore, by simply adding an LED matrix to a conventional microscope, FP is able to transform it into a high-resolution, wide field-of-view microscope with a scalable SBP that is orders of magnitude higher than that of the employed objective lens.

In the following, we will first discuss the forward imaging model of FP (section 2.1). We will then discuss the recovery process (section 2.2), the aberration-correction process (section 2.3), the sampling requirements (section 2.4), the optimal updating sequence (section 2.5), and the state-multiplexed scheme (section 2.6) in FP.

2.1 Forward imaging model

In the forward imaging model of FP, we capture multiple intensity images of the sample under different incident angles. This process can be modeled as a coherent imaging process as follows:

$$A_{\text{output}}(x, y) = h(x, y) \otimes (A_{\text{object}}(x, y)e^{ik_{xn}x + ik_{yn}y}) \quad (2.1)$$

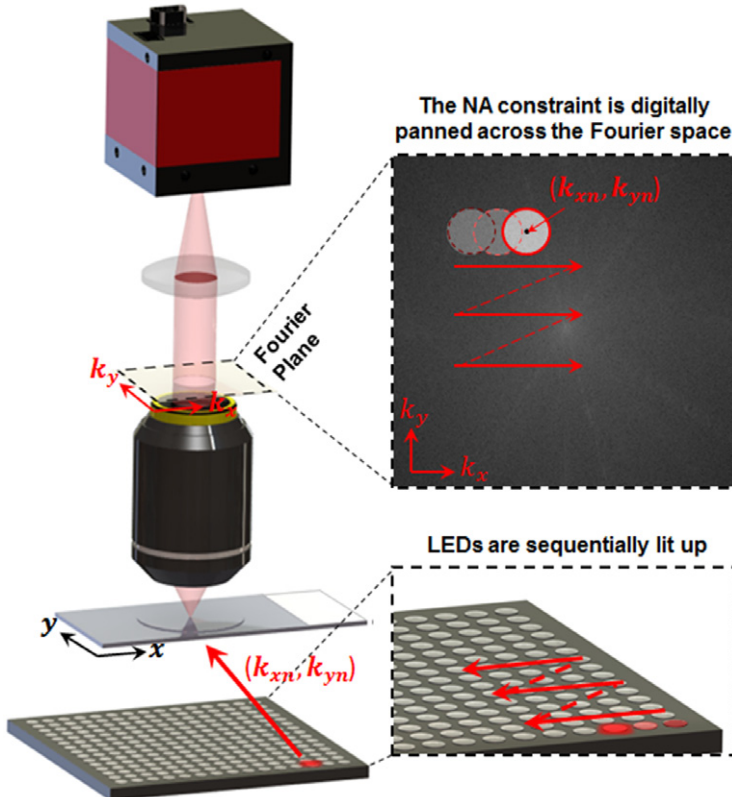


Figure 2.1. The setup and operation of the Fourier ptychographic microscope prototype. An LED array sequentially illuminates the sample with angle-varied plane waves. The constraint from the objective’s coherent transfer function is digitally panned across the Fourier space to reflect the angular variation of its illumination. Adapted from [31].

In equation (2.1), A_{object} represents the complex amplitude of the object, A_{output} represents the output complex signal of the microscope system, $h(x, y)$ represents the coherent point spread function in the spatial domain, and ‘ \otimes ’ represents the 2D convolution. The term $e^{ik_{xn}x+ik_{yn}y}$ represents the incident plane wave with a wave vector (k_{xn}, k_{yn}) . We can also transform equation (2.1) to the Fourier domain and obtain:

$$G_{\text{output}}(k_x, k_y) = H_{\text{coh}}(k_x, k_y)G_{\text{object}}(k_x - k_{xn}, k_y - k_{yn}) \quad (2.2)$$

In equation (2.2), G_{object} represents the object spectrum in the Fourier domain, G_{output} represents the output spectrum of the microscope platform, and $H_{\text{coh}}(k_x, k_y)$ is the coherent transfer function of the microscope platform. We

note that, the multiplication of $e^{ik_{xn}x+ik_{yn}y}$ in the spatial domain is equivalent to shifting the object spectrum by the amount of (k_{xn}, k_{yn}) in the Fourier domain. Therefore, we see a shifted spectrum in the right hand side of equation (2.2). We also note that we assume the sample to be a 2D thin layer in equations (2.1) and (2.2). Only under this assumption can the captured low-resolution images under different incident angles be uniquely mapped to different passbands in the Fourier domain.

In the following, we will simulate the forward imaging process of FP using MATLAB. We will first generate a high-resolution complex image as our object (lines 1–7). We will then generate the incident wave vector for the LED matrix (lines 8–22). Lastly, we will produce the output image using the low-pass filtering process of equation (2.2) (lines 23–51).

In lines 1–7, we generate a high-resolution complex image as our input object. We use the ‘camera man’ as the input amplitude and an aerial view image as the input phase, as shown in figure 2.2. The size of the complex input object is 256 by 256.

```

1  %% simulate the forward imaging process of Fourier ptychography
2  % simulate the high resolution complex object
3  objectAmplitude = double(imread('cameraman.tif'));
4  phase = double(imread('westconcordorthophoto.png'));
5  phase = pi*imresize(phase,[256 256])./max(max(phase));
6  object = objectAmplitude.*exp(li.* phase);
7  imshow(abs(object),[]);title('Input complex object');

```

In lines 8–22, we generate the wave vectors for the LED matrix. As shown in figure 2.3, the LED matrix in this simulation contains 15 by 15 elements. Line 12 defines the distance between adjacent LED elements. Line 13 defines the distance between the LED matrix and the sample. The ‘for loop’ in line 15 generates the spatial positions of the LED elements. Lines 21 and 22 generate the incident wave vectors for the 15 by 15 LED elements, assuming the object is placed at the $(0, 0)$ position.

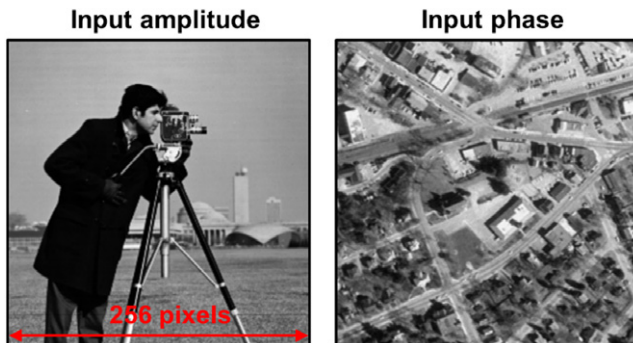


Figure 2.2. The simulated input amplitude and phase of the high-resolution object.

```

8 %% create the wave vectors for the LED illumination
9 arraysize = 15; % size of LED array
10 xlocation = zeros(1,arraysize^2);
11 ylocation = zeros(1,arraysize^2);
12 LEDgap = 4; % 4mm between adjacent LEDs
13 LEDheight = 90; % 90 mm between the LED matrix and the sample
14
15 for i=1:arraysize % from top left to bottom right
16     xlocation(1,1+arraysize*(i-1):15+arraysize*(i-1))
17         = (- (arraysize-1)/2:1:(arraysize-1)/2)*LEDgap;
18     ylocation(1,1+arraysize*(i-1):15+arraysize*(i-1))
19         = ((arraysize-1)/2-(i-1))*LEDgap;
20 end;
21 kx_relative = -sin(atan(xlocation/LEDheight)); % create kx, ky wavevectors
22 ky_relative = -sin(atan(ylocation/LEDheight));

```

Once we generate the wave vectors of the incident waves, we can perform the coherent imaging process using equation (2.2). In lines 23–28, we define the coherent imaging system. In particular, we define two pixel sizes:

- 1) the sampling pixel size of the image sensor (i.e. the pixel size of the employed CCD), and
- 2) the pixel size of the final reconstructed super-resolution image.

Similarly, we need to deal with two types of image dimensions in this coherent imaging process:

- 1) the high-resolution input image with a dimension of 256 by 256 pixels, and
- 2) the low-resolution output with a dimension of 64 by 64 pixels. In lines 31–33, we initialize the low-resolution output ‘imSeqLowRes’, which is an image stack with the dimensions of 64 by 64 by 225.

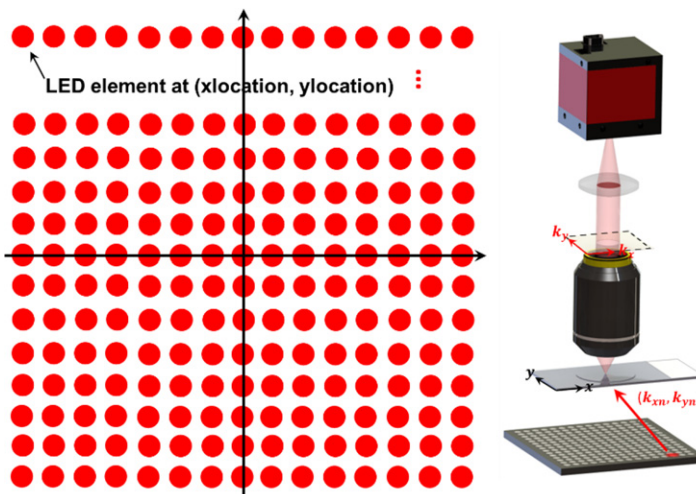


Figure 2.3. The LED matrix in the simulation. We use ‘xlocation’ and ‘ylocation’ to determine the position of each LED element. The incident wave vectors can be calculated based on the LED positions.

In particular, we use ‘imSeqLowRes’ to store the simulated low-resolution output images corresponding to the 225 different LED elements. In line 41, we define the coherent transfer function of the coherent imaging system. In the ‘for loop’ of line 43, we generate the filtered low-resolution images for different LED elements using equation (2.2). We note that there is a scaling factor in line 48. This factor is used to normalize the Fourier magnitude when changing the image size. In line 49, we take the absolute value of the output complex signal, as we lose the phase information in the recording process.

```

23 %% setup the parameters for the coherent imaging system
24 wavelength = 0.63e-6;
25 k0 = 2*pi/wavelength;
26 spsize = 2.75e-6; % sampling pixel size of the CCD
27 psize = spsize / 4; % final pixel size of the reconstruction
28 NA = 0.08;
29 %% generate the low-pass filtered images
30 [m,n] = size(object); % image size of the high resolution object
31 m1 = m/(spsize/psize);
32 n1 = n/(spsize/psize); % image size of the final output
33 imSeqLowRes = zeros(m1, n1, arraysize^2); % output low-res image sequence
34 kx = k0 * kx_relative;
35 ky = k0 * ky_relative;
36 dkx = 2*pi/(psize*n);
37 dky = 2*pi/(psize*m);
38 cutoffFrequency = NA * k0;
39 kmax = pi/spsize;
40 [kxm kym]
    = meshgrid(-kmax:kmax/((n1-1)/2):kmax,-kmax:kmax/((n1-1)/2):kmax);
41 CTF = ((kxm.^2+kym.^2)<cutoffFrequency^2); % coherent transfer function
42 objectFT = fftshift(fft2(object));
43 for tt = 1:arraysize^2
44     kxc = round((n+1)/2+kx(1,tt)/dkx);
45     kyc = round((m+1)/2+ky(1,tt)/dky);
46     kyl=round(kyc-(m1-1)/2);kyh=round(kyc+(m1-1)/2);
47     kxl=round(kxc-(n1-1)/2);kxh=round(kxc+(n1-1)/2);
48     imSeqLowFT = (m1/m)^2 * objectFT(kyl:kyh,kxl:kxh).*CTF;
49     imSeqLowRes(:,:,tt) = abs(ifft2(fftshift(imSeqLowFT)));
50 end;
51 figure;imshow(imSeqLowRes(:,:,1),[]);

```

Figure 2.4 shows the simulated output images corresponding to the first, the 113, and the 225 LED elements. We note that, the output image has a dimension of 64 by 64 pixels, 4 times lower than that of the input image in each dimension. The output image only contains the amplitude information, and the phase information is lost in the recording process. The goal of FP is to recover the high-resolution complex object using the low-resolution intensity measurements shown in figure 2.4.

2.2 Recovery process

The recovery process of FP follows the strategy of the phase retrieval technique: seeking a high-resolution sample estimate that is consistent with N low-resolution measurements. The algorithm switches between the spatial and Fourier domains of the sample estimate. In the spatial domain, the low-resolution intensity measurements are used as object constraints to ensure solution convergence. In the Fourier

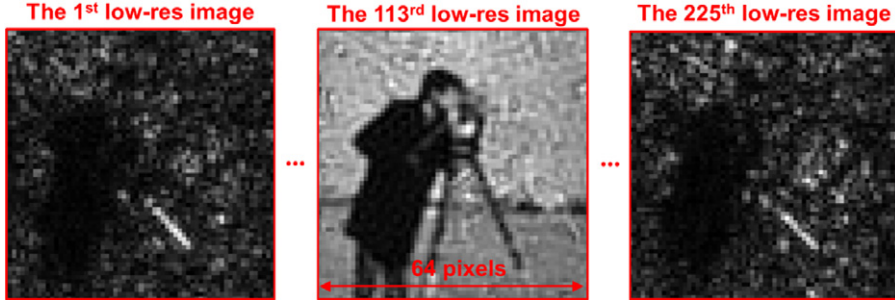


Figure 2.4. The simulated output low-resolution images. These images contain 64 by 64 pixels. The phase information is lost in the recording process.

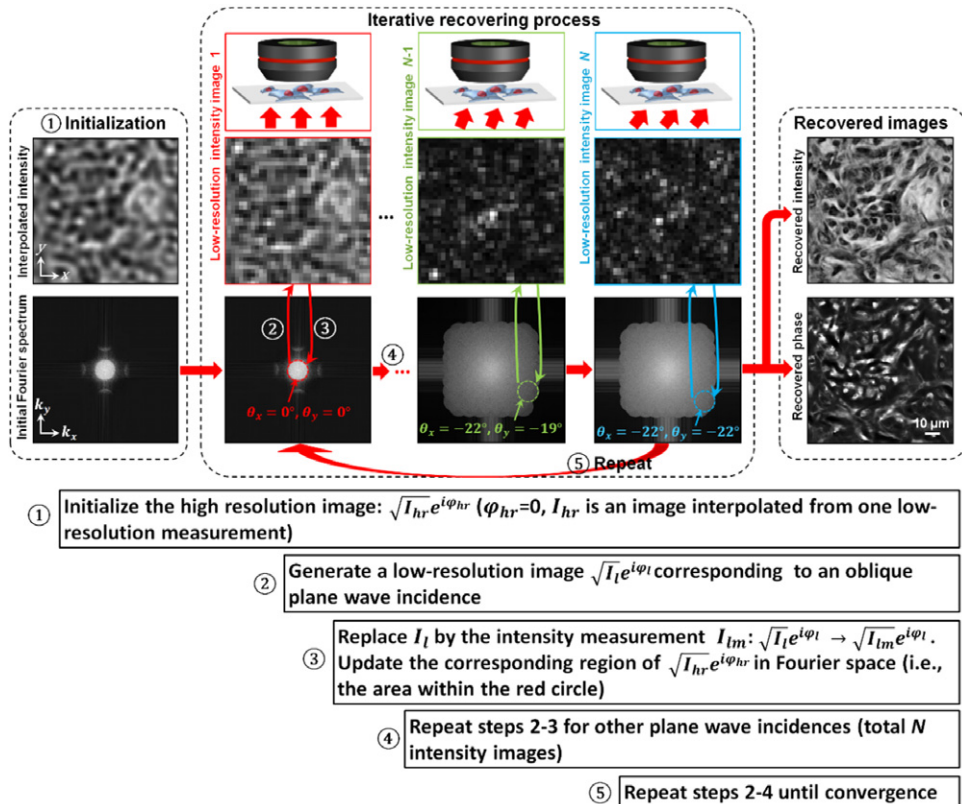


Figure 2.5. The recovery process of FP. Adapted from [2].

domain, the confined coherent transfer function of the objective lens is imposed as the support constraint. The recovery process of FP is summarized in figure 2.5 [2] and the Matlab code is provided in lines 52–76.

First (lines 54–55), the FP method makes an initial guess of the high-resolution object in the spatial domain, $\sqrt{I_h} e^{i\varphi_h}$. This initial guess is then transformed to the Fourier domain.

Second (lines 60–65), we select a small sub-region of the initial guess's Fourier spectrum, equivalent to a low-pass filter of the coherent imaging system, and apply the inverse Fourier transformation to generate a low-resolution target image $\sqrt{I_l}e^{ip_l}$. The position of the low-pass filter is selected to correspond to a particular angle of illumination. For example, the sub-region enclosed by the red circle in figure 2.5 corresponds to an image collected under the normal incident angle ($k_{x1} = 0, k_{y1} = 0$). In lines 60–63 of the simulation code, we define the sub-region of the initial guess's Fourier spectrum. In line 64, we multiply this selected spectrum with the low-pass filter. In line 65, we convert the filtered spectrum back to the spatial domain and generate the low-resolution target image.

Third (lines 66–70), following phase retrieval concepts, we replace the target image's amplitude component $\sqrt{I_l}$ with the square root of the low-resolution measurement obtained under illumination angle $i, \sqrt{I_m}$, to form an updated, low-resolution target image $\sqrt{I_m}e^{ip_l}$. We then apply Fourier transformation to this updated target image and replace its corresponding sub-region of the sample estimate's Fourier spectrum. In other words, for $i = 1$, we update the area enclosed by the red circle in figure 2.5 with image $I_m(k_{x1}, k_{y1})$, where $k_{x1} = 0, k_{y1} = 0$. In lines 66–67 of the simulation code, we replace the target image's amplitude with the low-resolution measurement. In line 68, we transform the updated target image back to Fourier domain. In lines 69–70, we update the corresponding region of the sample estimate's Fourier spectrum.

Fourth (line 58), we repeat steps 2 and 3 for different incident angles (select a small, circular region of the Fourier space and update it with measured image data). Examples are represented by the green and blue circles in figure 2.5. Each shifted sub-region corresponds to a unique, low-resolution intensity measurement $I_m(k_{xi}, k_{yi})$, and each sub-region must overlap with neighboring sub-regions to assure convergence. This iterative updating process continues for all N images, at which point the entire high-resolution image in the Fourier space has been modified with all low-resolution intensity measurements.

Lastly (line 57), steps 2–4 are repeated until a self-consistent solution is achieved (we typically repeat these steps 2–5 times). At the end of this iterative recovery process (lines 73–76), the converged solution in the Fourier space is transformed back to the spatial domain to recover a high-resolution field $\sqrt{I_h}e^{ip_h}$, offering an accurate image of the 2D complex sample (figure 2.5, right) with a dramatically increased SBP (high-resolution and wide-FOV).

```

52 %% recover the high resolution image
53 seq = gseq(arraysize); % define the order of recovery, we start from the
    % center (the 113rd image) to the edge of the spectrum (the 225th image)
54 objectRecover = ones(m,n); %% initial guess of the object
55 objectRecoverFT = fftshift(fft2(objectRecover));
56 loop = 5;
57 for tt=1:loop
58     for i3=1:arraysize^2

```

```

59         i2=seq(i3);
60         kxc = round((n+1)/2+kx(1,i2)/dkx);
61         kyc = round((m+1)/2+ky(1,i2)/dky);
62         kyl=round(kyc-(m1-1)/2);kyh=round(kyc+(m1-1)/2);
63         kxl=round(kxc-(n1-1)/2);kxh=round(kxc+(n1-1)/2);
64         lowResFT = (m1/m)^2 * objectRecoverFT(kyl:kyh,kxl:kxh).*CTF;
65         im_lowRes = ifft2(ifftshift(lowResFT));
66         im_lowRes = (m/m1)^2 *imSeqLowRes(:,:,i2)
67         .*exp(li.*angle(im_lowRes));
68         lowResFT=fftshift(fft2(im_lowRes)).*CTF;
69         objectRecoverFT(kyl:kyh,kxl:kxh)=
70             (1-CTF).*objectRecoverFT(kyl:kyh,kxl:kxh) + lowResFT;
71     end;
72 end;
73 objectRecover=ifft2(ifftshift(objectRecoverFT));
74 figure;imshow(abs(objectRecover),[]);title('test');
75 figure;imshow(angle(objectRecover),[]);
76 figure;imshow(log(objectRecoverFT),[]);

```

In the MATLAB code above, we use a function ‘gseq’ (lines 53 and 59) to configure the updating sequence of the reconstruction. In this example, we start with the image corresponding to the center of the Fourier spectrum (the 113 image), and end with the image corresponding to the edge of the spectrum (the 225 image). The reason of this updating sequence will be explained in section 2.5. The ‘gseq’ function is provided as follows:

```

1  function seqf=gseq(arraysize)
2      n=(arraysize+1)/2;
3      arrayszie=2*n-1;
4      sequence=zeros(2,arraysize^2);
5      sequence(1,1)=n;sequence(2,1)=n;
6      dx=+1;dy=-1;stepx=+1;stepy=-1;
7      direction=+1;counter=0;
8      for i=2:arraysize^2
9          counter=counter+1;
10         if (direction==+1)
11             sequence(1,i)=sequence(1,i-1)+dx;
12             sequence(2,i)=sequence(2,i-1);
13             if (counter==abs(stepx))
14                 counter=0;direction=direction*-1;
15                 dx=dx*-1;stepx=stepx*-1;
16                 if stepx>0
17                     stepx=stepx+1;
18                 else
19                     stepx=stepx-1;
20                 end
21             end
22         else
23             sequence(1,i)=sequence(1,i-1);
24             sequence(2,i)=sequence(2,i-1)+dy;
25             if (counter==abs(stepy))
26                 counter=0;direction=direction*-1;
27                 dy=dy*-1;stepy=stepy*-1;
28                 if (stepy>0)
29                     stepy=stepy+1;
30                 else
31                     stepy=stepy-1;
32                 end
33             end
34         end
35     end
36     seq=(sequence(1,:)-1)*arraysize+sequence(2,:);
37     seqf(1,1:arraysize^2)=seq;
38 end

```

Figure 2.6 shows the recovered complex image using the FP procedures. We can see that, the FP method is able to expand the passband in the Fourier domain and improve the achievable resolution well-beyond the cutoff frequency of the employed objective lens. In figure 2.6, we also show the Fourier spectrum of the recovered image and the red circle represents the size of the coherent transfer aperture.

The final resolution of FP is determined by the largest incident angle from the LED matrix, not the NA of the employed objective lens. In figure 2.7, we demonstrate the FP reconstructions using different numbers of LED elements. In this experiment, we used a $2\times$, 0.08 NA objective lens to acquire images of the sample. Different numbers of LED elements (with different illumination NAs) were used for sample illumination. We can see that the final synthetic spectrum is

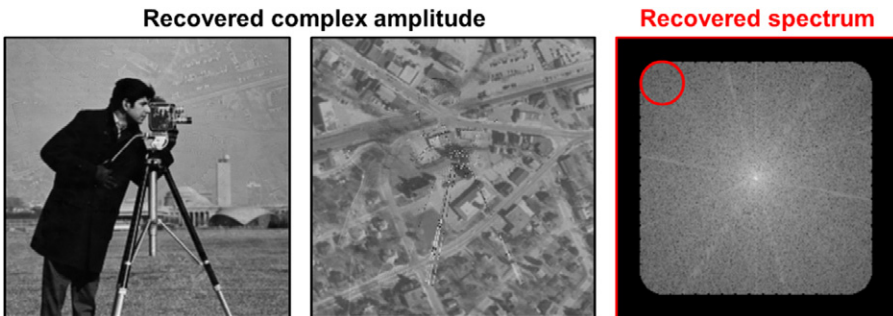


Figure 2.6. The recovered high-resolution complex image using the FP procedures.

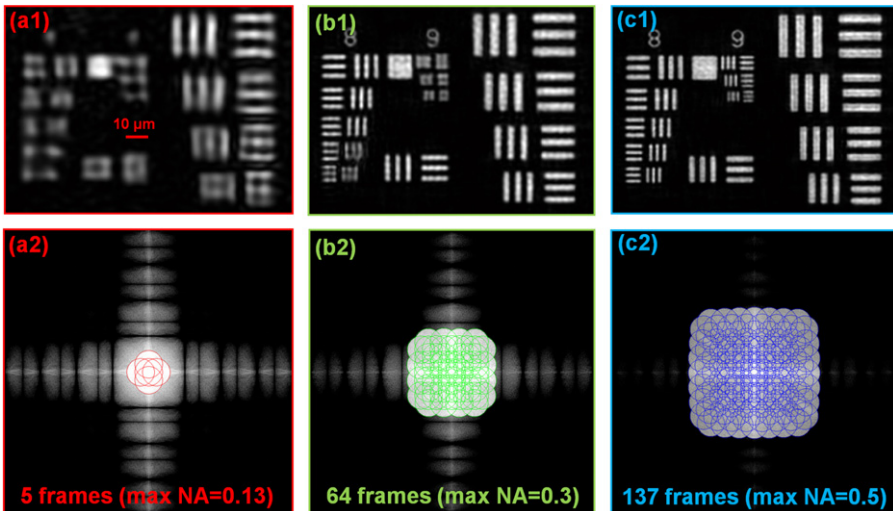


Figure 2.7. FP reconstructions using different numbers of LED elements. (a) A reconstruction using 5 input images, with a maximum synthetic NA of 0.13. (b) A reconstruction using 64 input images, with a maximum synthetic NA of 0.3. (c) A reconstruction using 137 input images, with a maximum synthetic NA of 0.5. Each small circle in (a2)–(c2) represents the spectrum region corresponding to one low-resolution input image.

determined by the number of LED elements, not the NA of the employed objective lens. Therefore, the FP approach is able to decouple the achievable resolution from the employed optics, and we can use low-NA lenses to achieve both high-resolution and wide-field-of-view imaging capabilities at the same time.

Drawing connections and distinctions between the iterative recovery process of FP and the related imaging modalities helps to clarify the concept and operation of FP. The name ‘Fourier ptychography’ comes from a related imaging modality, ptychography (we call it real-space ptychography for clarity) [33]. Real-space ptychography is a lensless phase retrieval technique that was originally proposed for transmission electron microscopy [34] and brought to fruition by Rodenburg [7, 35, 36]. It uses a focused coherent beam to illuminate the sample and repeatedly records its far-field diffraction pattern (i.e., Fourier spectrum) as the sample is mechanically scanned to different positions. The captured diffraction patterns are then used to recover the complex sample image. To this end, both FP and real-space ptychography seek for a complex solution that is consistent with many intensity measurements. With real-space ptychography, the finite aperture support constraint is imposed in the spatial domain and the magnitude constraint is imposed in the Fourier domain. FP, on the other hand, switches the spatial domain and the Fourier domain by using a lens [2, 4, 37]. With FP, the intensity images are captured in the spatial domain and the aperture constraint is imposed by the confined coherent transfer function in the Fourier domain [2]. To this end, FP appears as the Fourier counterpart of the real-space ptychography, justifying its name.

By employing a lens to switch the spatial and Fourier domain, FP has several unique advantages (we will further discuss some of these advantages in later chapters):

- 1) FP reduces the requirement of spatial coherence as the images are captured in spatial domain [4]. In FP, we only need to maintain the spatial coherence over the scale of the point spread function at the object plane. As such, we can use partially coherent LED illumination in FP settings. In real-space ptychography, on the other hand, we need to maintain the spatial coherence over the entire image detector. Thus, real-space ptychography requires the use of laser or other coherent sources. The possibility of using a partially coherent light source in FP may be important for imaging modalities where high spatial coherence is difficult to achieve, such as x-ray and electron microscopy.
- 2) By scanning the aperture in the Fourier domain, FP is able to recover an image with a resolution beyond the frequency limit of the employed lens. Aperture scanning in the Fourier domain can be implemented by using a simple LED array for angle-varied illumination, and thus, no mechanical scanning is needed in an optical FP platform. As we will discuss later, aberrations of the employed objective lens can be modeled as a pupil function in FP [38, 39] and it can be digitally corrected in the iterative recovery process. As one application, we can introduce a second-order Zernike function in the recovery process to compensate for the defocus aberration. By doing so, we can extend the depth of field of a microscopy

platform by ~ 75 folds [2]. Since aberrations can be corrected in the FP recovery process, low quality optics can also be used to achieve high-resolution imaging performance [40].

- 3) The Fourier spectrum of an image typically has a very high dynamic range. The signal strength at the center of the Fourier spectrum is typically orders of magnitude higher than that at the edge. As a result, real-space ptychography requires a detector with a very high dynamic range for capturing diffraction patterns at the Fourier space. FP, on the other hand, directly captures images in the spatial domain. The overall signal strength only changes when the sample is illuminated with a different incident angle. We can, thus, simply adjust the exposure time of the detector to accommodate the change of the signal strength in FP imaging settings [41]. In addition, the sampling overlap in FP can be adjusted in the Fourier space according to the energy level of the sample's Fourier spectrum [41, 42]. The sampling overlap for real-space ptychography, on the other hand, needs to be uniform in the spatial domain and cannot be adapted to the spatial features of the object [43].
- 4) As we will discuss in the next chapter, the FP concept can also be implemented in a macroscopic photographic imaging setting, where the aperture of a photographic lens naturally serves as a support constraint in the Fourier domain. By simply scanning the entire camera to different spatial positions, we can, thus, capture multiple images corresponding to different Fourier passbands. We can then synthesize them using the FP recovery process and bypass the resolution limit set by the aperture size of the photographic lens. The final achievable resolution is determined by the traveling range of the camera, not the size of the aperture [44]. Such an implementation may find important applications in remote sensing, where real-space ptychography cannot be applied.

The FP approach also shares its root with another related imaging modality: light-field microscopy. A light-field microscope employs a microlens array with M by M microlenses in front of the image sensor. To this end, the captured raw image of a light-field microscope contains M by M sub-images, corresponding to different microlens elements. By extracting different pixels from each sub-image, different perspective views of a 3D object can be synthesized, each corresponding to a different aperture of the objective's pupil plane [45, 46]. Similar to a light-field microscope, the FP setup also captures multiple perspective images of a sample, corresponding to different small apertures in the Fourier domain. There are two key differences between an FP and a light-field microscope. First, a light-field microscopy is applied to 3D object refocusing. FP, on the other hand, relies upon one-to-one mappings between the spatial and Fourier domain, and thus only applies to light emitted from a thin 2D sample. We note that it is possible to process an FP data set of a 3D object in a similar way as a light-field microscope image to achieve 3D sample refocusing and rendering [47]. A second key difference lies within the light-field microscope's sacrifice of spatial resolution to acquire additional 3D information, following what is referred as the spatio-angular resolution

tradeoff [45, 46]. The FP procedure also relies upon the interplay between spatial and angular resolvability, but achieves a different goal: increasing an object’s spatial resolution using different angular perspectives. Therefore, one can think of FP as a light-field-capturing setup focused on processing all captured data to improve spatial resolution.

2.3 Aberration correction in FP

In this section, we will discuss how to handle pupil aberrations in the recovery process of FP. We will first discuss the recovery scheme for known aberrations (section 2.3.1). We will then discuss two approaches for handling unknown aberrations in FP (section 2.3.2).

2.3.1 Correcting known aberrations in FP

If the aberration of the system is known, we can model it as a pupil function in the coherent imaging process. In line 4 below, we generate a coherent transfer function without aberrations. In lines 5–6, we define a pupil function for defocus aberration and the defocus distance is set to 10 μm . In line 7, we define the coherent transfer function with the 10- μm -defocus aberration.

```

1  cutoffFrequency = NA * k0;
2  kmax = pi/spsize;
3  [kxm kym] = meshgrid(-kmax:kmax/((n1-1)/2):kmax,-kmax:kmax/((n1-1)/2):kmax);
4  CTF = ((kxm.^2+kym.^2)<cutoffFrequency^2);
5  z = 10e-6; kzm = sqrt(k0^2-kxm.^2-kym.^2);
6  pupil = exp(1i.*z.*real(kzm)).*exp(-abs(z).*abs(imag(kzm)));
7  CTF_withaberration = pupil.*CTF;
```

In the forward imaging model of FP, we can then use the aberrated coherent transfer function to perform low-pass filtering and obtain the low-resolution output, as shown in line 14.

```

8  objectFT = fftshift(fft2(object));
9  for tt =1:arraysize^2
10    kxc = round((n+1)/2+kx(1,tt)/dkx);
11    kyc = round((m+1)/2+ky(1,tt)/dky);
12    kyl=round(kyc-(m1-1)/2);kyh=round(kyc+(m1-1)/2);
13    kxl=round(kxc-(n1-1)/2);kxh=round(kxc+(n1-1)/2);
14    imSeqLowFT = (m1/m)^2 * objectFT(kyl:kyh,kxl:kxh).*CTF_withaberration;
15    imSeqLowRes(:,:,tt) = abs(ifft2(ifftshift(imSeqLowFT)));
16  end;
17  figure;imshow(imSeqLowRes(:,:,225),[]);
```

Similarly, in the recovery process of FP, we can model and correct for aberrations in each iteration step. In line 29, we generate a low-resolution image using the aberrated coherent transfer function. In line 33, we invert the pupil function to compensate for the known aberration. By simply using these two lines, we are able to model and compensate for any known aberration of the imaging system.

```

18 seq = gseq(arraysize);
19 objectRecover = ones(m,n);
20 objectRecoverFT = fftshift(fft2(objectRecover));
21 loop = 5;
22 for tt=1:loop
23   for i3=1:arraysize^2
24     i2=seq(i3);
25     kxc = round((n+1)/2+kx(1,i2)/dkx);
26     kyc = round((m+1)/2+ky(1,i2)/dky);
27     Kyl = round(kyc-(m1-1)/2);kyh=round(kyc+(m1-1)/2);
28     kxl = round(kxc-(n1-1)/2);kxh=round(kxc+(n1-1)/2);
29     lowResFT = (m1/m)^2 * objectRecoverFT(kyl:kyh,kxl:kxh).*CTF.*pupil;
30     im_lowRes = ifft2(ifftshift(lowResFT));
31     im_lowRes = (m/m1)^2 * ImSeqLowRes(:, :, i2)
32
33   . *exp(i1.*angle(im_lowRes));
34   lowResFT = fftshift(fft2(im_lowRes)).*CTF.* (1./pupil);
35   objectRecoverFT(kyl:kyh,kxl:kxh) = (1-CTF).*
36   objectRecoverFT(kyl:kyh,kxl:kxh) + lowResFT;
37 end;
38 objectRecover = ifft2(ifftshift(objectRecoverFT));
39 imshow(abs(objectRecover), []);

```

In figure 2.8, we simulate the aberration-correction performance of the above procedures. Each row contains simulated images with the object placed at different defocus planes (ranging from $-150 \mu\text{m}$ to $150 \mu\text{m}$). Column 1 displays the low-resolution



Figure 2.8. Aberration correction in FP. Adapted from [2].

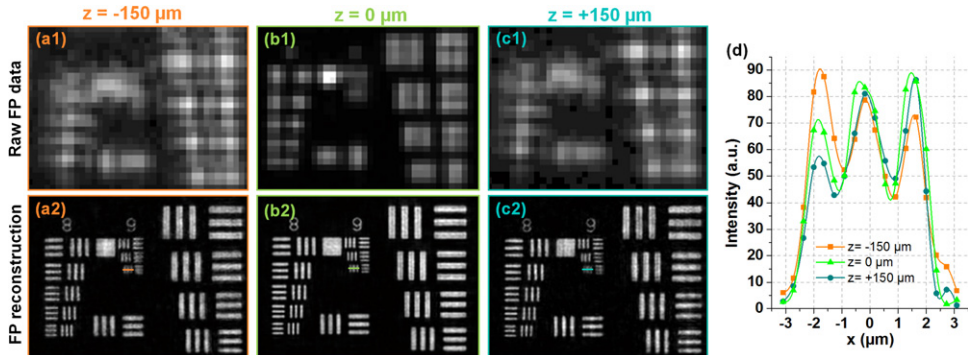


Figure 2.9. Correcting aberrations and extending depth of field using FP. (a1)–(c1) The low-resolution raw image of a resolution target, corresponding to defocused distances $-150 \mu\text{m}$, 0 , and $+150 \mu\text{m}$. (a2)–(c2) The high-resolution FP reconstructions by correcting the defocus aberrations. (d) Line traces of the small features in (a2)–(c2). Adapted from [2].

images using the forward imaging model. Columns 2 and 3 show the recovered high-resolution amplitude and phase profiles using aberration-correction procedures. As a comparison, columns 4 and 5 show the recovered high-resolution amplitude and phase profiles without modeling the pupil aberration in the recovery process, clearly exhibiting errors. One application of the aberration-correction capability in FP is to compensate for defocus aberrations and extend the depth of field of the imaging platform, as shown in figure 2.9 [2]. In this figure, we placed a resolution target at three different positions along the z -axis and performed FP imaging using a $2\times$, 0.08 NA objective lens. The synthetic NA of the recovered images is ~ 0.5 . From the recovered images, it is clear that the FP scheme is able to achieve a resolution-invariant depth-of-field of ~ 0.3 mm by modeling the aberrated pupil function in the recovery process. As a reference point, the depth-of-field of an objective with a similar 0.5 NA is $\sim 4 \mu\text{m}$.

2.3.2 Correcting unknown aberrations in FP

The aberration correction process discussed in the last section is based on the known aberrated pupil function. One question is that, if the pupil aberration is unknown, can we still compensate for the aberrations? We have two approaches for correcting unknown pupil aberrations in FP. The first approach is to use the concepts in adaptive optics for aberration correction [39] and the second approach is to recover both the high-resolution complex object and the unknown aberrated pupil function in the iterative process [38]. We will discuss these two approaches as follows.

In the first approach, we employ the concepts in adaptive optics for aberration correction [39]. There are two key components in conventional adaptive optics systems: a wavefront sensor for measuring the distortion and an adaptive optical element (for example, a deformable mirror) for performing system correction. If the wavefront sensor is not available, an image-quality metric can be used as the guide star for providing feedback for aberration correction. To employ the concepts of adaptive optics in FP, we need to first define an image-quality metric as a guide star for the optimization process, and then perform system corrections to maximize such

a guide star. A typical image-quality metric for conventional adaptive optics systems is the sharpness-metric, which can be calculated through the gradient of the image. In the FP scheme, however, the sharp features in the recovered image can be a result of incorrect modeling or artifacts of the reconstruction process. Therefore, we need to use convergence-related property [10–16] to quantify the quality of the FP reconstruction. We define the image-quality metric of FP as follows

$$\text{Convergence index} = \sum_{\text{all incident angles}} \frac{\text{mean}(\sqrt{I_l})}{\sum_{x,y} \text{abs}(\sqrt{I_{lm}} - \sqrt{I_l})} \quad (2.3)$$

where I_l is the low-resolution target image produced from the sample estimate and I_{lm} is the low-resolution intensity measurement. The ‘ x - y ’ summation in equation (2.3) is for adding up all the pixel values in the spatial domain, and the ‘incident angle’ summation is for adding up contributions of all captured images. If the difference between $\sqrt{I_{lm}}$ and $\sqrt{I_l}$ is small for all incident angles, the FP reconstruction is considered consistent with the intensity measurements, and the resulting value of the convergence index is high. In other words, the convergence index can be used to quantify the quality of the FP reconstruction: the higher the convergence index, the better the quality of the FP reconstruction. In MATLAB implementation, we can define the convergence index in lines 15–16 as follows:

```

1  seq = gseq(arraySize);
2  objectRecover = ones(m,n);
3  objectRecoverFT = fftshift(fft2(objectRecover));
4  loop = 5;
5  convergeIndex = zeros(loop);
6  for tt=1:loop
7      for i3=1:arraySize^2
8          i2=seq(i3);
9          kxc = round((n+1)/2+kx(1,i2)/dkx);
10         kyc = round((m+1)/2+ky(1,i2)/dky);
11         Kyl = round(kyc-(m1-1)/2); kyh=round(kyc+(m1-1)/2);
12         kxl = round(kxc-(n1-1)/2); kxh=round(kxc+(n1-1)/2);
13         lowResFT = (m1/m)^2 * objectRecoverFT(kyl:kyh,kxl:kxh).*CTF.*pupil;
14         im_lowRes = ifft2(ifftshift(lowResFT));
15         convergeIndex(loop)=convergeIndex(loop)+ mean(mean(abs(im_lowRes)))./
16             sum(sum(abs(im_lowRes - ImSeqLowRes(:,:,i2))));
17         im_lowRes = (m/m1)^2 * ImSeqLowRes(:,:,i2)
18             .*exp(li.*angle(im_lowRes));
19
20         lowResFT = fftshift(fft2(im_lowRes)).*CTF.*(.1./pupil);
21         objectRecoverFT(kyl:kyh,kxl:kxh) = (1-CTF).*
22             objectRecoverFT(kyl:kyh,kxl:kxh) + lowResFT;
23     end;
24 end;
objectRecover = ifft2(ifftshift(objectRecoverFT));

```

Once we have the convergence index (i.e., the guide star) defined in the recovery process of FP, we can perform system correction to maximize it. As an example, we used this scheme to recover the unknown defocus aberration of a resolution target in figure 2.10. In this experiment, the resolution target was placed at a defocused position which was treated as an unknown parameter. In the recovery process of FP, we calculated the convergence index as a function of the defocus distance. For the red curve in figure 2.10(c), we placed the sample at $z = -150 \mu\text{m}$ and the maximum value of the convergence index corresponds to a defocused distance of $-150.1 \mu\text{m}$, which is in a

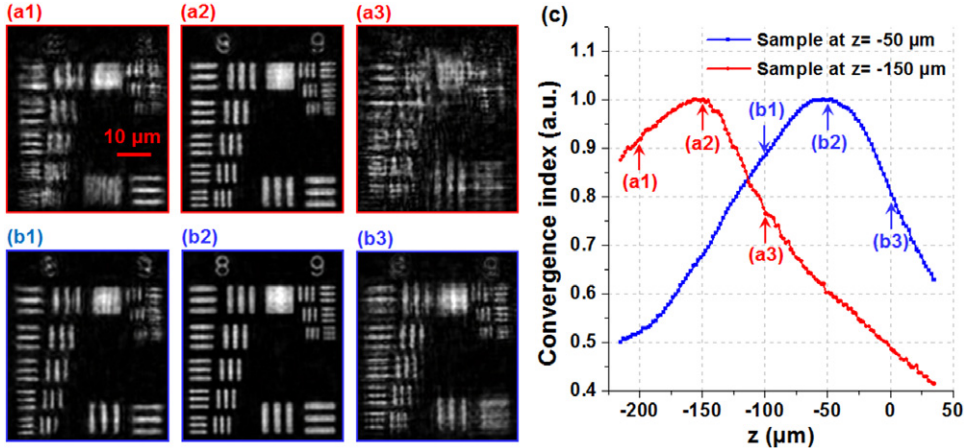


Figure 2.10. Defocus aberration recovery through optimization of the convergence index. (a)–(b) FP reconstructions using different defocused distances indicated in (c). (c) The convergence index as a function of different defocused distances. Adapted from [39].

good agreement with the actual sample position. Figures 2.10(a1)–(a3) show the FP reconstructions using three different defocus distances: $-200\text{ }\mu\text{m}$, $-150\text{ }\mu\text{m}$, and $-100\text{ }\mu\text{m}$. When the defocused distance matches with the actual sample position, we get the best FP reconstruction in figure 2.10(a2). We also repeated this experiment by placing the sample at $z = -50\text{ }\mu\text{m}$ (the blue curve in figure 2.10(c)). The corresponding reconstructions are shown in figure 2.10(b). Again, the recovered defocused distance from the convergence index is in a good agreement with the actual sample position.

The capability of automatically recovering the sample position is useful for imaging samples that are not on a flat surface. In this case, we can first divide the entire field of view into many small segments. We can then determine the defocused position for each small segment by maximizing the convergence index. Finally, we can perform the corresponding FP reconstructions and combine them into one image.

Following the same line of logic, figure 2.11 demonstrates the use of the adaptive correction scheme to recover the unknown second-order pupil function and perform aberration correction. Figure 2.11(a) shows the raw data of a blood smear. Figure 2.11(b) shows the FP recovered intensity and phase images using the adaptive correction scheme, while figure 2.11(c) shows the control images without using the adaptive correction scheme. Figure 2.11(d) shows the recovered unknown pupil aberration. We can see that the image quality of figure 2.11(b) is much better than that of figure 2.11(c), validating the effectiveness of the adaptive correction scheme. We note that, the adaptive correction scheme can also be used to correct for intensity fluctuation of the LED matrix and recover other unknown system parameters [39].

The second approach for handling unknown aberrations is to jointly recover the high-resolution sample image and the pupil function in the iterative process. This approach, termed embedded pupil function recovery (EPRY) [38], is inspired by a similar strategy demonstrated in the real-space ptychography [8, 48]. The implementation of EPRY in MATLAB is shown below. In lines 12 and 17, we define the

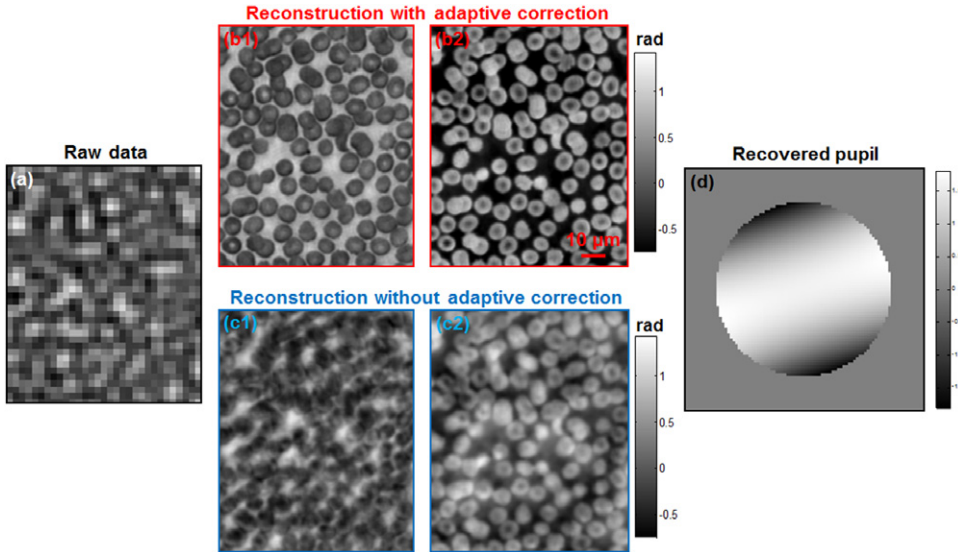


Figure 2.11. Second-order-aberration recovery through optimization of the convergence index. (a) The raw image of FP. (b) The FP reconstruction using the adaptive correction scheme. (c) The FP reconstruction without using the adaptive correction scheme. (d) The recovered pupil function. Adapted from [39].

Fourier spectra of the low-resolution image before and after the magnitude updating process. In lines 18–20, we update the high-resolution sample estimate using the difference of the two spectra defined in lines 12 and 17. In lines 21–23, we update the unknown pupil function of the imaging system.

```

1  seq = gseq(arraysize);
2  objectRecover = ones(m,n);
3  objectRecoverFT = fftshift(fft2(objectRecover));
4  loop = 25;pupil=1;
5  for tt=1:loop
6    for i3=1:arraysize^2
7      i2=seq(i3);
8      kxc = round((n+1)/2+kx(1,i2)/dkx);
9      kyc = round((m+1)/2+ky(1,i2)/dky);
10     kyl=round(kyc-(m1-1)/2);kyh=round(kyc+(m1-1)/2);
11     kxl=round(kxc-(n1-1)/2);kxh=round(kxc+(n1-1)/2);
12     lowResFT_1 = (m1/m)^2 *
13       objectRecoverFT(kyl:kyh,kxl:kxh).*CTF.*pupil;
14     im_lowRes = ifft2(ifftshift(lowResFT_1));
15     im_lowRes = (m/m1)^2 *
16       imSeqLowRes(:,:,i2).*exp(lj.*angle(im_lowRes));
17     lowResFT_2 = fftshift(fft2(im_lowRes)).*CTF.* (1./pupil);
18     objectRecoverFT(kyl:kyh,kxl:kxh) = objectRecoverFT(kyl:kyh,kxl:kxh)
19       + conj(pupil)./(max(max(abs(pupil).^2)));
20       .* (lowResFT_2 - lowResFT_1);
21     pupil = pupil + conj(objectRecoverFT(kyl:kyh,kxl:kxh))
22       ./ (max(max(abs(objectRecoverFT(kyl:kyh,kxl:kxh)).^2)))
23       .* (lowResFT_2 - lowResFT_1);
24   end;
25 end;
26 objectRecover=ifft2(ifftshift(objectRecoverFT));
27 imshow(abs(objectRecover),[]);
28 figure;imshow(angle(objectRecover),[]);
29 figure;imshow(log(objectRecoverFT),[]);

```

Figure 2.12 demonstrates the application of the EPRY scheme for aberration correction [38]. In this experiment, we used a pathology slide as the sample and a 2 \times , 0.08 NA objective lens for image acquisition. The entire slide was divided into small tiles and the EPRY scheme was applied to each tile to recover both the high-resolution intensity image and the unknown pupil aberration. Figures 2.12(a)–(c) represent results at different spatial positions of the slide. The wavefront aberrations for red, green, and blue channels are shown in figure 2.12(a2)–(c2), (a3)–(c3), and (a4)–(c4). We note that, aperture sizes are different for different color channels, as they are scaled by different wavelengths. We also note that, the shape of the pupil function changes from a circle to an ellipse as we move from the center to the edge of the slide. This is because the 2 \times objective lens is not a strict telecentric lens and the aperture shape changes asymmetrically as we move towards the edge of the field of view.

In summary, the FP scheme is able to correct for any known or unknown pupil aberration. If the aberration is known, we can simply invert the pupil function in the iterative process. If the aberration is unknown, we can either use the adaptive correction scheme or the EPRY scheme to recover it.

2.4 Sampling requirements of FP

In this section, we will first discuss the sampling requirement of FP in the spatial domain. We will then discuss the sampling strategy in the Fourier domain. In particular, we will demonstrate the use of non-uniform sampling pattern in the Fourier domain to reduce the number of raw image acquisitions.

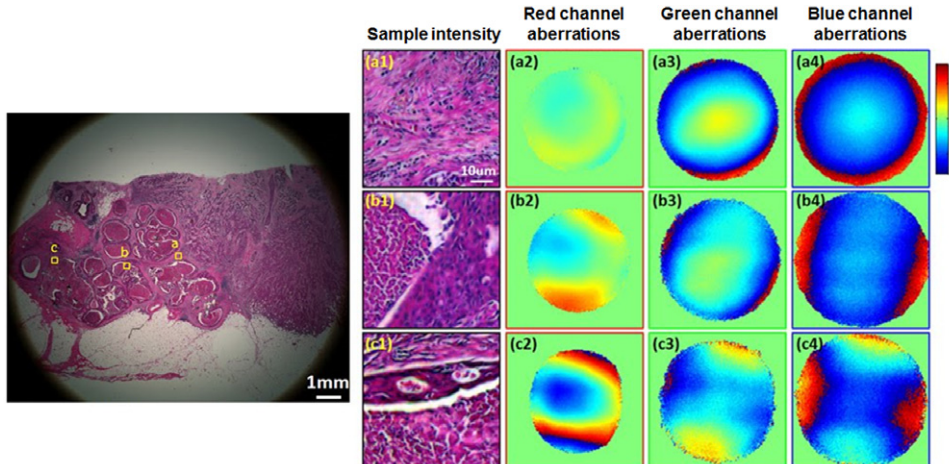


Figure 2.12. High-resolution FP reconstruction of a pathology slide and the recovered pupil aberrations using the EPRY scheme. (a1)–(c1) The reconstructed intensity images at different spatial positions of the slide. (a2)–(c2) The recovered red channel aberrations. (a3)–(c3) The recovered green channel aberrations. (a4)–(c4) The recovered blue channel aberrations. Adapted from [38].

2.4.1 Sampling in the spatial domain

In the spatial domain, there are two questions regarding the sampling requirement of FP [2]:

- 1) given the NA of an objective lens, what is the largest pixel size we can use for acquiring the low-resolution intensity images;
- 2) given the synthetic NA of the reconstructed image, what is the largest pixel size we can use for the reconstructed intensity image.

To answer the first question, we need to keep in mind that, FP is a coherent imaging method and it has the same sampling requirement as that in conventional coherent imaging systems. In chapter 1, we have shown that the resolution of coherent imaging system is λ/NA_{obj} for the complex light field. Therefore, we need to use a pixel size of $\lambda/(2 \cdot NA_{\text{obj}})$ or smaller to sample the complex signal in the spatial domain. Here, the factor of 2 comes from the Nyquist sampling theorem.

For the second question, we note that, the synthetic NA of the final recovered image is for the complex light field E (with amplitude and phase). We need to convert this complex light field to intensity profile I for analysis, and $I = E \cdot E^*$ ($*$ denotes complex conjugate). The multiplication operation between the complex light field and its conjugate corresponds to a convolution operation in the Fourier domain. As such, the passband of the reconstructed intensity image doubles in the Fourier domain, i.e., $k_{\max} = 2 \cdot NA_{\text{syn}} \cdot k_0$ for the intensity signal. Therefore, the largest pixel size we can use for representing the reconstructed intensity image is $\lambda/(4 \cdot NA_{\text{syn}})$. We note that, this sampling requirement is the same as that in conventional incoherent imaging systems. If we choose the largest pixel sizes both for the raw image and the reconstructed image, the pixel enhancement factor of FP can be expressed as:

$$\text{Enhancement factor} = 2 \cdot NA_{\text{syn}}/NA_{\text{obj}} \quad (2.4)$$

Now we have another question: if the sampling pixel size is too large for acquiring the raw FP image, what should we do? This question, in fact, is an important one since the pixel size of the employed image sensor may not satisfy the sampling requirement. As an example, we consider a 2 \times objective lens with 0.1 NA. The sampling pixel size for the raw FP image is $\lambda/(2 \cdot NA_{\text{obj}})$ at the object plane. If we use green light with $\lambda = 0.5 \mu\text{m}$, we need to have a sampling pixel size of $2.5 \mu\text{m}$ or smaller at the object plane. Considering the 2 \times magnification factor of the objective lens, we need to have a sampling pixel size of $5 \mu\text{m}$ or smaller at the detector plane; in other words, the pixel size of the image sensor needs to be smaller than $5 \mu\text{m}$. The pixel size of typical image sensors ranges from $1.5 \mu\text{m}$ to $10 \mu\text{m}$, and thus, not all of them satisfy the sampling requirement of FP. A pixel size larger than $\lambda/(2 \cdot NA_{\text{obj}})$ may lead to the pixel aliasing problem in the Fourier domain (figure 2.13(a)). It would also significantly degrade the quality of the FP reconstruction. To address the problem, we can use a sub-sampled scheme in FP [49]. A similar scheme has also been discussed in real-space ptychography [50].

The sub-sampled FP scheme is shown in figure 2.13(b), where we divide one original pixel into 4 sub-pixels and the effective pixel size is only half of the original

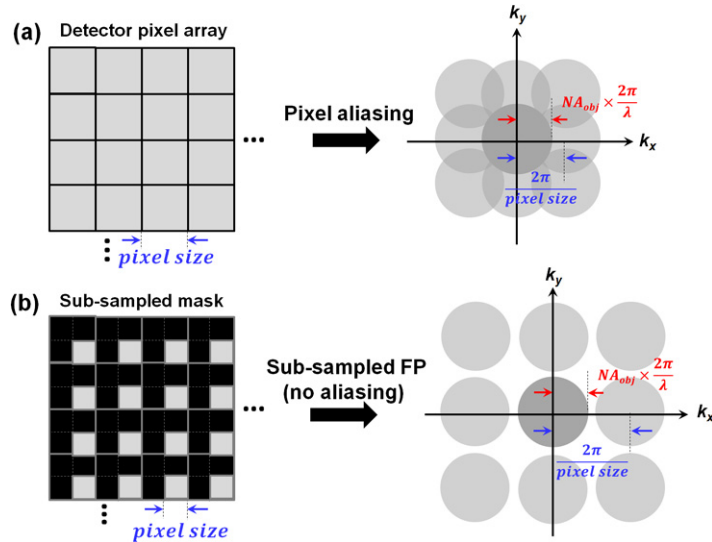


Figure 2.13. The sub-sampled FP scheme. (a) The pixel aliasing problem due to the use of a large pixel size in the spatial domain. (b) The sub-sampled scheme by dividing one original pixel into 4 sub-pixels. The effective pixel size is only half of the original pixel size. At each iteration, only 1 out of 4 sub-pixels is updated by the measurement. The other 3 are kept unchanged. Adapted from [49].

pixel size. We then generate a sub-sampled mask in the amplitude updating step, as shown in the left part of figure 2.13(b). Only 1 out of 4 sub-pixels is updated by the measurement and the other 3 sub-pixels are kept unchanged in the updating process.

In the following MATLAB code, we implement this sub-sampled scheme in line 15, where we update the 1 out 4 pixels of ‘im_lowRes’ using the measurement ‘ImSeqLowRes(:, :, i2)’:

```

1  seq = gseq(arraySize);
2  objectRecover = ones(m,n);
3  objectRecoverFT = fftshift(fft2(objectRecover));
4  loop = 5;
5  converIndex = zeros(loop);
6  for tt=1:loop
7      for i3=1:arraySize^2
8          i2=seq(i3);
9          kxc = round((n+1)/2+kx(1,i2)/dkx);
10         kyc = round((m+1)/2+ky(1,i2)/dky);
11         Kyl = round(kyc-(m1-1)/2); kyh=round(kyc+(m1-1)/2);
12         kxl = round(kxc-(n1-1)/2); kxh=round(kxc+(n1-1)/2);
13         lowResFT = (m1/m)^2 * objectRecoverFT(kyl:kyh,kxl:kxh).*CTF.*pupil;
14         im_lowRes = ifft2(ifftshift(lowResFT));
15         im_lowRes (1:2:end,1:2:end) = (m/m1)^2 * ImSeqLowRes(:, :, i2)
16             .*exp(1i.*angle(im_lowRes));
17
18         lowResFT = fftshift(fft2(im_lowRes)).*CTF.* (1./pupil);
19         objectRecoverFT(kyl:kyh,kxl:kxh) = (1-CTF).*
20             objectRecoverFT(kyl:kyh,kxl:kxh) + lowResFT;
21     end;
22 end;
objectRecover = ifft2(ifftshift(objectRecoverFT));

```

Figure 2.14 shows the simulation result of the sub-sampled FP scheme, where we used a pixel size of $4.125 \mu\text{m}$, a wavelength of $0.63 \mu\text{m}$, and an NA of 0.1. Therefore, the pixel size is larger than the sampling requirement of $3.15 \mu\text{m}$. We simulated the use of a 15 by 15 LED matrix for sample illumination and the maximum synthetic NA is about 0.4. Figure 2.14(a) shows one raw intensity image of the sample. Figures 2.14(b1)–(b2) demonstrate the FP reconstructions using the sub-sampled scheme. Figure 2.14(b3) shows the corresponding recovered spectrum in the Fourier space. The case without using the sub-sampled scheme is shown in figure 2.14(c). Due to the pixel aliasing problem, there is not enough bandwidth to impose the circular pupil function in the Fourier space. As such, each low-resolution image corresponds to a square region in the Fourier space of figure 2.14(c3), and the final reconstructed images are corrupted by the pixel aliasing problem.

The sub-sampled scheme can also be modified to handle other challenges in FP. One challenge is the limited dynamic range of the detector in FP experiments. Due to the limited bit-depth of the image sensors, we need to acquire multiple images with different exposure times for the same LED element (typically, one short and one long). These raw images are then combined to produce a high-dynamic-range (HDR) image for one LED element. Figure 2.15 demonstrates such an HDR combination process. Figure 2.15(a) shows a raw image of a blood smear sample, where many regions are overexposed. Figure 2.15(b) shows the HDR image by combining two raw images with two different exposure times. The sampling strategy to handle the underexposed/overexposed pixels is similar to the sub-sampled FP scheme. Here, we term it sparsely-sampled FP scheme. In the amplitude updating step, we will generate a sparsely sampled mask by binarizing the

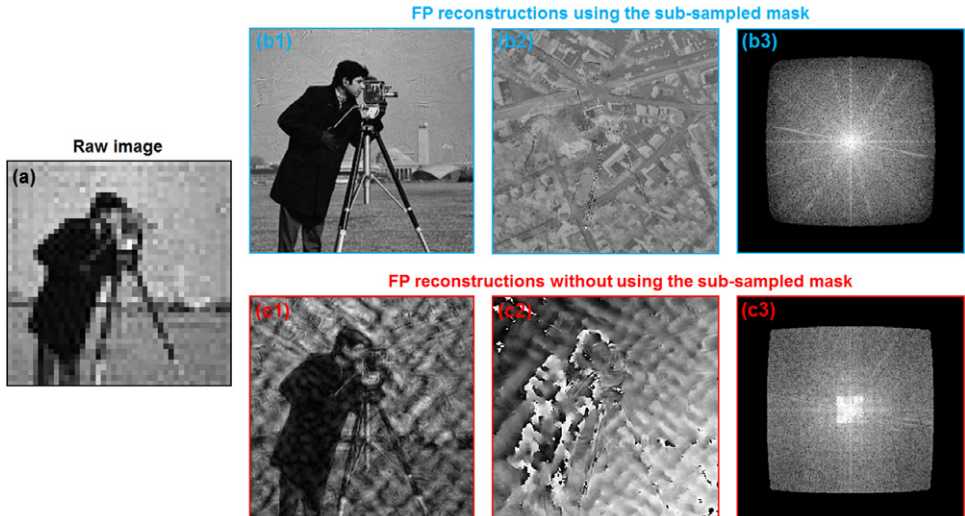


Figure 2.14. Simulation of the sub-sampled FP scheme. (a) The raw intensity image with a pixel size larger than the sampling requirement. (b1)–(b2) The FP reconstructions using the sub-sampled scheme. (b3) The recovered spectrum of (b1) and (b2). (c1)–(c2) The FP reconstructions without using the sub-sampled scheme. (c3) The recovered spectrum of (c1) and (c2). Adapted from [49].

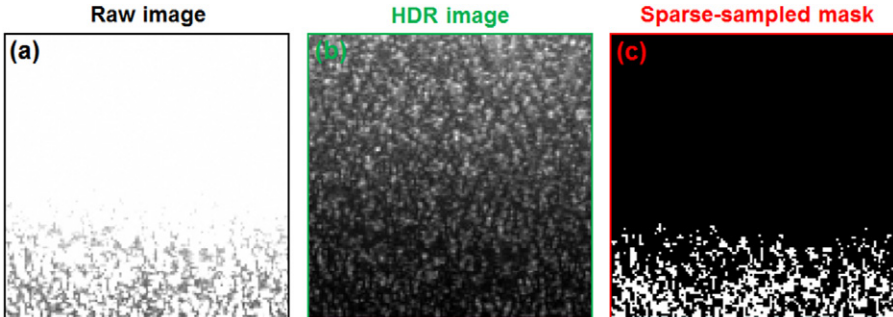


Figure 2.15. Sparsely-sampled mask in FP. (a) The overexposed raw image of a blood smear sample. (b) The corresponding HDR image of (a). Two exposure times were used in the HDR combination process. (c) The sparsely sampled mask by binarizing the overexposed raw image of (a). Adapted from [49].

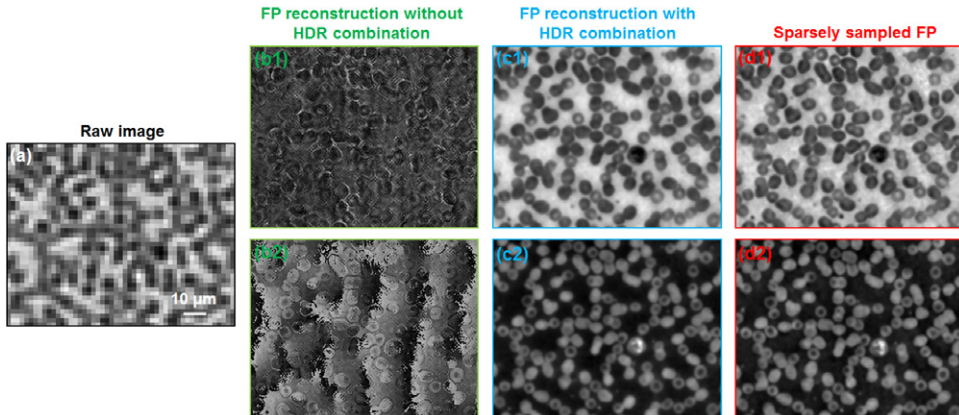


Figure 2.16. Solving the limited bit-depth problem using the sparsely-sampled scheme. (a) The raw image of a blood smear sample. The FP recovered intensity and phase images without (b) and with (c) the HDR combination process. (d) The FP reconstruction using the sparsely-sampled FP scheme. (b1)–(d1) The recovered high-resolution intensity images. (b2)–(d2) The recovered high-resolution phase images. Adapted from [49].

underexposed/overexposed pixels, as shown in figure 2.15(c). We can choose two threshold values for this binarizing process. As an example, we consider an 8-bit raw image with the captured intensity value ranging from 0 to 255. We can set two values in this case: 3 and 245. If the pixel value is less than 3 (underexposed) or higher than 245 (overexposed), we will set this pixel to 0 in the binary mask. We then apply the binary mask in the amplitude updating process: the regions with underexposed/overexposed pixels will be kept unchanged while other regions will be updated by the intensity measurements. As a reference point, the percentage of underexposed/overexposed pixels is typically no more than 15% in an FP experiment. Depending on the percentage of the invalid pixels, one may need to increase the number of plane wave illuminations to ensure the solution convergence.

We validated the sparsely-sampled FP scheme using an experiment in figure 2.16, where we used a blood smear slide as the sample and a 2 \times , 0.08 NA objective for

image acquisition. Figure 2.16(a) shows the raw image of the sample with a pixel size of 2.75 μm . Figures 2.16(b1) and (b2) demonstrate the recovered intensity and phase images without using the HDR combination process. These two images are corrupted by the overexposed pixels in the raw images. Figure 2.16(c) demonstrates the recovered images using the HDR combination process. The result of the sparsely-sampled FP scheme is shown in figure 2.16(d). From the comparison in figure 2.16, we can see that, the image quality of the sparsely-sampled scheme is comparable to that with the HDR combination process. The advantage of this scheme is obvious: it gets rid of the multi-exposure acquisition process and significantly shortens the acquisition time.

2.4.2 Sampling in the Fourier domain

A key aspect of a successful FP reconstruction is the data redundancy requirement in the recovery process. In particular, images with different plane wave illuminations correspond to different spectrum regions in the Fourier space. Intuitively, a certain amount of spectrum overlap in between successive acquisitions is needed to connect all acquired images in the Fourier space. If there is no overlap in between these spectrum regions, FP reduces to a conventional phase retrieval procedure where each image can be processed independently. In this section, we want to answer the following questions: how much spectrum overlap is needed for a successful FP reconstruction and how do we arrange the LED positions to optimize the spectrum overlap?

The spectrum overlap is determined by the angular variation between two successive illuminations. We define the overlapping percentage as the overlapping region of two successive acquisitions divided by the entire region of the objective's pupil aperture. A typical FP platform uses an LED matrix for providing angle-varied illuminations. As such, the spectrum overlapping percentage is determined by the distance between adjacent LED elements and the distance between the LED matrix and the sample. In figure 2.17, we investigate the spectrum overlapping percentage versus the reconstruction quality. The simulation parameters were chosen to realistically model a light microscope experiment, with an incident wavelength of 632 nm, a pixel size of 2.75 μm and an objective NA of 0.08. We simulated the use of a 15 by 15 LED matrix for sample illumination. A different spectrum overlapping percentage was achieved by adjusting the distance between the LED array and the sample. The high-resolution input intensity and phase profiles are shown in figures 2.17(a1) and (a2), which serve as the ground truth of the simulated object. Figures 2.17(b)–(d) demonstrate the FP reconstructions with different spectrum overlapping percentages. It is obvious that the reconstruction quality of figure 2.17(b) (with an 18% overlapping percentage) is worse than those with higher overlapping percentages. The image qualities of different FP reconstructions are quantified in figure 2.17(e), where the root-mean-square (RMS) error (i.e. the difference between the ground truth and the recovered images) is plotted as a function of the overlapping percentage. It is shown that the RMS error decreases as the overlapping percentage increases, and a minimum of $\sim 35\%$ overlapping percentage is needed for a successful FP reconstruction.

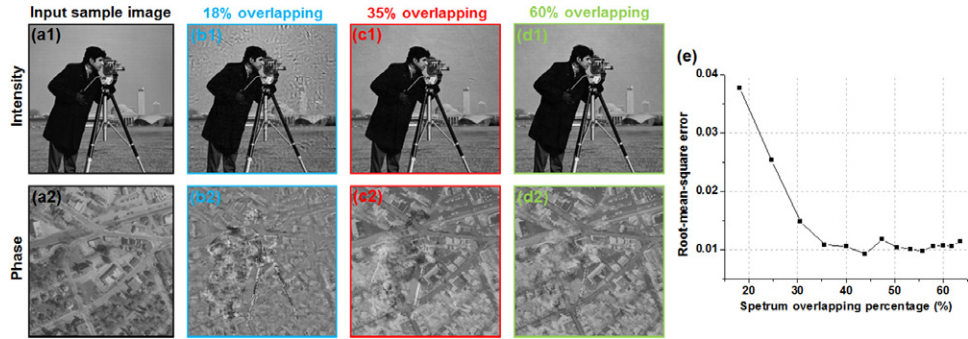


Figure 2.17. FP reconstructions with different spectrum overlapping percentages, assuming an LED matrix is used for sample illumination. (a1)–(a2) The input high-resolution intensity and phase profiles of the simulated complex sample. (b)–(d) FP reconstructions with different spectrum overlapping percentages in the Fourier domain. (e) The RMS error of FP reconstructions with different spectrum overlapping percentages. Adapted from [49].

In the previous paragraph, we assume using an LED matrix for sample illumination. The incident wave vector of each LED element (k_{xn}, k_{yn}) corresponds one sampling point in the Fourier space. The use of LED matrix for sample illumination, therefore, corresponds to the use of a grid sampling pattern in the Fourier domain. The sampling points of this grid pattern uniformly distribute across the Fourier space. It follows an important question: can we use non-uniform sampling patterns to reduce the overlapping percentage in FP [41]. Figure 2.18 demonstrates the use of different sampling patterns in the Fourier space and their FP reconstructions. Going from figure 2.18(a1) to (a5), the sampling patterns have a higher overlapping percentage at the center while the total number of LED elements remains the same. In particular, figure 2.18(a2) shows a sampling pattern where the sampling points are uniformly distributed in the Fourier space. The corresponding FP reconstructions are shown in figure 2.18(b1)–(b5). In figure 2.18(c), we plot the overlapping percentage as a function of illumination NA for the cases shown in figure 2.18(a1)–(a5). We can define the sampling density ratio α as the overlapping percentage at the edge divided by that at the center. Using this definition, the sampling density ratio in figure 2.18(a1)–(a5) increases from 0.7 to 2.0. The RMS errors corresponding to these different sampling density ratios are shown in figure 2.18(d), where a higher sampling density at the central Fourier space leads to a better FP reconstruction. The reason for this behavior is easy to understand: as the Fourier spectral energy concentrates at low-frequency regions, a higher sampling density at low-frequency regions helps the solution to converge faster to the global optimal.

One important implication of figure 2.18 is that we can reduce the number of image acquisitions using a non-uniform sampling pattern in the Fourier domain. As shown in figure 2.19, we have performed an experiment to demonstrate this idea [41]. In this figure, we show two sets of FP reconstructions: one using a uniform sampling pattern (an LED matrix) and the other one using a non-uniform sampling pattern (a ring-LED illuminator). For both cases, we used 68 LED elements for sample illumination and a 4x, 0.1 NA objective lens for image acquisition. The final

Fourier Ptychographic Imaging

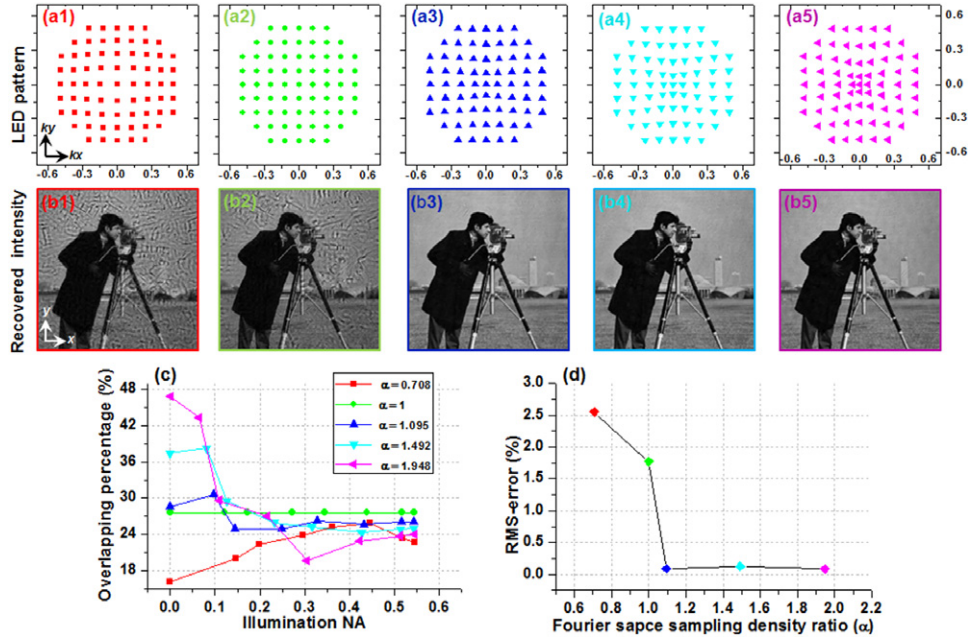


Figure 2.18. FP reconstructions with different sampling patterns in the Fourier space. (a1)–(a5) The LED sampling patterns in the Fourier space. (b1)–(b5) The FP reconstructions corresponding to (a1)–(a5). (c) The overlapping percentage as a function of the illumination NA. Different curves correspond to different cases in (a1)–(a5) (see the color code). (d) The RMS error as a function of the sampling density ratio. A higher sampling density at the center leads to a better FP reconstruction. Adapted from [41].

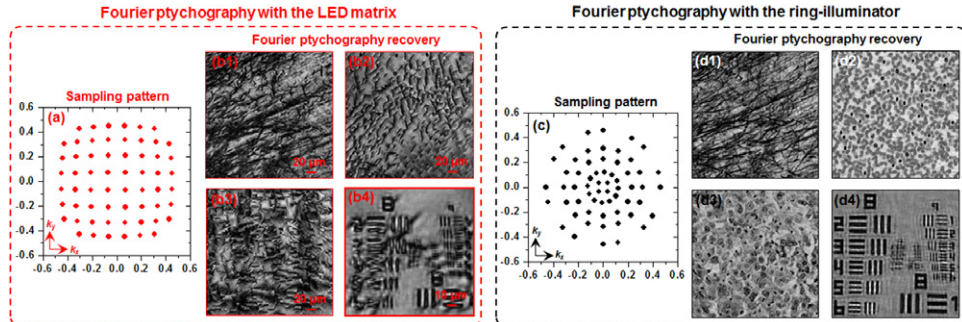


Figure 2.19. Comparison of FP reconstructions using the uniform and non-uniform sampling patterns in the Fourier domain. The total numbers of LED elements are the same for both cases (68 LEDs). (a) The sampling pattern of the periodic LED array in the Fourier domain. (b) The FP reconstructions using the periodic LED array, including a mouse brain slice (b1), a blood smear (b2), a pathology slide (b3), and a USAF resolution target (b4). (c) The sampling pattern of the ring-LED illuminator in the Fourier space. (d) The FP reconstructions using the ring-LED illuminator (non-uniform sampling in the Fourier domain). Adapted from [41].

synthetic NAs for both cases are ~ 0.55 . We can see that, the image quality in figure 2.19(d) (using the non-uniform sampling pattern) is much better than that in figure 2.19(b) (using the uniform LED matrix). We also note that, the use of non-uniform sampling pattern is able to reduce the number image acquisitions by at least 50% (68 images [41] versus 137 images in the FP prototype [1]).

Another important consideration of Fourier-domain sampling is the translational symmetry of the sampling pattern. In section 2.3.2, we have discussed how to update the sample and the unknown pupil aberration in the iterative process [19, 20]. If the sampling pattern is a periodic grid in the Fourier space, it would introduce periodic artifacts to the recovered pupil function [8]. This problem is called raster-grid pathology [8] and the corrupted pupil function would further degrade the high-resolution FP reconstruction. We study this raster-grid pathology problem in figure 2.20, where we compare the case of non-uniform sampling pattern with the case of periodic pattern. The RMS error is plotted as a function of the loop iteration in figure 2.20(c). Figures 2.20(d)–(g) show the recovered sample images and the pupil

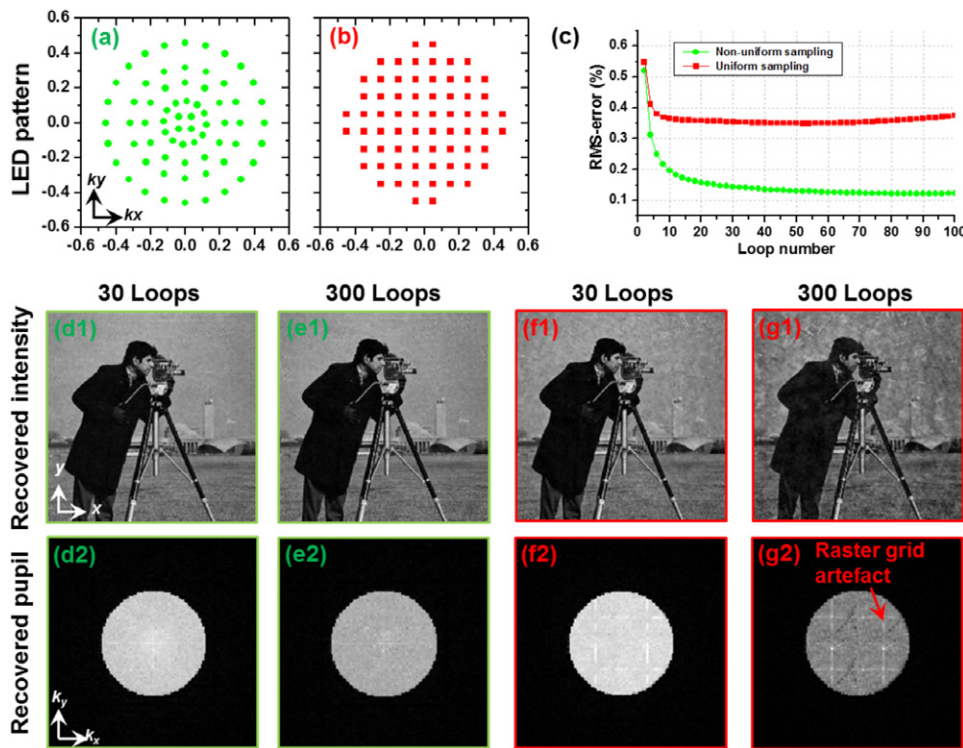


Figure 2.20. Solving the raster-grid pathology problem with a non-uniform sampling pattern in the Fourier domain. (a) A non-uniform sampling pattern and (b) a uniform sampling pattern in the Fourier domain. (c) The RMS error is plotted as a function of the iteration number. (d)–(e) The recovered sample images and pupil functions corresponding to (a). (f)–(g) The recovered sample images and pupil functions corresponding to (b). The raster-grid pathology problem is presented in (g). The use of non-uniform sampling pattern is able to solve the raster-grid pathology problem of FP. Adapted from [41].

functions. For the case of periodic sampling pattern in figure 2.20(g), the FP reconstruction degrades with more iterations and the recovered pupil function contains periodic artifacts. For the case of non-uniform sampling pattern in figure 2.20(e), the FP reconstruction converges with more iterations and the recovered pupil function does not contain periodic artifacts. It follows that the use of non-uniform sampling pattern in the Fourier domain is able to solve the raster-grid pathology problem of FP.

To summarize, we have discussed the Fourier-domain sampling strategy of FP. There are several take-away points:

- 1) a certain amount of Fourier spectrum overlap between adjacent acquisitions is needed in FP.
- 2) A non-uniform sampling pattern with higher sampling density at the center is preferred for improving the solution convergence and reducing the number of image acquisitions.
- 3) A non-uniform sampling pattern is able to break the translational symmetry and solve the raster-grid pathology problem.

Finally, one can design non-uniform sampling patterns for FP using one simple engineering guideline: reducing the spectrum overlapping percentage from 40% at the center (bright-field images) to 15% at the edge (dark-field images).

2.5 Optimal updating sequence for FP: energy criteria

In this section, we will answer the following question: if we capture N raw images corresponding to different incident angles, what is the optimal sequence to apply these raw images in the FP reconstruction process? For example, we capture three raw images I_1 , I_2 , and I_3 corresponding to three different incident angles. In the FP reconstruction process, we can update the sample estimate first with I_1 , then with I_2 , and lastly with I_3 . We can also choose another updating order such as I_2 , I_1 , and I_3 . The choice of the updating sequence is important for fast solution convergence. If the updating sequence is not properly chosen, the iterative alternative projection algorithm [27] may stagnate at a local minimum. In the experimental implementation of FP, the order of raw-image acquisition can be different from the order of the updating sequence, as we can always reorder the images after they have been acquired. However, if we want to process the data during the acquisition process, we need to light up the LED elements in the same order as that of the updating sequence (reordering is not possible in this case).

Here, we will discuss three updating sequences and compare their imaging performances. The three updating sequences are

- 1) a random sequence,
- 2) a sequence ranked by the LED illumination NA, and
- 3) a sequence ranked by the total energy of the raw images.

For case 1, we will randomly reorder the captured images and use them to update the sample estimate. For case 2, we will reorder the captured images according to

their incident angles (smallest angle ranks first) and update the sample estimate accordingly. For case 3, we will reorder the captured images according to their total intensity values and update the sample estimate accordingly.

Figure 2.21 shows the reconstructed images obtained from the three cases discussed above. We quantify the RMS errors (the differences between the FP reconstructions and the ground truth) for the three cases in figure 2.21(e). We can see that the image quality of the random-order case is worse than that of the other two and the corresponding RMS error is much higher in figure 2.21(e). This simulation study shows that, a carefully-chosen updating sequence is important for fast solution convergence. In the case of a random updating sequence, the solution may stagnate at a local minimum instead of the global minimum. We also note that the illumination-NA order and the total-energy order give similar performances in figure 2.21. The reason can be explained as follows: the energy of the sample spectrum is concentrated at low-frequency regions, i.e. the energy level decreases as the illumination NA increases. As a result, the illumination-NA order and the total-energy order give a similar updating sequence.

To further study the difference between the illumination-NA order and the total-energy order, we need to consider a sample image with its Fourier-spectrum energy not concentrated at low-frequency regions. In figure 2.22, we consider the ‘cameraman’ sample image modulated by a sinusoidal pattern. In this case, the spectral energy is concentrated at two off-center positions in the Fourier domain. In figure 2.22(a)–(c), we perform FP reconstruction using the three updating sequences: the random order (figure 2.22(a)), the illumination-NA order (figure 2.22(b)), and the total-energy order (figure 2.22(c)). The corresponding RMS error curves are shown in figure 2.22(d), where the total-energy order gives the best performance for solution convergence. This study implies that, the captured raw images with high energy levels are able to quickly guide the solution to the global minimum in the solution space. To this end, it may be important to consider the energy distribution of the sample spectrum and choose an optimal updating sequence in FP experiments.

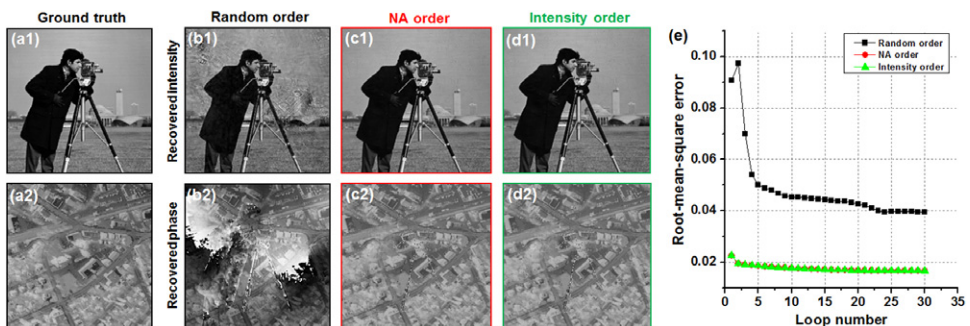


Figure 2.21. FP reconstructions using different updating sequences. (a) The input intensity and phase images. The FP reconstructions using the random order (b), the illumination-NA order (c), and the total-energy order (d). (e) The RMS error of the FP reconstructions versus the iteration loop number. Adapted from [41].

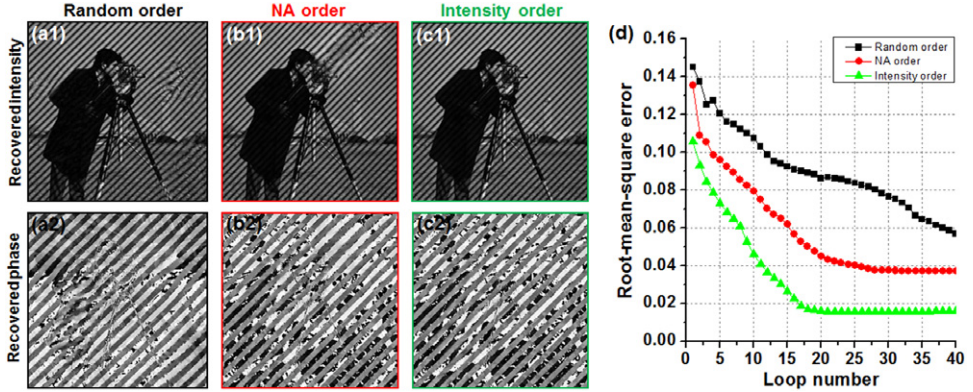


Figure 2.22. FP reconstructions using different updating sequences. The sample image is modulated by a sinusoidal pattern and the energy concentrates at two off-center positions in the Fourier domain. The FP reconstructions using the random order (a), the illumination-NA order (b), and the total-energy order (c). (d) The RMS error of the FP reconstructions versus the iteration loop number. Adapted from [41].

2.6 State-multiplexing in FP

In previous sections, our discussions are limited to modeling a single coherent state for each acquired image. In other words, the light source in our discussions is assumed to be spatially a point source and temporally a single wavelength. Incoherent mixture of multiple coherent states has not been considered in the FP recovery process. To this end, it is important to develop a recovery framework to handle coherent-state mixture and perform information multiplexing in FP experiments.

Figure 2.23 demonstrates the state-multiplexed FP framework [51], which is developed based on the mixed-state decomposition framework in real-space ptychography [52, 53]. Similar to the single-state scheme, it starts with a high-resolution estimate of the sample profile: $\sqrt{I_h} e^{i\phi_h}$. This sample estimate is used to generate multiple low-resolution target images corresponding to different coherent states. Second, the intensity components of the target images are summed up to generate the incoherent mixture I_t . Third, the ratio between the actual measurement I_m and I_t is used to update the intensity components of the target images, while the phase components are kept unchanged. Fourth, the updated target images are used to modify the corresponding spectral regions of the sample estimate. Lastly, the entire process is repeated for all intensity measurements with different incident angles and iterated for several times until the solution converges. The computational cost of the state-multiplexed FP scheme is linearly proportional to the number of coherent states. For example, the computational time of two-state multiplexing is twice the single-state's computational time.

The key difference between the state-multiplexed FP framework and the single-state FP lies in the intensity replacement process. In the single-state FP, the intensity component of the target image is directly replaced by the actual measurement I_m while the phase component is kept unchanged. The state-multiplexed framework, on the other hand, uses the ratio between the incoherent mixture and the actual

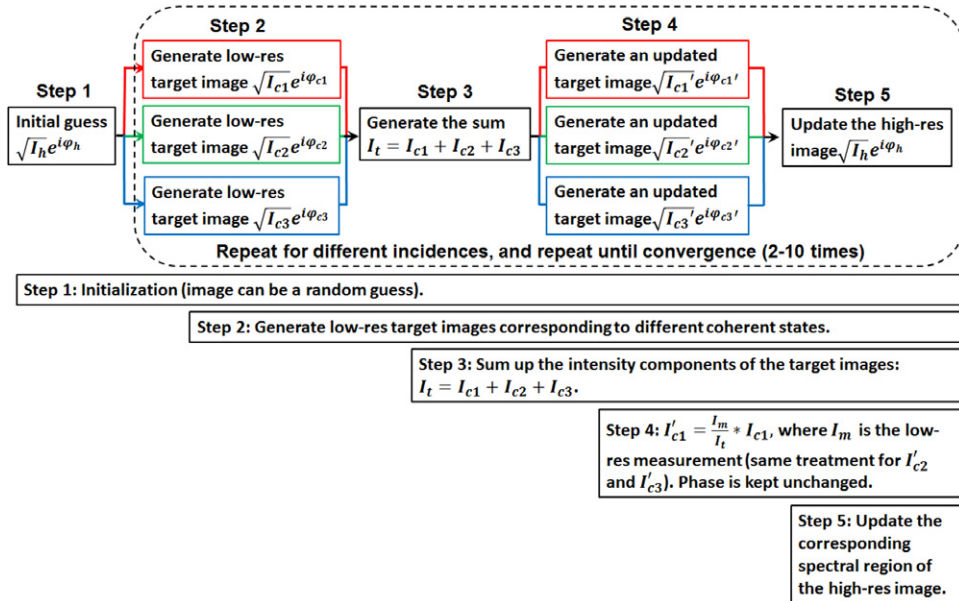


Figure 2.23. State-multiplexed FP framework. Adapted from [51].

measurement to update the intensity components of the target images. This new updating process ensures that the intensity summation of different coherent modes equates to the measured incoherent mixture, while the phase of individual modes is preserved [51].

The MATLAB code for the state-multiplexed FP is shown below. In this simulation code, we assume a color sample is illuminated by red, green, and blue LED elements at the same time. The captured images are, therefore, incoherent mixtures of three different coherent states. In the recovery process, we use the state-multiplexed FP to model the three coherent states and recover the high-resolution sample images at red, green, and blue channels. In lines 1–11, we generate the color object using the ‘Lenna’ image. In lines 12–18, we set up the coherent imaging system with three different wavelengths. In lines 19–30, we generate the wave vector for the LED array. Similar to previous simulations, we use a 15 by 15 LED matrix in this simulation.

```

1 % simulate the high resolution complex object
2 im=double(imread('Lenna.png'));
3 im=imresize(im,[256 256]);
4 objectAmplitude_r = padarray(im(:,:,1),[128 128]);
5 objectAmplitude_g = padarray(im(:,:,2),[128 128]);
6 objectAmplitude_b = padarray(im(:,:,3),[128 128]);
7 phase = double(imread('westconcordorthophoto.png'));
8 phase = imresize(phase,[512 512])./max(max(phase));
9 object_r = objectAmplitude_r.*exp(1i.* phase);
10 object_g = objectAmplitude_g.*exp(1i.* phase);
11 object_b = objectAmplitude_b.*exp(1i.* phase);
12 %% setup the parameters for the coherent imaging system
13 wavelength_r = 0.63e-6;k0_r = 2*pi/wavelength_r;
14 wavelength_g = 0.53e-6;k0_g = 2*pi/wavelength_g;
15 wavelength_b = 0.47e-6;k0_b = 2*pi/wavelength_b;
16 spsize = 2.5e-6; % sampling pixel size of the CCD

```

```

17 psize = spsize / 4; % final pixel size of the reconstruction
18 NA = 0.1;
19 %% create the wave vectors for the LED illumination
20 arraysize = 15;
21 xlocation = zeros(1,arraysize^2);
22 ylocation = zeros(1,arraysize^2);
23 LEDgap = 4; % 4mm between adjacent LEDs
24 LEDheight = 90; % distance between the LED matrix and the sample
25 for i=1:arraysize % from top left to bottom right
26     xlocation(1,1+arraysize*(i-1):15+arraysize*(i-1)) = (-(arraysize-
1)/2:1:(arraysize-1)/2)*LEDgap;
27     ylocation(1,1+arraysize*(i-1):15+arraysize*(i-1)) = ((arraysize-1)/2-
(i-1))*LEDgap;
28 end;
29 kx_relative = -sin(atan(xlocation/LEDheight));
30 ky_relative = -sin(atan(ylocation/LEDheight));

```

In the forward imaging model, we first generate the three sequences of low resolution images using three coherent transfer functions for different wavelengths: ‘imSeqLowRes_r’, ‘imSeqLowRes_g’, and ‘imSeqLowRes_b’. We then incoherently combine these images in line 90. As such, the resulting low-resolution image sequence ‘imSeqLowRes’ represents an incoherent mixture of three different coherent states.

```

31 %% generate the low-pass filtered images
32 [m,n] = size(object_r); % image size of high resolution object
33 m1 = m/(psize/psize);n1 = n/(psize/psize); % image size of the output
34 dkx = 2*pi/(psize*n);dky = 2*pi/(psize*m);
35 kmax = pi/psize;
36 [kxm kym] =
    meshgrid(-kmax:kmax/((n1-1)/2):kmax,-kmax:kmax/((n1-1)/2):kmax);
37 % red channel
38 kx_r = k0_r * kx_relative;
39 ky_r = k0_r * ky_relative;
40 imSeqLowRes_r
    = zeros(m1, n1, arraysize^2); % the final low resolution image sequence
41 cutoffFrequency_r = NA * k0_r;
42 CTF_r = double((kxm.^2+kym.^2)<cutoffFrequency_r^2);
43 % green channel
44 kx_g = k0_g * kx_relative;
45 ky_g = k0_g * ky_relative;
46 imSeqLowRes_g
    = zeros(m1, n1, arraysize^2); % the final low resolution image sequence
47 cutoffFrequency_g = NA * k0_g;
48 CTF_g = double((kxm.^2+kym.^2)<cutoffFrequency_g^2);
49 % blue channel
50 kx_b = k0_b * kx_relative;
51 ky_b = k0_b * ky_relative;
52 imSeqLowRes_b
    = zeros(m1, n1, arraysize^2); % the final low resolution image sequence
53 cutoffFrequency_b = NA * k0_b;
54 CTF_b = double((kxm.^2+kym.^2)<cutoffFrequency_b^2);
55 % the incoherent summation of the R,G,B channels
56 imSeqLowRes = zeros(m1, n1, arraysize^2);
57 %% forward imaging model
58 objectFT_r = fftshift(fft2(object_r));
59 objectFT_g = fftshift(fft2(object_g));
60 objectFT_b = fftshift(fft2(object_b));
61 for tt =1:arraysize^2
62     % red channel
63     kxc_r = round((n1+1)/2+kx_r(1,tt)/dkx);
64     kyc_r = round((m1+1)/2+ky_r(1,tt)/dky);
65     kyl_r = round(kyc_r-(m1-1)/2);
66     kyh_r = round(kyc_r+(m1-1)/2);
67     kx1_r = round(kxc_r-(n1-1)/2);
68     kxh_r = round(kxc_r+(n1-1)/2);
69     imSeqLowFT_r = (m1/m)^2 * objectFT_r(kyl_r:kyh_r,kx1_r:kxh_r).*CTF_r;

```

```

70 imSeqLowRes_r(:,:,tt) = abs(ifft2(ifftshift(imSeqLowFT_r)));
71 % green channel
72 kxc_g = round((n+1)/2+kx_g(1,tt)/dkx);
73 kyc_g = round((m+1)/2+ky_g(1,tt)/dky);
74 kyl_g = round(kyc_g-(m-1)/2);
75 kyh_g = round(kyc_g+(m-1)/2);
76 kxl_g = round(kxc_g-(n-1)/2);
77 kxh_g = round(kxc_g+(n-1)/2);
78 imSeqLowFT_g = (m\l/m)^2 * objectFT_g(kyl_g:kyh_g,kxl_g:kxh_g).*CTF_g;
79 imSeqLowRes_g(:,:,tt) = abs(ifft2(ifftshift(imSeqLowFT_g)));
80 % blue channel
81 kxc_b = round((n+1)/2+kx_b(1,tt)/dkx);
82 kyc_b = round((m+1)/2+ky_b(1,tt)/dky);
83 kyl_b = round(kyc_b-(m-1)/2);
84 kyh_b = round(kyc_b+(m-1)/2);
85 kxl_b = round(kxc_b-(n-1)/2);
86 kxh_b = round(kxc_b+(n-1)/2);
87 imSeqLowFT_b = (m\l/m)^2 * objectFT_b(kyl_b:kyh_b,kxl_b:kxh_b).*CTF_b;
88 imSeqLowRes_b(:,:,tt) = abs(ifft2(ifftshift(imSeqLowFT_b)));
89 % summation of R,G,B channels
90 imSeqLowRes(:,:,tt) =
91     imSeqLowRes_r(:,:,tt) + imSeqLowRes_g(:,:,tt)+ imSeqLowRes_b(:,:,tt);
92 end;
93 figure;imshow(imSeqLowRes(:,:,113),[]);

```

In the recovery process, we first initialize three high-resolution object images in lines 95–100. We then follow the recovery procedures in figure 2.23. In particular, we generate the incoherent summation of the three coherent states in line 123. This incoherent summation is then used to update the three coherent states in lines 124–129. In lines 130–132, we update the high-resolution object images using a similar procedure discussed in section 2.3.

```

93 %% Recover the high resolution images at R,G, and B channels
94 seq = gseq(arraysize);
95 objectRecover_r = ones(m,n);
96 objectRecoverFT_r = fftshift(fft2(objectRecover_r));
97 objectRecover_g = ones(m,n);
98 objectRecoverFT_g = fftshift(fft2(objectRecover_g));
99 objectRecover_b = ones(m,n);
100 objectRecoverFT_b = fftshift(fft2(objectRecover_b));
101 loop = 25;
102 for tt=1:loop
103     for i3=1:arraysize^2
104         i2=seq(i3);
105         kxc_r=round((n+1)/2-kx_r(1,i2)/dkx);
106         kyc_r=round((m+1)/2-ky_r(1,i2)/dky);
107         kxc_g=round((n+1)/2-kx_g(1,i2)/dkx);
108         kyc_g=round((m+1)/2-ky_g(1,i2)/dky);
109         kxc_b=round((n+1)/2-kx_b(1,i2)/dkx);
110         kyc_b=round((m+1)/2-ky_b(1,i2)/dky);
111         kyl_r=round(kyc_r-(m-1)/2);kyh_r=round(kyc_r+(m-1)/2);
112         kyl_g=round(kyc_g-(m-1)/2);kyh_g=round(kyc_g+(m-1)/2);
113         kyl_b=round(kyc_b-(m-1)/2);kyh_b=round(kyc_b+(m-1)/2);
114         kxl_r=round(kxc_r-(n-1)/2);kxh_r=round(kxc_r+(n-1)/2);
115         kxl_g=round(kxc_g-(n-1)/2);kxh_g=round(kxc_g+(n-1)/2);
116         kxl_b=round(kxc_b-(n-1)/2);kxh_b=round(kxc_b+(n-1)/2);
117         lowResFT_lr = (m\l/m)^2 *
118             objectRecoverFT_r(kyl_r:kyh_r,kxl_r:kxh_r).*CTF_r;
119         lowResFT_lg = (m\l/m)^2 *
120             objectRecoverFT_g(kyl_g:kyh_g,kxl_g:kxh_g).*CTF_g;
121         lowResFT_lb = (m\l/m)^2 *
122             objectRecoverFT_b(kyl_b:kyh_b,kxl_b:kxh_b).*CTF_b;
123         im_lowRes_r = ifft2(ifftshift(lowResFT_lr));
124         im_lowRes_g = ifft2(ifftshift(lowResFT_lg));
125         im_lowRes_b = ifft2(ifftshift(lowResFT_lb));
126         rbg_sum = sqrt(abs(im_lowRes_r).^2 +
127                         (abs(im_lowRes_g)).^2+(abs(im_lowRes_b)).^2);

```

```

124     im_lowRes_r = (m/m1)^2 * imSeqLowRes(:,:,i2).*  
125         abs(im_lowRes_r)./rbg_sum.*exp(1i.*angle(im_lowRes_r));  
126     lowResFT_2r = fftshift(fft2(im_lowRes_r)).*CTF_r;  
127     im_lowRes_g = (m/m1)^2 * imSeqLowRes(:,:,i2).*  
128         abs(im_lowRes_g)./rbg_sum.*exp(1i.*angle(im_lowRes_g));  
129     lowResFT_2g = fftshift(fft2(im_lowRes_g)).*CTF_g;  
130     im_lowRes_b = (m/m1)^2 * imSeqLowRes(:,:,i2).*  
131         abs(im_lowRes_b)./rbg_sum.*exp(1i.*angle(im_lowRes_b));  
132     lowResFT_2b = fftshift(fft2(im_lowRes_b)).*CTF_b;  
133     objectRecoverFT_r(kyl_r:kyh_r,kxl_r:kxh_r) =  
134         objectRecoverFT_r(kyl_r:kyh_r,kxl_r:kxh_r)+ conj(CTF_r)./  
135             (max(max(abs(CTF_r).^2))).*(lowResFT_2r - lowResFT_1r);  
136     objectRecoverFT_g(kyl_g:kyh_g,kxl_g:kxh_g) =  
137         objectRecoverFT_g(kyl_g:kyh_g,kxl_g:kxh_g)+ conj(CTF_g)./  
138             (max(max(abs(CTF_g).^2))).*(lowResFT_2g - lowResFT_1g);  
139     objectRecoverFT_b(kyl_b:kyh_b,kxl_b:kxh_b) =  
140         objectRecoverFT_b(kyl_b:kyh_b,kxl_b:kxh_b)+ conj(CTF_b)./  
             (max(max(abs(CTF_b).^2))).*(lowResFT_2b - lowResFT_1b);  
141     end;  
142 end;  
143 objectRecover_r=ifft2(ifftshift(objectRecoverFT_r));  
144 objectRecover_g=ifft2(ifftshift(objectRecoverFT_g));  
145 objectRecover_b=ifft2(ifftshift(objectRecoverFT_b));  
146 figure;imshow(abs(objectRecover_r),[]);  
147 figure;imshow(abs(objectRecover_g),[]);  
148 figure;imshow(abs(objectRecover_b),[]);

```

Figure 2.24 shows the simulation results using the above MATLAB code. High-resolution input images (the ground truth) at three different channels are shown in figure 2.24(a1)–(a3), and the corresponding color image is shown in figure 2.24(a4). The simulated low-resolution measurement is shown in figure 2.24(b), which represents the incoherent summation of three coherent states of the sample profiles. The reconstructed images using the state-multiplexed FP scheme are shown in figure 2.24(c1)–(c4). We can see that the state-multiplexed FP scheme is able to recover the high-resolution color image of the sample from state-mixed monochromatic measurements.

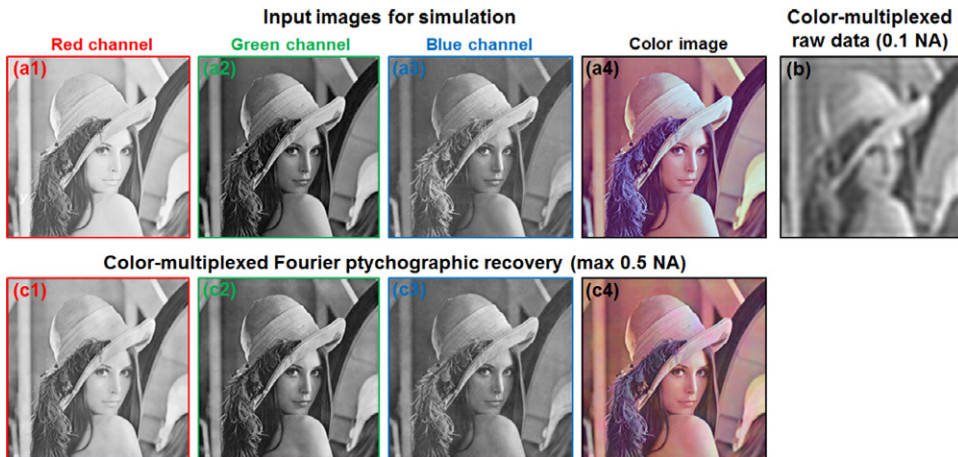


Figure 2.24. Simulations of the state-multiplexed FP scheme. (a) The input R/G/B channels and the combined color ground truth. (b) The low-resolution intensity measurement of the object, representing an incoherent summation of 3 object profiles at R/G/B wavelengths. (c) The state-multiplexed FP recovery with a 0.5 synthetic NA. Adapted from [51].

We also validated the state-multiplexed FP scheme using a light microscope experiment, as shown in figure 2.25. In this experiment, we used a pathology slide as the sample and turned on R/G/B LEDs simultaneously as the light source. Low-resolution images were acquired using a 0.1 NA objective lens and a monochrome camera. As such, the acquired images represent incoherent mixtures of sample profiles at three wavelengths, as shown in figure 2.25(a). The state-multiplexed FP algorithm was then used to decouple the R/G/B channels from the state-mixed measurements and recover the high-resolution color image of the sample. Figures 2.25(b1)–(b3) demonstrate the recovered images for the R/G/B channels, and the final color image is shown in figure 2.25(c). We also reconstructed the color image using three separated FP acquisitions (without state-mixing) in figure 2.25(d). As a comparison, the color image captured using a conventional 40 \times objective lens (0.6 NA) is shown in figure 2.25(e).

From this experiment, we can see that the state-multiplexed FP framework is able to successfully recover the high-resolution color image from the state-mixed measurements. We note that, under the same illumination intensity, the intrinsic image contrast for the blue channel is weaker than that of red and green channels. To address this problem, we can adjust the illumination intensity ratio between different wavelength components. The optimal intensity ratio may depend on the

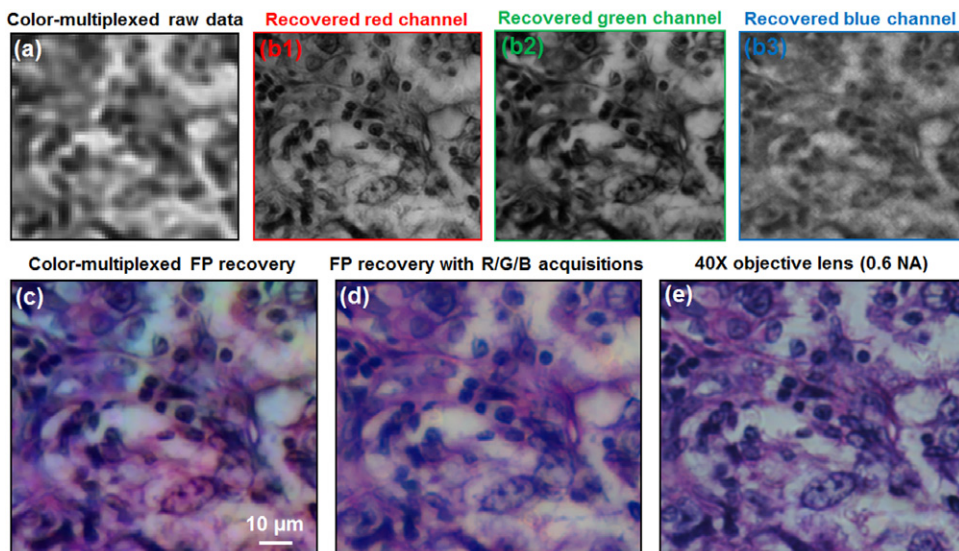


Figure 2.25. Experimental demonstration of the state-multiplexed FP framework. (a) The raw image of the state-multiplexed FP acquisition, representing incoherent summation of the sample profiles at R/G/B wavelengths. (b) The recovered high-resolution R/G/B images using the state-multiplexed FP framework. The final synthetic NA is 0.5. (c) The recovered color image by combining (b1)–(b3) (with white balance). (d) The recovered color image (0.5 synthetic NA) using three separated FP acquisitions with individual red, green, and blue illumination (no state-mixing). (e) The color image captured with a 40 \times high-NA objective lens (0.6 NA). Adapted from [51].

employed staining technique. Nevertheless, the experiment shown in figure 2.25 provides a solid proof for the state-multiplexed FP framework.

Finally, we note that, the state-multiplexed FP framework is not limited to modeling images at different wavelengths. It can be used to model the partially coherent effect of the employed light source. For example, the finite extent of the light source (related to spatial coherence) can be modeled as multiple point sources emitting light independently. The finite spectrum of the light source (related to temporal coherence) can be modeled as multiple light sources emitting light with different, but narrower passbands. The finite spatial extent or the emission band of the LED can be separated into different point sources or narrower passbands until no difference between adjacent states can be detected [51].

Bibliography

- [1] Lohmann A W, Dorsch R G, Mendlovic D, Zalevsky Z and Ferreira C 1996 Space-bandwidth product of optical signals and systems *JOSA A* **13** 470–3
- [2] Zheng G, Horstmeyer R and Yang C 2013 Wide-field, high-resolution Fourier ptychographic microscopy *Nat. Photonics* **7** 739–45
- [3] Zheng G, Ou X, Horstmeyer R, Chung J and Yang C 2014 Fourier Ptychographic Microscopy: A Gigapixel Superscope for Biomedicine *Opt. and Photonics News* 26–33
- [4] Zheng G 2014 Breakthroughs in Photonics 2013: Fourier Ptychographic Imaging *Photonics Journal, IEEE* **6** 1–7
- [5] Fienup J R 1982 Phase retrieval algorithms: a comparison *Appl. Opt.* **21** 2758–69
- [6] Elser V 2003 Phase retrieval by iterated projections *JOSA A* **20** 40–55
- [7] Faulkner H M L and Rodenburg J M 2004 Movable Aperture Lensless Transmission Microscopy: A Novel Phase Retrieval Algorithm *Phys. Rev. Lett.* **93** 023903
- [8] Maiden A M and Rodenburg J M 2009 An improved ptychographical phase retrieval algorithm for diffractive imaging *Ultramicroscopy* **109** 1256–62
- [9] Gonsalves R 1976 Phase retrieval from modulus data *JOSA* **66** 961–4
- [10] Fienup J R 1987 Reconstruction of a complex-valued object from the modulus of its Fourier transform using a support constraint *JOSA A* **4** 118–23
- [11] Candes E J, Strohmer T and Voroninski V 2013 Phaselift: Exact and stable signal recovery from magnitude measurements via convex programming *Comm. Pure Appl. Math.* **66** 1241–74
- [12] Candes E J, Eldar Y C, Strohmer T and Voroninski V 2015 Phase retrieval via matrix completion *SIAM Review* **57** 225–51
- [13] Waldspurger I, d'Aspremont A and Mallat S 2015 Phase recovery, maxcut and complex semidefinite programming *Math. Program.* **149** 47–81
- [14] Mico V, Zalevsky Z, García-Martínez P and García J 2006 Synthetic aperture super-resolution with multiple off-axis holograms *JOSA A* **23** 3162–70
- [15] Di J, Zhao J, Jiang H, Zhang P, Fan Q and Sun W 2008 High resolution digital holographic microscopy with a wide field of view based on a synthetic aperture technique and use of linear CCD scanning *Appl. Opt.* **47** 5654–9
- [16] Hillman T R, Gutzler T, Alexandrov S A and Sampson D D 2009 High-resolution, wide-field object reconstruction with synthetic aperture Fourier holographic optical microscopy *Opt. Exp.* **17** 7873–92

- [17] Granero L, Micó V, Zalevsky Z and García J 2010 Synthetic aperture superresolved microscopy in digital lensless Fourier holography by time and angular multiplexing of the object information *Appl. Opt.* **49** 845–57
- [18] Gutzler T, Hillman T R, Alexandrov S A and Sampson D D 2010 Coherent aperture-synthesis, wide-field, high-resolution holographic microscopy of biological tissue *Opt. Lett.* **35** 1136–8
- [19] Meinel A 1970 Aperture synthesis using independent telescopes *Appl. Opt.* **9** 2501
- [20] Turpin T, Gesell L, Lapides J and Price C 1995 Theory of the synthetic aperture microscope *Proc. SPIE* **2566** 230–40
- [21] Ryle M and Hewish A 1960 The synthesis of large radio telescopes *Mon. Not. R. Astron. Soc.* **120** 220
- [22] Hillman T R, Gutzler T, Alexandrov S A and Sampson D D 2009 High-resolution, wide-field object reconstruction with synthetic aperture Fourier holographic optical microscopy *Opt. Exp.* **17** 7873–92
- [23] Kim M, Choi Y, Fang-Yen C, Sung Y, Dasari R R and Feld M S *et al* 2011 High-speed synthetic aperture microscopy for live cell imaging *Opt. Lett.* **36** 148–50
- [24] Schwarz C J, Kuznetsova Y and Brueck S 2003 Imaging interferometric microscopy *Opt. Lett.* **28** 1424–26
- [25] Feng P, Wen X and Lu R 2009 Long-working-distance synthetic aperture Fresnel off-axis digital holography *Opt. Exp.* **17** 5473–80
- [26] Yuan C, Zhai H and Liu H 2008 Angular multiplexing in pulsed digital holography for aperture synthesis *Opt. Lett.* **33** 2356–8
- [27] Mico V, Zalevsky Z and García J 2007 Synthetic aperture microscopy using off-axis illumination and polarization coding *Opt. Comm.* **276** 209–17
- [28] Alexandrov S and Sampson D 2008 Spatial information transmission beyond a system's diffraction limit using optical spectral encoding of the spatial frequency *J. Optics A: Pure and Appl. Opt.* **10** 025304
- [29] Tippie A E, Kumar A and Fienup J R 2011 High-resolution synthetic-aperture digital holography with digital phase and pupil correction *Opt. Exp.* **19** 12027–38
- [30] Alexandrov S A, Hillman T R, Gutzler T and Sampson D D 2006 Synthetic aperture Fourier holographic optical microscopy *Phys. Rev. Lett.* **97** 168102
- [31] Ou X, Horstmeyer R, Yang C and Zheng G 2013 Quantitative phase imaging via Fourier ptychographic microscopy *Opt. Lett.* **38** 4845–8
- [32] Guizar-Sicairos M and Fienup J R 2008 Phase retrieval with transverse translation diversity: a nonlinear optimization approach *Opt. Exp.* **16** 7264–78
- [33] Li P, Batey D J, Edo T B and Rodenburg J M 2015 Separation of three-dimensional scattering effects in tilt-series Fourier ptychography *Ultramicroscopy* **158** 1–7
- [34] Hoppe W and Strube G 1969 Diffraction in inhomogeneous primary wave fields. 2. Optical experiments for phase determination of lattice interferences *Acta Crystallogr. A* **25** 502–7
- [35] Rodenburg J, Hurst A, Cullis A, Dobson B, Pfeiffer F and Bunk O *et al* 2007 Hard-x-ray lensless imaging of extended objects *Phys. Rev. Lett.* **98** 034801
- [36] Rodenburg J 2008 Ptychography and related diffractive imaging methods *Adv. Imag. Electr. Phys.* **150** 87
- [37] Horstmeyer R and Yang C 2014 A phase space model of Fourier ptychographic microscopy *Opt. Exp.* **22** 338–58

- [38] Ou X, Zheng G and Yang C 2014 Embedded pupil function recovery for Fourier ptychographic microscopy *Opt. Exp.* **22** 4960–72
- [39] Bian Z, Dong S and Zheng G 2013 Adaptive system correction for robust Fourier ptychographic imaging *Opt. Exp.* **21** 32400–10
- [40] Dong S, Guo K, Nanda P, Shiradkar R and Zheng G 2014 FPscope: a field-portable high-resolution microscope using a cellphone lens *Biomed. Opt. Exp.* **5** 3305–10
- [41] Guo K, Dong S, Nanda P and Zheng G 2015 Optimization of sampling pattern and the design of Fourier ptychographic illuminator *Opt. Exp.* **23** 6171–80
- [42] Bian L, Suo J, Situ G, Zheng G, Chen F and Dai Q 2014 Content adaptive illumination for Fourier ptychography *Opt. Lett.* **39** 6648–51
- [43] Huang X, Yan H, Harder R, Hwu Y, Robinson I K and Chu Y S 2014 Optimization of overlap uniformness for ptychography *Opt. Exp.* **22** 12634–44
- [44] Dong S, Horstmeyer R, Shiradkar R, Guo K, Ou X and Bian Z *et al* 2014 Aperture-scanning Fourier ptychography for 3D refocusing and super-resolution macroscopic imaging *Opt. Exp.* **22** 13586–99
- [45] Levoy M, Ng R, Adams A, Footer M and Horowitz M 2006 Light field microscopy *ACM Transactions on Graphics* **25** 924–34
- [46] Levoy M, Zhang Z and McDowall I 2009 Recording and controlling the 4D light field in a microscope using microlens arrays *J. Microsc.* **235** 144–62
- [47] Zheng G, Kolner C and Yang C 2011 Microscopy refocusing and dark-field imaging by using a simple LED array *Opt. Lett.* **36** 3987–9
- [48] Thibault P, Dierolf M, Bunk O, Menzel A and Pfeiffer F 2009 Probe retrieval in ptychographic coherent diffractive imaging *Ultramicroscopy* **109** 338–43
- [49] Dong S, Bian Z, Shiradkar R and Zheng G 2014 Sparsely sampled Fourier ptychography *Opt. Exp.* **22** 5455–64
- [50] Edo T B, Batey D J, Maiden A M, Rau C, Wagner U and Pešić Z D *et al* 2013 Sampling in x-ray ptychography *Phys. Rev. A* **87** 053850
- [51] Dong S, Shiradkar R, Nanda P and Zheng G 2014 Spectral multiplexing and coherent-state decomposition in Fourier ptychographic imaging *Biomedical Opt. Exp.* **5** 1757–67
- [52] Thibault P and Menzel A 2013 Reconstructing state mixtures from diffraction measurements *Nature* **494** 68–71
- [53] Batey D J, Claus D and Rodenburg J M 2014 Information multiplexing in ptychography *Ultramicroscopy* **138** 13–21

Fourier Ptychographic Imaging

A MATLAB® tutorial
Guoan Zheng

Chapter 3

Experimental implementations and imaging modalities of Fourier ptychography

In this chapter, we will discuss and review different experimental implementations of FP, including the LED-array approach, the liquid-crystal-display (LCD) approach, and the aperture-scanning approach. We will also discuss different imaging modalities using FP, including bright-field, dark-field, phase, phase-gradient, reflective, and multi-slice imaging.

3.1 Experimental implementations

3.1.1 LED-array illumination

The original FP prototype uses an LED array for sample illumination. The development of this platform can be traced back to the use of an LED array for 3D tomographic imaging in a conventional microscope platform [1, 2]. Different from the 3D tomographic imaging setup, the maximum incident angle of an FP setup needs to be much larger than the maximum collection angle of the employed objective lens. In other words, we capture a lot of dark-field images in an FP setup and these images contain high-frequency information of the sample.

Figures 3.1(a1) shows the FP prototype setup where we replace the condenser lens with a square LED array (32 by 32 LED array, Adafruit) [3]. Each LED element at the array illuminates the sample from a different incident angle. The distance between the adjacent LED elements is 4 mm and the distance between the LED array and the sample is ~90 mm. Images corresponding to different LED elements are then processed to recover a high-resolution complex image using the procedures in section 2.2. In this prototype setup, we used a 2×, 0.08 NA objective lens for image acquisition and the final synthetic NA is 0.5. By using this FP prototype platform, we are able to combine the field-of-view advantage of the 2× objective lens and the resolution advantage of the FP recovery process, as shown in figures 3.1(a2).

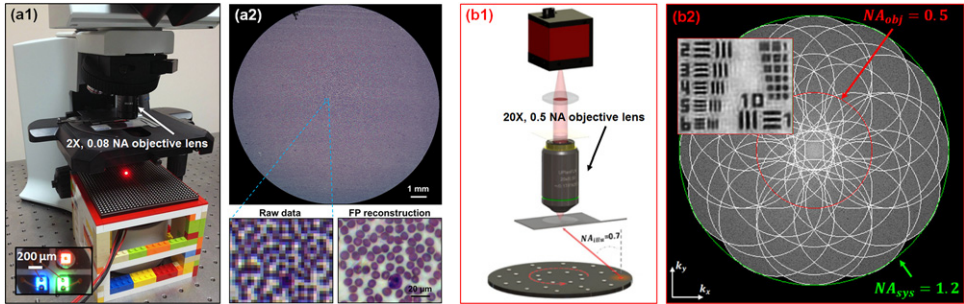


Figure 3.1. The FP prototype setup using LED-array illumination. (a1) The FP setup using a 2 \times , 0.08 NA objective lens. (a2) The recovered wide-field, high-resolution image of a blood smear sample. The final synthetic NA is 0.5. (b1) The FP setup using a 20 \times , 0.5 NA objective lens. (b2) The recovered high-resolution image of a resolution target. The final synthetic NA is \sim 1.2. Adapted from [3, 4].

We can also use a high-NA objective lens for image acquisition in an FP setup and apply the FP recovery process to further improve the resolution. As shown in figure 3.1(b), a 20 \times , 0.5 NA objective lens is used for image acquisition and the final synthetic NA is \sim 1.2 [4]. It has also been shown that, we can build a high-NA FP imaging platform using a 40 \times , 0.75 NA objective lens and an LED array with large incident angles; the achievable resolution of this high-NA FP platform is comparable to a conventional microscope platform with a 1.25 NA oil-immersion objective lens [4].

As we have discussed in section 2.4, an important consideration for implementing sample illumination is the sampling pattern in the Fourier space. In particular, we need to consider two factors: the overlapping percentage between adjacent Fourier apertures and the overlapping uniformity. For the square LED array used in figure 3.1(a), the sampling pattern is a periodic grid in the Fourier domain. Such a periodic sampling pattern leads to two problems in the FP implementation:

- 1) it requires a large number of raw images and a significant amount of aperture overlap ($>35\%$) in the Fourier space, and
- 2) it introduces raster-grid pathology problem in the reconstruction process [5, 6].

To address these problems, we can design a non-uniform sampling pattern using ring LEDs, as shown in figure 3.2(a)–(c). In this case, the aperture overlapping percentage decreases from \sim 50% at the center of the Fourier space to \sim 15% at the edge. This non-uniform sampling pattern also departs from the translational symmetry of Fourier-space sampling, and thus, it solves the raster-grid pathology problem in the FP recovery process. Figure 3.2(b) and (c) show the design of the ring-LED illuminator. Figures 3.2(d)–(f) compare the FP reconstruction using the square LED matrix and that using the non-uniform ring-LED illuminator. For both cases, we used 68 LED elements for sample illumination and the final synthetic NA is \sim 0.55. We can see that we can achieve a better reconstruction quality with fewer image acquisitions using the non-uniform ring-LED illuminator [6].

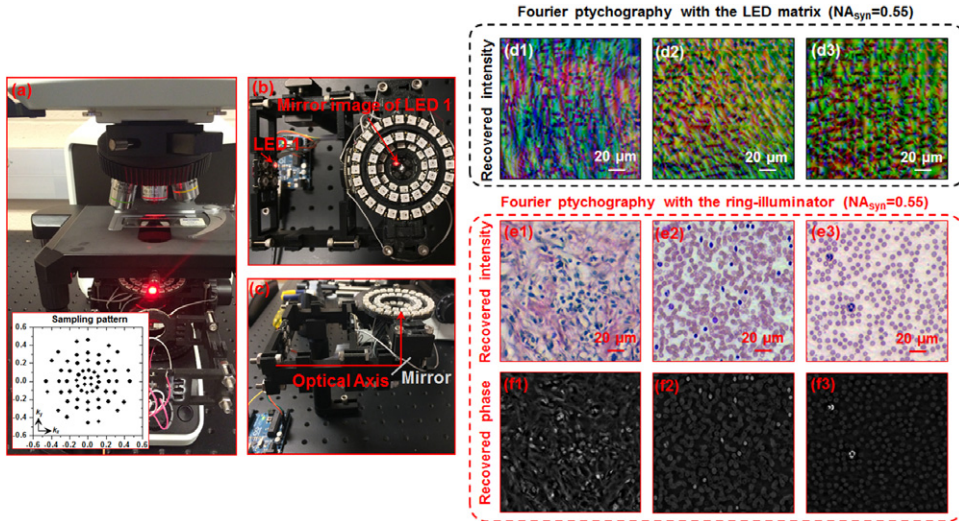


Figure 3.2. The FP setup using ring-LED illuminator. (a) An optimized ring-LED illuminator with 68 elements was used for sample illumination. This ring-LED illuminator corresponds to a non-uniform sampling pattern in the Fourier domain and reduces the number of image acquisitions by at least 50%. It also departs from the translational symmetry of Fourier-space sampling and solves the raster-grid pathology problem. The top view (b) and side view (c) of the ring-LED illuminator. 4 LED elements and an LED ring were mounted far away from the sample to achieve a higher sampling density in low-frequency regions of the Fourier space. (d) The recovered FP images using an LED matrix with 68 elements. (e)–(f) The recovered FP images using the ring-LED illuminator with 68 elements. Adapted from [6].

In FP platforms, the achievable resolution is determined by the largest incident angle and lens aberrations can be corrected in the iterative recovery process. Therefore, we can use low-resolution, low-quality optics to achieve high-resolution microscopy performance. Figure 3.3 shows an implementation of FP using an 8 by 8 LED array and a cellphone lens [7]. Each LED element of the array illuminates the sample from an oblique incident angle and the corresponding image is acquired using the cellphone lens with a 0.15 NA. The final synthetic NA of the recovered image is ~ 0.5 . Figure 3.3(b) shows the raw image captured using this platform. Figure 3.3(c) shows the FP recovered intensity, phase, and color images of the sample. With the rapid development of mobile hardware, we envision that the FP technique can be implemented on mobile platforms for providing healthcare accesses in resource-limited environments.

3.1.2 Liquid crystal display (LCD) for illumination modulation

Implementing FP using an LED array is a simple and cost-effective solution for many applications. However, there are also some disadvantages associated with it [8]:

- 1) the light emitted from the LED element is not a plane wave. In the recovery process, we need a plane wave approximation by splitting the entire image into small tiles.

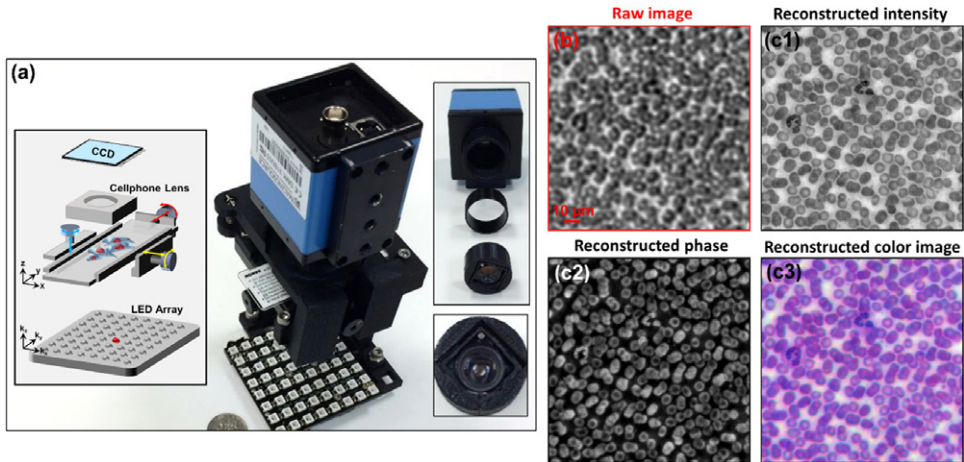


Figure 3.3. The FP setup using a small LED matrix and a cell-phone lens. (a) A Nokia cellphone lens was fitted into a plastic case and assembled with a CCD camera. A manual stage was assembled using 3D-printed parts. (b) The raw image captured using the 0.15 NA cellphone lens. (c) The FP recovered intensity, phase, and color images of the sample. The synthetic NA is ~ 0.5 . Adapted from [7].

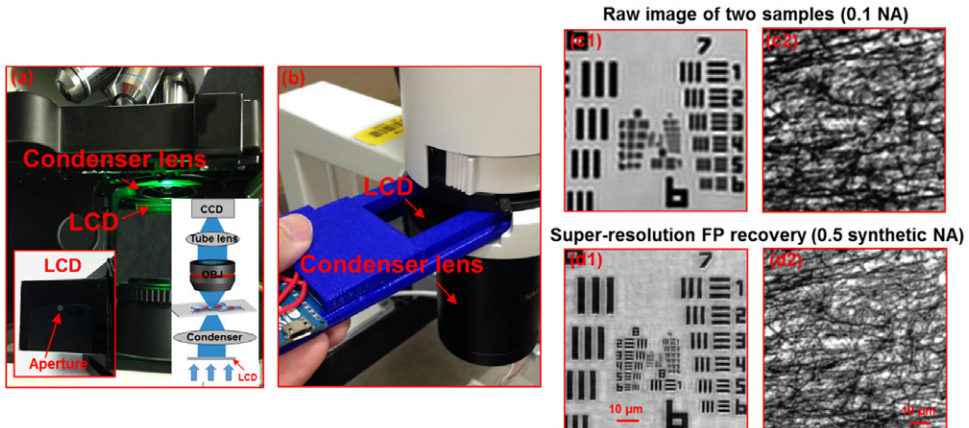


Figure 3.4. Implementing FP using a liquid crystal display (LCD). An LCD can be inserted at the back focal plane of the condenser lens for illumination modulation. By setting a scanning aperture pattern on the LCD, we can effectively illuminate the sample from different incident angles. The experimental setups for an upright (a) and inverted microscope (b). (c) The raw images captured using the microscope platform with a 0.1 NA objective lens. (d) The FP reconstructions using the LCD-based illumination, with a synthetic NA of ~ 0.5 . Modified from [8].

- 2) The intensity from LED elements may fluctuate over time, introducing errors to the system.
- 3) The light delivering efficiency is very low for LED elements at the edge of the array, limiting the achievable resolution of the system.

One possible solution to address these technical problems is to use a liquid crystal display (LCD) as a transparent spatial light modulator for illumination modulation [8]. As shown in figure 3.4(a), we can simply insert a cost-effective LCD at the back focal plane of the condenser lens; no other modification is needed for the system. Different binary patterns can be set on the LCD for illumination engineering. For bright-field microscopy, we can set a circular pattern on the LCD. The diameter of the pattern can be adjusted to match to different NAs of the objective lenses. For dark-field microscopy, a complementary pattern can be shown on the LCD. In this case, the pixel transmission is turned off within the circle. Furthermore, we can also use the LCD-based platform for 3D tomographic imaging [8], similar to the original demonstration of LED-array microscope [1, 2].

For Fourier ptychographic imaging, we can set a scanning aperture at the LCD. Each position of the aperture produces a plane wave illumination for the sample. As such, we can illuminate the sample from different incident angles and synthesize all captured images using the FP recovery process. Figures 3.4(a) and (b) show the experimental implementations of the LCD-based illumination in an upright and inverted microscope. Figure 3.4(c) shows the raw FP images using a 0.1 NA objective lens. Figure 3.4(d) shows the FP reconstructions, where the synthetic NA is ~ 0.5 .

There are several advantages of using LCD for illumination modulation. First, it is cost-effective and compatible with most existing compound microscopes. The only modification is the addition of a low-cost LCD at the condenser diaphragm. Second, the LCD provides a large degree of freedom for illumination engineering. For example, a typical LCD has more than 400 pixels per inch, which is the equivalent of 800 by 800 pixels over the condenser diaphragm of ~ 2 inches. This provides orders of magnitude improvement in degrees of freedom over the LED-array approach. Third, in the LCD-based illumination scheme, the light from the condenser lens is plane waves modulated by the LCD. In contrast, the LED-illumination approach essentially produces an array of spherical-waves, necessitating a plane wave approximation by splitting the entire image into small tiles [5]. Fourth, since we can set the aperture to any position on the LCD, the non-uniform sampling scheme discussed in section 2.4 can be directly implemented without rearranging the LED positions. Fifth, the intensity of the light source in the LCD-modulation scheme does not fluctuate as we set different patterns on the display. For the LED-array approach, one needs to calibrate the intensity differences between different LED elements and the intensity fluctuations over time.

One limitation of the LCD-based illumination scheme is the low extinction ratio of the LCD. To this end, an LCD with better polarizers can be used or two LCDs can be placed in series to increase the extinction ratio. We can also combine the LED-array approach with the LCD-modulation approach by putting a high-power LED array at the back focal plane of the condenser lens. The LCD can be placed on top of the LED array for modulating the light emission and increasing the spatial coherence.

3.1.3 Aperture-scanning FP for holographic imaging and remote sensing

In previous sections, we have discussed how to generate angle-varied plane waves for sample illumination. However, they share a major limitation: the sample needs to be thin [3]. Only under this assumption can the captured low-resolution images under different incident angles be uniquely mapped to different passbands of the 2D Fourier spectrum, allowing the FP algorithm to accurately impose the panning spectrum constraint to recover a high-resolution complex sample image. If the sample is not thin, this one-to-one mapping relationship in the Fourier plane is invalid, and the panning spectrum constraint cannot be imposed [9]. Fortunately, angle-varied illumination is not the only way to capture shifted versions of a sample's Fourier spectrum. We can, instead, illuminate the sample with one plane wave and translate the aperture at the Fourier plane, as shown in figure 3.5(a). In this case, we are recovering the complex wavefront exiting the sample. Therefore, the sample thickness is irrelevant for the FP recovery process and it allows us to circumvent the thin sample assumption noted above. The recovered complex light field can also be back-propagated to any plane along the optical axis to perform 3D holographic imaging. We call this scheme ‘aperture-scanning FP’ [9].

Figures 3.5(a)–(c) show the aperture-scanning FP prototype setup, where we used two photographic lenses to form a 4f system and placed a circular aperture at its Fourier plane. In this prototype setup, we used a mechanical stage to scan the aperture stop. One can also insert an LCD at the Fourier plane and digitally set a scanning pattern. For each scanning position of the aperture, we captured one low-resolution image of the sample. We then used the FP recovery process to produce a high-resolution complex image of the sample. Figure 3.5(d) shows the raw image of a tilted slide sample. Figure 3.5(e) shows the recovered high-resolution complex light

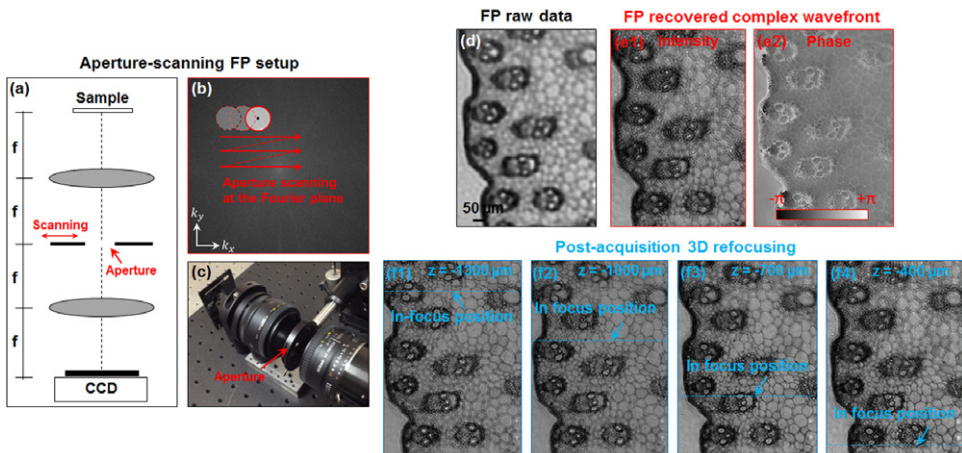


Figure 3.5. Aperture-scanning FP. (a) The schematic diagram. (b) A circular aperture was placed at the Fourier plane of a 4f system and scanned to different positions. (c) The prototype setup. (d) The raw intensity image of a tilted slide. (e) The recovered intensity and phase images of the tilted slide. The refocused images at (f1) $z = -1300 \mu\text{m}$, (f2) $z = -1000 \mu\text{m}$, (f3) $z = -700 \mu\text{m}$, and (f4) $z = -400 \mu\text{m}$. Modified from [9].

field of the sample. Similar to other holographic imaging techniques, we can propagate the recovered complex light field to any plane along the optical axis. Figure 3.5(f) demonstrates the refocused images after the digital propagating process. For example, in figure 3.5(f1), we propagated the recovered complex light field by -1.3 mm axially. As the sample was tilted with respect to the optical axis, different spatial regions of the sample were brought into focus in figure 3.5(f1)–(f4).

The key innovation of the aperture-scanning FP scheme is to impose an aperture constraint at the Fourier plane. This simple concept, in fact, can be directly implemented in a macroscopic imaging setting. Figures 3.6(a) and (b) demonstrate a camera-scanning FP setup, where the object is placed at the far field and the camera is scanned over different x – y positions to acquire images corresponding to different Fourier passbands. We note that far field propagation is equivalent to performing a Fourier transform of the light field. Therefore, the aperture of the camera lens naturally serves as a support constraint at the Fourier plane. By scanning the entire camera to different x – y positions, we are able to synthesize a large passband in the Fourier space, and thus, bypass the resolution limit imposed by the lens’s aperture. The final achievable resolution in this case is determined by how far we can move the camera, not by the size of the lens’s aperture. Figure 3.6(c) shows the raw image captured by the camera and the resolution is limited by the lens’s aperture. Figure 3.6(d) shows the recovered high-resolution image using the FP recovery process and the achievable resolution is determined by the scanning distance of the entire camera. The camera-scanning scheme extends the FP

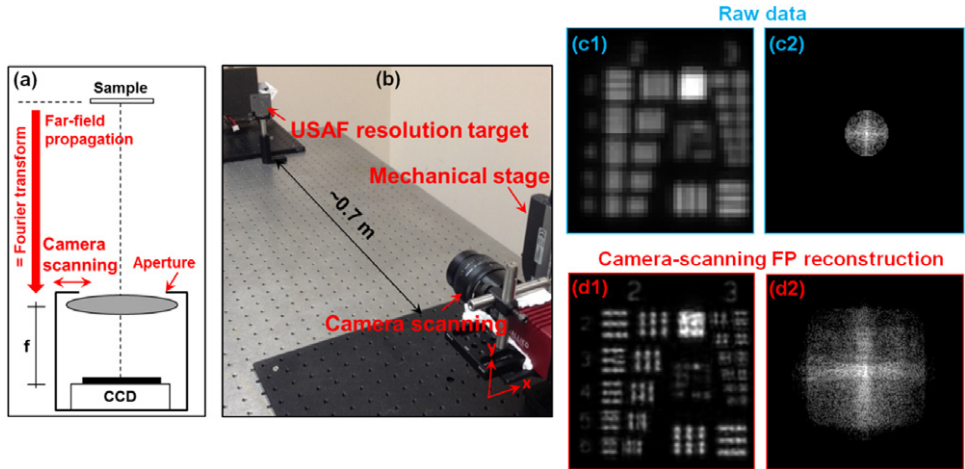


Figure 3.6. Camera-scanning FP. (a) The sample is placed at the far field and the aperture of the camera lens naturally serves as a confined support constraint in the Fourier plane. By scanning the entire camera to different positions, we can synthesize a larger passband in the Fourier space, enabling super-resolution imaging beyond the resolution limit of the lens’s aperture. (b) The experimental setup where a mechanical stage was used to scan the entire camera at the x – y plane. The raw image of the object directly captured by the camera (c1) and the corresponding Fourier spectrum (c2). The recovered image using the camera-scanning FP (d1) and the corresponding Fourier spectrum (d2). Modified from [9].

framework for macroscopic imaging settings. We envision its applications in remote sensing and other defense-related applications.

3.1.4 Other implementations

There are also other implementations of the FP concept. For example, it can be implemented without using lenses. In this case, the object is directly placed on top of an image sensor and illuminated with angle-varied plane waves. The recovery process switches between the spatial domain (the plane of the image sensor) and the Fourier domain. In the spatial domain, the intensity measurement is used as a magnitude constraint for the solution. In the Fourier domain, the coherent transfer function is used as the confined aperture support constraint for the solution. Once the high-resolution complex field at the detector plane is recovered, one can digitally propagate it to the object plane and recover the high-resolution complex image of the object. The interested reader can refer to the ‘lensfree imaging using synthetic aperture (LISA)’ platform demonstrated by Professor Ozcan’s group at UCLA [10].

In a typical FP platform, we need to capture multiple images of the sample under different incident angles. It is also possible to perform single-shot FP implementation using two microlens arrays. The interested reader can refer to [11] for more details.

3.2 Imaging modalities of FP

3.2.1 Bright-field, phase, and phase-gradient imaging

The FP reconstruction process is able to recover both the intensity and phase information of the sample. As such, we can perform bright-field and phase imaging using FP. Figure 3.7(a) shows the raw intensity images of two biological samples.

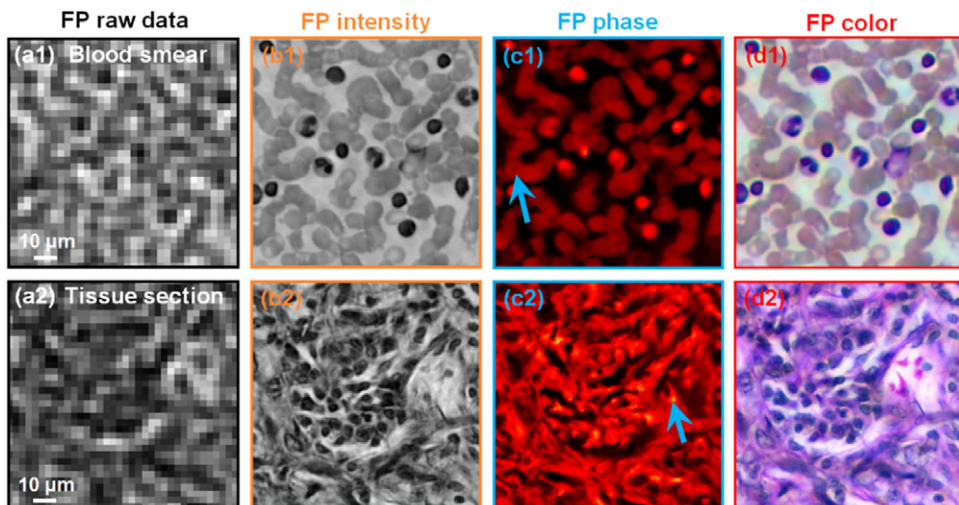


Figure 3.7. Bright-field and phase imaging using FP. (a) The raw images captured using a 2 \times , 0.08 NA objective lens. The recovered high-resolution bright-field (b), phase (c), and color images (d) using FP. Adapted from [3, 16].

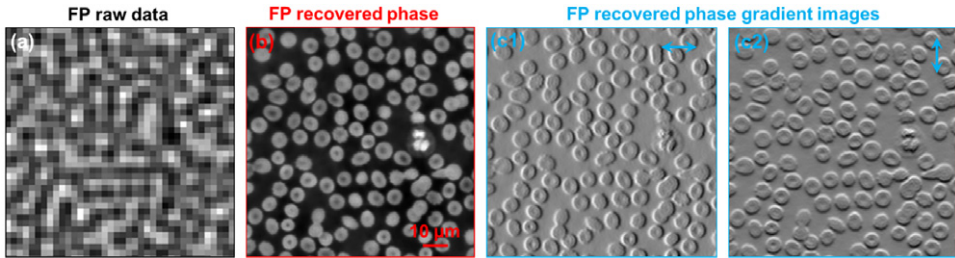


Figure 3.8. Phase and phase-gradient imaging using FP. (a) The raw FP image. (b) The recovered phase image. (c) The FP-generated phase-gradient images, simulating the appearance of the conventional DIC microscope. Adapted from [12].

Figures 3.7(b) and (c) demonstrate the recovered high-resolution bright-field and phase images using FP. We can also use three different wavelengths (R/G/B) for sample illumination and recover three bright-field images at R/G/B channels. Figure 3.7(d) shows the combined high-resolution color images of the samples. The blue arrows in figure 3.7(c) identify regions where phase maps can provide additional sample information. These features cannot be seen from the intensity reconstructions. It has also been shown that the phase information recovered by FP is quantitative in nature [12]. Combining with its wide-field-of-view imaging capability, phase imaging using FP may find applications in blood testing [13], tissue screening [14], and disease diagnosis [15].

Once we recover the phase information of the sample, we can also generate phase gradient images, as shown in figure 3.8(c). The generated phase gradient images simulate the improved visibility of a differential-interference-contrast (DIC) microscopy; however, they are quantitative in nature as compared to the conventional DIC microscopy.

Figure 3.9 further demonstrates the phase imaging modality on a transparent biological sample (an unstained mouse kidney slide). It is difficult to resolve sample details from the FP recovered intensity image; however, we can clearly resolve individual cells from the FP recovered phase image. Figure 3.9 also raises a question on why we can recover the phase information of a transparent sample with intensity-only measurements. To answer this question, we may need to revisit the image acquisition process of FP, where we use angle-varied plane wave for sample illumination. In this process, when the illumination NA is less than the collection NA of the objective lens, the captured brightfield images are in low contrast and contain little information of the phase profile. However, when the illumination NA is larger than the collection NA, we capture dark-field images that are related to the scattering property of the transparent sample. The phase information is encoded in these dark-field intensity images.

3.2.2 Dark-field imaging

In bright-field FP imaging, we need to illuminate the sample from small incident angles to large incident angles. The corresponding images are then synthesized in the Fourier space and the recovered high-resolution image contains all Fourier

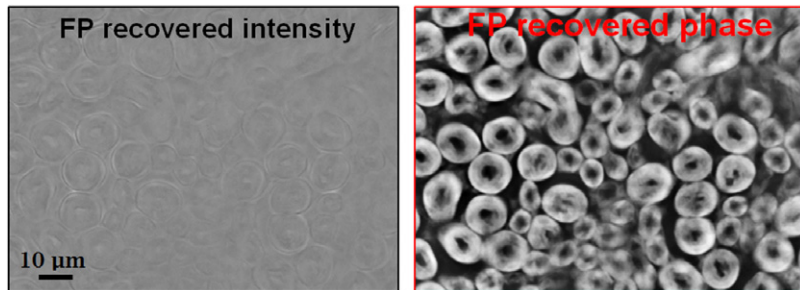


Figure 3.9. Comparison between the FP-recovered intensity and phase images of a transparent sample (unstained mouse kidney cells). Adapted from [17].

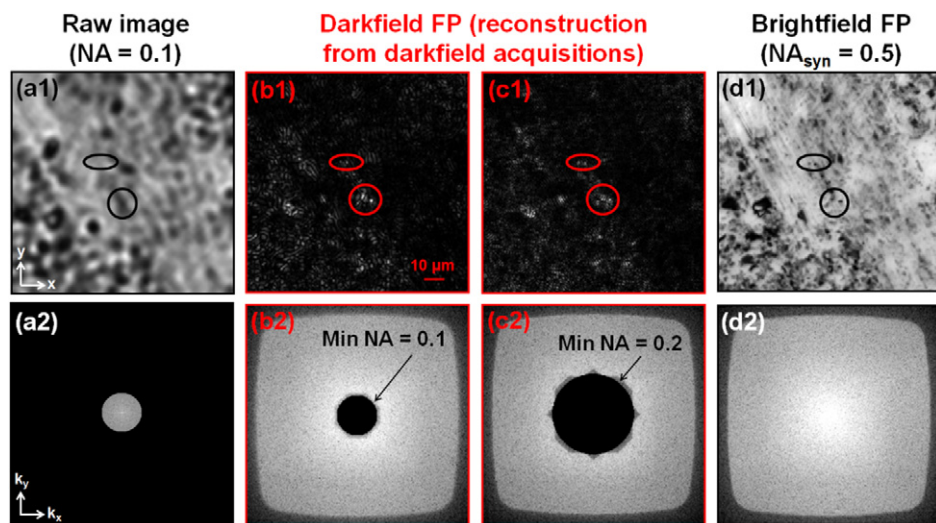


Figure 3.10. Dark-field FP. (a1) The raw bright-field image captured using a 0.1 NA objective lens. (a2) The corresponding Fourier spectrum of (a1). Dark-field FP recovery using raw images with an illumination NA higher than 0.2 (b1) and 0.3 (c1). (b2) and (c2): Fourier spectra of (b1) and (c1). (d1) The bright-field FP recovery using both bright-field and dark-field raw images. (d2) The corresponding Fourier spectrum of (d1), with a synthetic NA of 0.5. Detailed features are highlighted in (a1)–(d1) for comparison. Adapted from [17].

components within the synthetic passband. It raises a question: is this full-passband coverage necessary for FP imaging? For many applications, we only care about the high-frequency components in the Fourier space, as these components represent the detailed information of the sample. Therefore, a logical development of FP is to selectively capture images in the Fourier space to shorten the acquisition time. One example to this end is the dark-field FP scheme where we only capture dark-field raw images in the acquisition process.

Figure 3.10 demonstrates the result of the dark-field FP scheme using a glass slide deposited with carbon particles. Figures 3.10(a1) and (a2) show the raw bright-field image captured with a 0.1 NA objective lens and its Fourier spectrum.

In figure 3.10(b), we use raw dark-field images with an illumination NA higher than 0.2 to perform FP recovery. In figure 3.10(c), we use raw dark-field images with an illumination NA higher than 0.3 to perform FP recovery. The empty regions in figures 3.10(b2) and (c2) correspond to low-frequency components of the sample, and the final synthetic NA for both figures is 0.5. As a comparison, we also show the bright-field FP recovery in figure 3.10(d), where we have full spectrum coverage across the entire synthetic passband. In figure 3.10(a1)–(d1), we also highlight small features of the sample for comparison. From this comparison, we can identify the small details of the sample from both the dark-field and bright-field FP recoveries.

Dark-field FP is a simple extension of the bright-field FP. However, it has the potential to perform high-resolution, high-throughput microscopy imaging with ultra large field of view. For example, we can use a low-NA lens for image acquisition and use plane waves with large incident angles for sample illumination. The recovered dark-field FP image only contains detailed information of the sample; the low-frequency components will not be presented. The dark-field FP imaging modality may find applications in surface inspection, where we aim to identify small features of the sample over a large field of view and in high-throughput [17].

3.2.3 Reflective imaging

Transmitted light microscopes cannot handle opaque or reflective specimens such as metallic surfaces, silicon wafer, and integrated circuits. As a result, reflected light microscopes have been developed to image these specimens using an epi-illumination configuration. Reflected light microscopes have found important industrial applications in wafer inspection, metallography and metrology.

The FP imaging scheme can also be implemented in an epi-illuminated mode for reflective imaging [17, 18]. We term it epi-illuminated FP (eFP). The schematic of the eFP setup is shown in figure 3.11, where we use two LED rings for sample illumination and a 10 \times (0.28 NA) objective lens for image acquisition. Similar to the conventional epi-illumination platform, we used a beam splitter to separate the illumination path and the detection path. The first LED ring was mounted at the epi-illumination arm of the microscope platform. The emitted light from different elements of this LED ring was focused at different off-axis positions of the objective's back-focal plane. The light wave exiting from the objective thus illuminated the sample from different oblique incident angles. The second LED ring was mounted outside the employed objective lens. This LED ring thus illuminated the sample with an illumination NA higher than the collection NA of the employed optics. This second LED ring gives us the true super-resolution imaging performance (better than the incoherent diffraction limit of the employed lens).

To operate the eFP platform, we simply turn on the LED elements one after the other and acquire the corresponding raw images of the sample. In the prototype platform shown in figure 3.11, we used 8 elements at the first LED ring and 16 elements at the second ring. Based on all acquired images (24 in this setup), we can then recover the high-resolution sample image. Figure 3.12(a) shows the raw image captured by the eFP platform and figure 3.12(b) shows the recovered images. In figure 3.12(b1), the

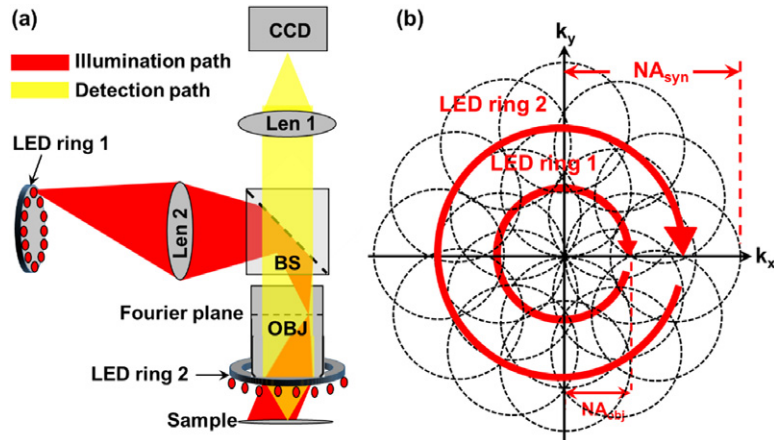


Figure 3.11. Epi-illuminated FP (eFP). (a) Schematic of the optical setup. Two LED rings were used for sample illumination. The first LED ring was mounted at the epi-illumination arm of the platform. The emitted light from this LED ring was focused at off-axis positions of the objective's back-focal plane. The second LED ring was mounted outside the objective lens. (b) The captured images were synthesized in the Fourier domain to produce a final image with three times higher NA for coherent imaging (1.5 times better resolution than the incoherent diffraction limit). Adapted from [17].

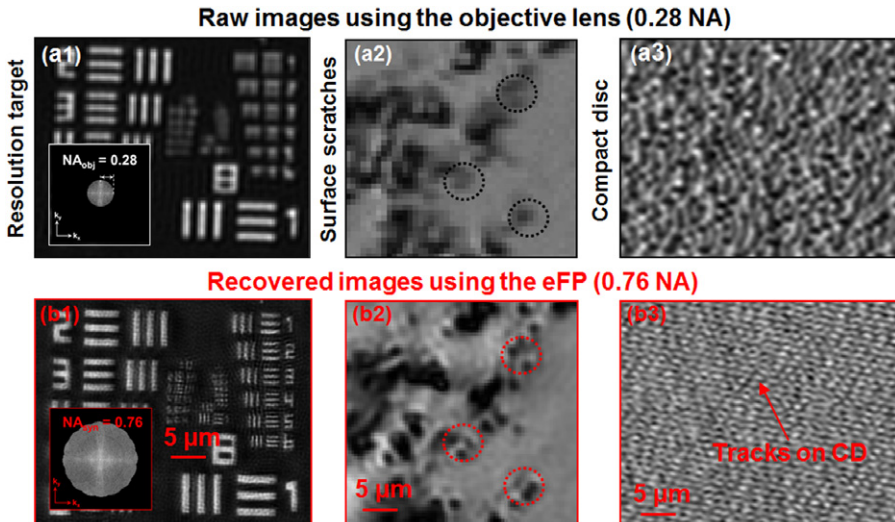


Figure 3.12. Imaging performance of the eFP platform. (a) Raw images of a resolution target, a silicon wafer, and a compact disc. (b) eFP-recovered images with a 0.76 synthetic NA. Adapted from [17].

390 nm linewidth of group 10, element 3 can be clearly resolved. The final synthetic NA is about three times higher than the NA of the employed objective lens in a coherent imaging setting (i.e. 1.5 times better resolution than the incoherent diffraction limit). We also tested the eFP platform with two reflective samples, a silicon wafer with

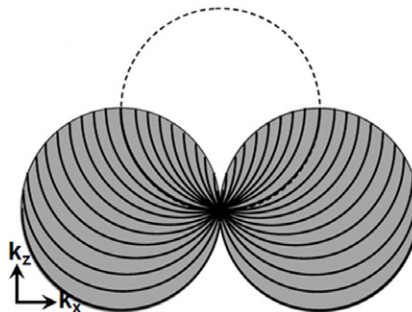


Figure 3.13. The accessible Fourier-space volume by the multi-slice FP. Modified from [21].

scratches and a compact disc. Figures 3.12(a2) and (a3) show the raw images of these two samples. Figures 3.12(b2) and (b3) show the eFP recovered images, where we can resolve small features of the samples that are not presented in the raw images.

The eFP scheme can be readily employed in most existing epi-illuminated imaging platforms without major hardware modifications. It also provides useful insights for the development of reflective imaging platforms using low-NA optics. In particular, we can combine the advantages of low-NA optics (large field-of-view, long working distance etc) with the high-resolution imaging capability for wafer inspection. We can also combine the dark-field FP modality with the epi-illumination configuration for high-resolution, high-throughput reflective imaging.

3.2.4 Multi-slice imaging

In the development of real-space ptychography technique, multi-slice modeling has been proposed for recovering sample information at multiple layers along the optical axis [19]. Confocal-type images have been demonstrated for 3D biological samples using the multi-slice ptychography [20]. Due to the close relationship between the real-space ptychography and the FP, the developments in real-space ptychography can be directly applied to the FP platforms. By modeling the sample using the multi-slice approach [19, 20], FP can be used to recover high-resolution images of a sample that contains multiple layers [21, 22]. In this multi-slice imaging modality, the accessible volume in the Fourier space is a doughnut with a cross-section corresponding to two discs of the diameter of the Ewald sphere, as shown in figure 3.13 [21]. This accessible volume is the same as the 3D transfer function of the conventional incoherent microscope platform [23].

Bibliography

- [1] Zheng G, Kolner C and Yang C 2011 Microscopy refocusing and dark-field imaging by using a simple LED array *Opt. Lett.* **36** 3987–9
- [2] Zheng G 2012 Microscopy-Programmable LED array makes microscopes more versatile *Laser Focus World* **48** 66
- [3] Zheng G, Horstmeyer R and Yang C 2013 Wide-field, high-resolution Fourier ptychographic microscopy *Nature Photonics* **7** 739–45

- [4] Ou X, Horstmeyer R, Zheng G and Yang C 2015 High numerical aperture Fourier ptychography: principle, implementation and characterization *Opt. Exp.* **23** 3472–91
- [5] Thibault P, Dierolf M, Bunk O, Menzel A and Pfeiffer F 2009 Probe retrieval in ptychographic coherent diffractive imaging *Ultramicroscopy* **109** 338–43
- [6] Guo K, Dong S, Nanda P and Zheng G 2015 Optimization of sampling pattern and the design of Fourier ptychographic illuminator *Opt. Exp.* **23** 6171–80
- [7] Dong S, Guo K, Nanda P, Shiradkar R and Zheng G 2014 FPscope: a field-portable high-resolution microscope using a cellphone lens *Biomed. Opt. Exp.* **5** 3305–10
- [8] Guo K, Bian Z, Dong S, Nanda P, Wang Y M and Zheng G 2015 Microscopy illumination engineering using a low-cost liquid crystal display *Biomed. Opt. Exp.* **6** 574–9
- [9] Dong S, Horstmeyer R, Shiradkar R, Guo K, Ou X and Bian Z *et al* 2014 Aperture-scanning Fourier ptychography for 3D refocusing and super-resolution macroscopic imaging *Opt. Exp.* **22** 13586–99
- [10] Luo W, Greenbaum A, Zhang Y and Ozcan A 2015 Synthetic aperture-based on-chip microscopy *Light: Science & Applications* **4** e261
- [11] Sidorenko P and Cohen O 2016 Single-shot ptychography *Optica* **3** 9–14
- [12] Ou X, Horstmeyer R, Yang C and Zheng G 2013 Quantitative phase imaging via Fourier ptychographic microscopy *Opt. Lett.* **38** 4845–8
- [13] Mir M, Tangella K and Popescu G 2011 Blood testing at the single cell level using quantitative phase and amplitude microscopy *Biomed. Opt. Exp.* **2** 3259
- [14] Kim T, Sridharan S, Kajdacsy-Balla A, Tangella K and Popescu G 2013 Gradient field microscopy for label-free diagnosis of human biopsies *Appl. Opt.* **52** A92–A96
- [15] Wang Z, Tangella K, Balla A and Popescu G 2011 Tissue refractive index as marker of disease *J. Biomed. Opt.* **16** 116017–177
- [16] Zheng G 2014 Breakthroughs in Photonics 2013: Fourier Ptychographic Imaging *Photonics J. IEEE* **6** 1–7
- [17] Guo K, Dong S and Zheng G 2016 Fourier Ptychography for Brightfield, Phase, Darkfield, Reflective, Multi-slice, and Fluorescence Imaging, *IEEE J. Select. Topics Quant. Electr.* at press
- [18] Pacheco S, Zheng G and Liang R 2016 Reflective Fourier ptychography *J. Biomed. Opt.* **21** 026010
- [19] Maiden A M, Humphry M J and Rodenburg J M 2012 Ptychographic transmission microscopy in three dimensions using a multi-slice approach *J. Opt. Soc. Am.* **29** 1606–14
- [20] Godden T, Suman R, Humphry M, Rodenburg J and Maiden A 2014 Ptychographic microscope for three-dimensional imaging *Opt. Exp.* **22** 12513
- [21] Li P, Batey D J, Edo T B and Rodenburg J M 2015 Separation of three-dimensional scattering effects in tilt-series Fourier ptychography *Ultramicroscopy* **158** 1–7
- [22] Tian L and Waller L 2015 3D intensity and phase imaging from light field measurements in an LED array microscope *Optica* **2** 104–11
- [23] Sheppard C J R and Cogswell C J 1990 Three-dimensional image formation in confocal microscopy *J. Microsc.* **159** 179–94

Fourier Ptychographic Imaging

A MATLAB® tutorial
Guoan Zheng

Chapter 4

Extending Fourier ptychography for incoherent imaging

In the original FP implementation, we use angle-varied plane waves to encode the sample information into the intensity measurements. As a coherent imaging technique, the original FP approach cannot be used for incoherent imaging, such as fluorescence microscopy. The reason is very simple: **fluorophores are not responsive to phase variation of the excitation wave**. In the original FP setup, no matter which angle we illuminate the sample with, the fluorescence emission remains unchanged and no additional information can be extracted from the raw images. **To modify the FP recovery process for incoherent imaging, we can simply replace the angle-varied plane waves with intensity-varied patterns for sample illumination.** In this case, each low-resolution measurement carries additional information of the sample profile. Based on all measurements, we can then **recover the sample information beyond the frequency limit of the employed objective lens**. We term this scheme **pattern-illuminated FP**. Figure 4.1 outlines the strategies of using FP procedures for both coherent and incoherent imaging settings. In the following, we will first discuss the pattern-illuminated FP scheme (section 4.1) [1, 2]. We will then discuss how to reduce the number of acquisitions for resolution doubling (section 4.2) [3]. Finally, we will discuss how to recover higher dimensional information using multi-state FP modeling (section 4.3) [4].

4.1 Pattern-illuminated FP

The pattern-illuminated FP approach uses multiple non-uniform intensity pattern P_n ($n = 1, 2, 3\dots$) to illuminate the object I_{obj} and acquires the corresponding low-resolution images I_n ($n = 1, 2, 3\dots$) through the objective lens. **By illuminating the sample with non-uniform patterns, one can shift the high-frequency components lying outside the lens's aperture to the passband of the collection optics [6–14].** As

	Coherent FP	Incoherent FP
Step 1	Initialization $I_{obj}e^{i\phi}$	Initialization I_{obj}
Step 2	$I_{tn} = I_{obj}e^{i\phi} \cdot A e^{ikx}$	$I_{tn} = I_{obj} \cdot P_n$
Step 3	Update the image in the Fourier domain	
Step 4	Update the image in the spatial domain	
Step 5	Repeat for other illumination angles	Repeat for other illumination patterns
Step 6	Repeat step 2 - 5 until solution converges	

Figure 4.1. FP recovery procedures for coherent and incoherent imaging settings. For coherent imaging, plane waves with different incident angles are used to encode the sample information into the measurements. For incoherent imaging, different intensity patterns are used to encode the sample information into the measurements. Adapted from [5].

such, the recorded intensity images contain sample information that is beyond the diffraction limit. The forward imaging model of the pattern-illuminated FP scheme can be expressed as follows:

$$\mathcal{F}(I_n) = \text{OTF} \cdot \mathcal{F}(I_{obj} \cdot P_n) \quad (4.1)$$

where $\mathcal{F}(I_n)$ denotes the Fourier transform of the image, and OTF denotes the incoherent optical transfer function of the objective lens. There are two multiplication steps in equation (4.1): one in the spatial domain and one in the Fourier domain. In the spatial domain, the object profile is multiplied with the illumination pattern to produce a target image I_{tn} : $I_{tn} = I_{obj} \cdot P_n$. In the Fourier domain, the incoherent OTF is multiplied with the spectrum of the target image to produce the spectrum of the measurement: $\mathcal{F}(I_n) = \text{OTF} \cdot \mathcal{F}(I_{obj} \cdot P_n)$. To recover the high-resolution object profile I_{obj} , we need to invert these two multiplication steps in both the spatial and Fourier domains.

The pattern-illuminated FP scheme aims to recover the high-resolution object image I_{obj} from the low-resolution measurements I_n ($n = 1, 2, 3\dots$), as shown in figure 4.2. Here we assume the illumination pattern P_n is known. Later in this section we will extend the recovery framework to handle an unknown illumination pattern. The recovery process can be explained as follows.

Step 1: it starts with an initial guess of the sample profile I_{obj} . This initial guess can be an interpolation of one low-resolution measurement; it can also be a random guess.

Step 2: the initial guess is multiplied with the illumination pattern P_n to produce a target image I_{tn} in the spatial domain: $I_{tn} = I_{obj} \cdot P_n$.

Step 3: the target image I_{tn} is updated by the low-resolution measurement I_n in the Fourier domain using the following equation:

$$\mathcal{F}(I_{tn})^{\text{updated}} = \mathcal{F}(I_{tn}) + \text{OTF} \cdot (\mathcal{F}(I_n) - \text{OTF} \cdot \mathcal{F}(I_{tn})) \quad (4.2)$$

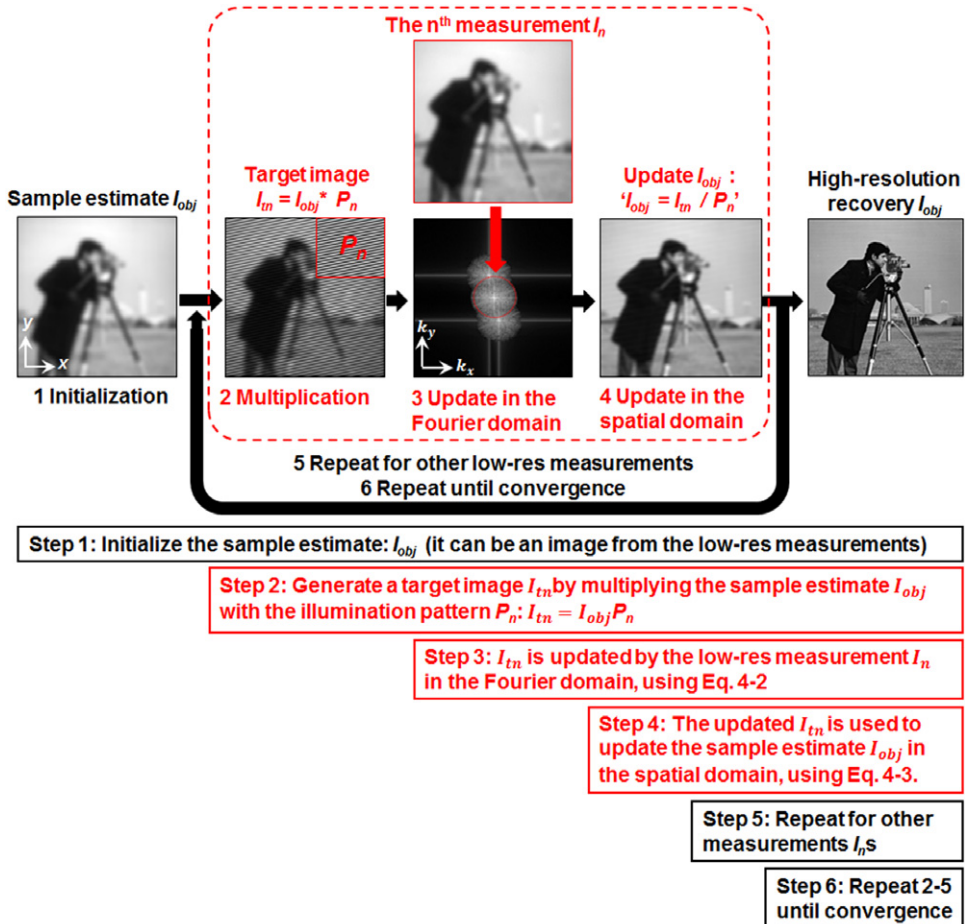


Figure 4.2. The recovery procedures of the pattern-illuminated FP scheme. Adapted from [1]

The term $\mathcal{F}(I_{tn})^{\text{updated}}$ is then transformed back to the spatial domain to produce an updated target image I_{tn}^{updated} .

Step 4: the updated target image I_{tn}^{updated} is used to update the high-resolution sample estimate in the spatial domain using the following equation:

$$I_{obj}^{\text{updated}} = I_{obj} + \frac{P_n}{(\max(P_n))^2} \cdot (I_{tn}^{\text{updated}} - I_{obj} \cdot P_n) \quad (4.3)$$

Step 5: The updating process is repeated for all different illumination patterns.

Step 6: Steps 2–5 are repeated until the solution converges. The convergence metric can be the mean-square-error (MSE) of two consecutive recovered solutions. We can terminate the process if the MSE is smaller than a pre-defined value. In a practical implementation, we can simply terminate it with a pre-defined loop number, typically 10–100.

We use the following MATLAB code to simulate the recovery process of the pattern-illuminated FP scheme. In lines 1–3, we simulate the high-resolution object using the ‘cameraman’ image. In lines 4–19, we set up the incoherent imaging system and define the incoherent transfer function. In lines 20–37, we generate a sequence of speckle patterns ‘patternSeq’ for sample illumination. In particular, we create one speckle pattern in line 21 and shift this pattern to produce a sequence of speckle patterns in line 36.

```

1  %% input high-resolution image
2  objectIntensity = double(imread('cameraman.tif'));
3  figure;imshow(abs(objectIntensity),[]);
4  %% set up the incoherent imaging system
5  waveLength = 0.63e-6;
6  psize = 0.5e-6; % sampling pixel size
7  NA = 0.15;
8  k0 = 2*pi/waveLength;
9  cutoffFrequency = NA*k0;
10 [m n] = size(objectIntensity);
11 kx = -pi/psize:2*pi/(psize*(n-1)):pi/psize;
12 ky = -pi/psize:2*pi/(psize*(n-1)):pi/psize;
13 [kxm kym] = meshgrid(kx,ky);
14 CTF = double(((kxm.^2+kym.^2)<cutoffFrequency^2)); % define the coherent
   transfer function
15 cpsf = fftshift(ifft2(ifftshift(CTF))); % coherent PSF
16 ipsf = (abs(cpsf)).^2; % incoherent PSF
17 OTF = abs(fftshift(fft2(fftshift(ipsf)))); % incoherent transfer function
18 OTF = OTF./max(max(OTF));
19 figure;imshow(abs(OTF),[]); title('Incoherent OTF in the Fourier domain');
20 %% define illumination pattern
21 pattern = imnoise(ones(m,n), 'speckle', 0.5);
22 patternNum = 49; % number of speckle patterns
23 % define the scanning path of the speckle pattern
24 arraySize = 15;
25 xLocation = zeros(1,arraySize^2);
26 yLocation = zeros(1,arraySize^2);
27 scanStep = 2;
28 for i=1:arraySize
29     xLocation(1,1+arraySize*(i-1):15+arraySize*(i-1))
30         = (- (arraySize-1)/2:1:(arraySize-1)/2)*scanStep;
31     yLocation(1,1+arraySize*(i-1):15+arraySize*(i-1))
32         = ((arraySize-1)/2-(i-1))*scanStep;
33 end;
34 snakeSeq = gseq(arraySize);
35 patternSeq = zeros(m,n,patternNum);
36 % shift one speckle pattern to generate a sequence of speckle patterns
37 for i=1:patternNum
38     patternSeq(:,:,:,i)
39         = circshift(pattern,[xLocation(snakeSeq(i)) yLocation(snakeSeq(i))]);
40 end

```

In lines 38–43, we create a sequence of low-resolution measurements ‘imSeqLowRes’ using the forward imaging model. In lines 44–64, we use the pattern-illuminated FP procedures to recover the high-resolution sample image. In line 56, we update the sample estimate in the Fourier domain using equation (4.2). In line 58, we update the sample estimate in the spatial domain using equation (4.3). The updating process is repeated for different measurements

(line 48) and the entire process is repeated several times for solution convergence (line 47).

```

38 %% forward imaging model
39 imSeqLowRes = zeros(m,n,patternNum);
40 for i=1:patternNum
41     lowResFT = OTF.*fftshift(fft2(objectIntensity.*patternSeq(:,:,i)));
42     imSeqLowRes(:,:,:,i) = abs(ifft2(ifftshift(lowResFT)));
43 end
44 %% pattern-illuminated FP recovery
45 objectRecover = sum(imSeqLowRes,3)/patternNum; % initial guess
46 figure;imshow(objectRecover,[]);title('diffraction-limited image');
47 for loopnum=1:10
48     for i=1:patternNum
49         object_pattern=objectRecover.*patternSeq(:,:,i);
50         object_pattern2=object_pattern;
51         object_patternFT=fftshift(fft2(object_pattern));
52         lowResFT1=OTF.*object_patternFT;
53         im_lowRes=ifft2(ifftshift(lowResFT1));
54         im_lowRes=imSeqLowRes(:,:,:,i).*exp(li.*angle(im_lowRes));
55         lowResFT2=fftshift(fft2(im_lowRes));
56         object_patternFT=object_patternFT
57             + conj(OTF)./(max(max((abs(OTF)).^2))).*(lowResFT2-lowResFT1);
58         object_pattern=ifft2(ifftshift(object_patternFT));
59         objectRecover=objectRecover + patternSeq(:,:,:,i)
60             .* (object_pattern-object_pattern2)./(max(max(patternSeq(:,:,:,i))).^2);
61     end;
62     figure;imshow(abs(objectRecover),[]);
63     title('Pattern-illuminated FP recovery');
64     objectRecoverFT=fftshift(fft2(objectRecover));
65     figure;imshow(log(abs(objectRecoverFT)),[]);

```

In coherent FP settings, we can jointly recover the unknown aberrations and the high-resolution sample image in the iterative process [15]. We can modify this process to jointly recover the unknown illumination pattern and the super-resolution sample image in the patterned-illuminated FP scheme [1, 4, 5]. In this case, one unknown pattern can be translated to different spatial positions or rotated with different orientations. At each position, one low-resolution image is acquired using the low-NA objective lens. Similar to the recovering process of the sample image I_{obj} , we can assign an initial guess for the unknown pattern P_{unknown} . To recover this unknown pattern, we only need to add one more step in the image updating process:

$$P_{\text{unknown}}^{\text{updated}} = P_{\text{unknown}} + \frac{I_{\text{obj}}}{\left(\max(I_{\text{obj}})\right)^2} \cdot (I_{tn}^{\text{updated}} - I_{\text{obj}} \cdot P_{\text{unknown}}(x - x_n)), \quad (4.4)$$

where the updated target image I_{tn}^{updated} is used to update the unknown pattern and x_n represents the scanning positions of the pattern. We can add the following MATLAB code to recover the unknown pattern in the iterative process:

```

1 patternRecover = patternRecover + objectRecover./
    (max(max((abs(objectRecover)).^2))).*(object_pattern-object_pattern2);

```

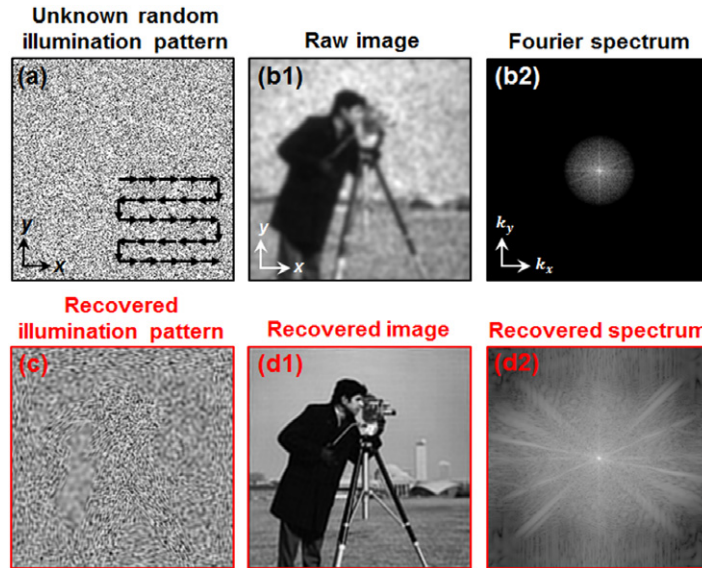


Figure 4.3. Simulation of the pattern-illuminated FP recovery scheme. (a) The unknown illumination pattern is translated into 169 different spatial positions. (b1) The simulated raw image. (b2) The Fourier spectrum of (b1). (c) The recovered illumination pattern. (d) The recovered high-resolution object image and its Fourier spectrum. We use 15 loops in the reconstruction process. Adapted from [1].

Figure 4.3 shows the simulation result using the pattern-illuminated FP scheme. In this simulation, we translate one unknown speckle pattern to 169 different spatial positions and use them for sample illumination. We show one low-resolution raw image in figure 4.3(b). The recovered unknown illumination pattern and the recovered high-resolution object image are shown in figure 4.3(c) and (d).

The pattern-illuminated FP scheme can be used to improve the resolution of a conventional fluorescence microscope platform. Figure 4.4 shows the result of super-resolution fluorescence imaging using the pattern-illuminated FP scheme. The experiment was performed on a Nikon Ti fluorescence microscope with a 10 \times , 0.25 NA objective lens. As shown in figure 4.4(a), a 488 nm laser diode was used as the light source and a diffuser was inserted into the epi-illumination reflector cube. The excitation light thus produced an unknown speckle pattern on the sample. Figure 4.4(b) shows one raw image of a mouse kidney sample and the speckle-like pattern is evident in this raw image. To perform pattern-illuminated FP imaging, we moved the sample to different spatial positions using a motorized stage and acquired the corresponding images under the speckle-pattern illumination. Figure 4.4(d) shows the FP reconstruction using 49 raw images. Figure 4.4(c) shows the

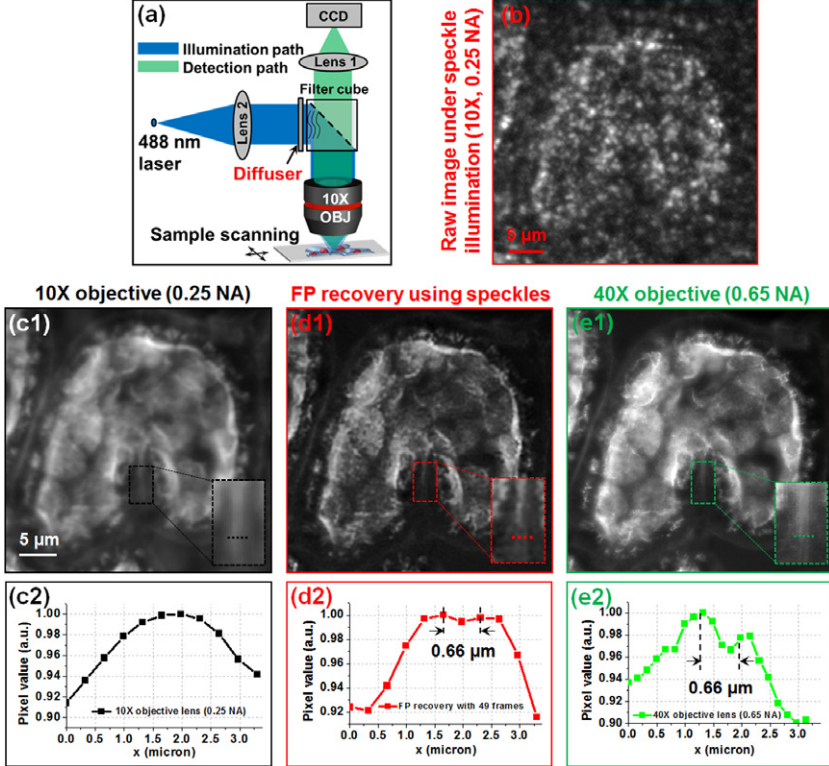


Figure 4.4. Super-resolution fluorescence imaging using the pattern-illuminated FP scheme. (a) The experimental setup. (b) One raw image under the speckle-pattern illumination. (c) The uniform-illuminated image using the same 10 \times objective. (d) The recovered image using the pattern-illuminated FP scheme. (e) The high-resolution ground truth using the 40 \times objective. Adapted from [1].

uniform-illuminated sample image using the same 10 \times objective lens. As a comparison, figure 4.4(e) shows the uniform-illuminated image using a 40 \times high-NA objective. Figure 4.4(c2)–(e2) shows the intensity line traces of a small feature of the sample, corresponding to the highlighted regions in figure 4.4(c1)–(e1). As shown in figure 4.4(c2), we cannot resolve the two lines using the 10 \times objective lens. We can, however, barely resolve the two-line feature using the recovered FP image in figure 4.4(d2). We can also observe the same feature from the image captured by the 40 \times objective in figure 4.4(e2).

4.2 Resolution doubling using 4 frames

Improving the lateral resolution beyond the diffraction limit remains an important challenge in optical imaging. Conventional structured illumination microscopy (SIM) employs sinusoidal patterns for sample illumination [6, 7, 16].

Frequency mixing between the sample and the sinusoidal patterns modulates the high-frequency components to the passband of the collection optics. In a typical implementation of SIM, three different lateral phase shifts ($0, 2\pi/3, 4\pi/3$) are needed for each orientation of the sinusoidal pattern and three different orientations are needed to double the bandwidth isotropically in the Fourier domain. Therefore, nine incoherent images are needed in the acquisition process of SIM. The capability of bypassing the diffraction limit has made SIM a popular tool for microscopy imaging with high-spatiotemporal resolution and reduced phototoxicity.

We can apply the pattern-illuminated FP scheme to the SIM data and reduce the number of image acquisitions from 9 to 4 [3]. Figure 4.5 shows the four sinusoidal patterns used in the pattern-illuminated FP scheme for sample illumination. The first two sinusoidal patterns have the same orientation but are π -shifted. The last two patterns are oriented at two other directions. The recovery process begins with an initial guess of the high-resolution sample image: $I_{\text{obj}} = I_1 + I_2$. This initial guess is then multiplied with a sinusoidal pattern P_n to generate a target image in the spatial domain: $I_{tn} = I_{\text{obj}} \cdot P_n$. The target image I_{tn} is then updated by the measurement I_n using the following equation:

$$I_{tn}^{\text{updated}} = I_{tn} + \text{deconvwnr}(I_n - \text{PSF} \cdot I_{tn}), \quad (4.5)$$

where ‘deconvwnr’ stands for Wiener deconvolution. The use of deconvolution here is to better capture the noise characteristics and improve the convergence performance. The updated target image in equation (4.5) is then used to update the initial guess using equation (4.3). The updating process is repeated for the four measurements and the entire process is terminated until solution convergence. We use the following MATLAB code to simulate the 4-frame resolution-doubling process. In lines 1–15, we define the four sinusoidal patterns for sample illumination. In lines 16–21, we create the four low-resolution measurements using the forward imaging model (one can define the incoherent imaging system using the same code in section 4.1). In lines 22–39, we perform 4-frame resolution doubling in an iterative manner. In particular, we update the target image using equation (4.5) in line 34. In line 35, we update the sample estimate using equation (4.3). The updating process is

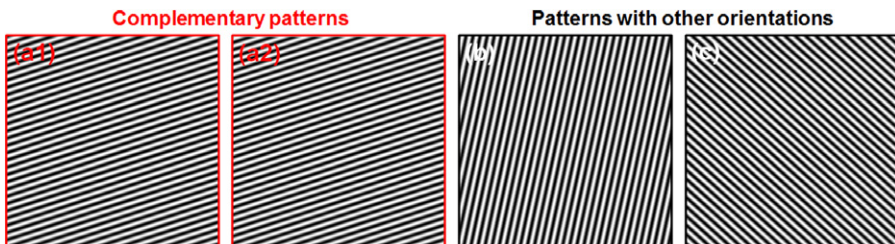


Figure 4.5. The 4 illumination patterns for resolution doubling in the pattern-illuminated FP scheme. (a1)–(a2) Two complementary patterns (with 0 and π shifts) for uniform sample modulation. (b)–(c) Patterns with two other orientations for expanding the bandwidth along two other directions. Adapted from [3].

repeated for different measurements (line 28) and the entire process is repeated for solution convergence (line 27).

```

1  %% define the illumination patterns
2  NA_ill=0.14; % illumination NA for the sin patterns
3  sita=(0:2*pi/3:2*pi/3);% three orientations
4  n=size(objectIntensity,1);
5  for i=1:3
6      kx_relative(i) = NA_ill.*sin(sita(i));
7      ky_relative(i) = NA_ill.*cos(sita(i)); % create kx, ky wavevectors
8      kx = k0*kx_relative(i);
9      ky = k0*ky_relative(i);
10     x = -n/2*psize:psize:(n/2-1)*psize;
11     y = -n/2*psize:psize:(n/2-1)*psize;
12     [X, Y]=meshgrid(x,y);
13     patternSeq(:,:,i)=(1.1+1.*sin(kx.*X+ky.*Y));
14 end
15 patternSeq(:,:4) = 2.2-patternSeq(:,:,1);% the complementary pattern
16 %% forward imaging model
17 imSeqLowRes = zeros(m,n,4);
18 for i=1:4
19     lowResFT = OTF.*fftshift(fft2(objectIntensity.*patternSeq(:,:,i)));
20     imSeqLowRes(:,:,:,i) = abs(ifft2(ifftshift(lowResFT)));
21 end
22 %% pattern-illuminated FP recovery
23 objectRecover = imSeqLowRes(:,:,1)+ imSeqLowRes(:,:,4); % initial guess
24 figure;imshow(objectRecover,[]);
25 title('diffraction-limited image');
26 objectRecoverFT = fftshift(fft2(objectRecover));
27 for loop=1:50
28     for i=1:4
29         object_pattern = objectRecover.*patternSeq(:,:,i);
30         object_pattern2 = object_pattern;
31         object_patternFT = fftshift(fft2(object_pattern));
32         lowResFT = OTF.*object_patternFT;
33         im_lowRes = ifft2(ifftshift(lowResFT));
34         object_pattern = object_pattern
35             + deconvwnr(imSeqLowRes(:,:,i)-im_lowRes,ipsf,0.01);
36         objectRecover = objectRecover + (patternSeq(:,:,i))
37             .* (object_pattern-object_pattern2)./((max(max(patternSeq(:,:,i)))).^2);
38     end;
39 end;
40 figure;imshow(abs(objectRecover),[]);
41 title('Recovered high resolution image');

```

Figure 4.6 demonstrates the simulation result of the 4-frame resolution-doubling process. Figure 4.6(a) shows the diffraction-limited image and its Fourier spectrum. Figure 4.6(b1) shows the results using the conventional 9-frame SIM scheme. Figure 4.6(b2) shows the results using the 4-frame resolution-doubling scheme. In this simulation, we use both the mean square error (MSE) and structural similarity (SSIM) index to quantify the imaging performance. We can see that, the performance of the 4-frame FP scheme is similar to that of the conventional 9-frame SIM.

We have also performed an experiment to validate the 4-frame resolution-doubling FP scheme. Figure 4.7(a) shows the imaging setup, where we used a projector to generate the sinusoidal patterns. Figure 4.7(b) shows the diffraction-limited images under uniform illumination. Figure 4.7(c) shows the deconvolved images of figure 4.7(b). Figure 4.7(d) shows the recovered super-resolution images using the 4-frame FP scheme. The use of 4-frame resolution-doubling scheme may

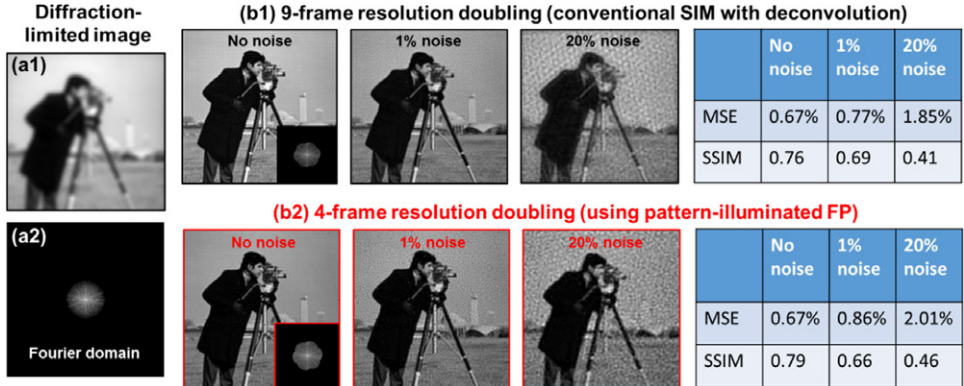


Figure 4.6. 4-frame resolution doubling using the pattern-illuminated FP scheme (simulation). (a) The diffraction-limited image and its Fourier spectrum. Comparison between the typical 9-frame SIM implementation (b1) and the 4-frame FP recovery scheme (b2). Adapted from [3].

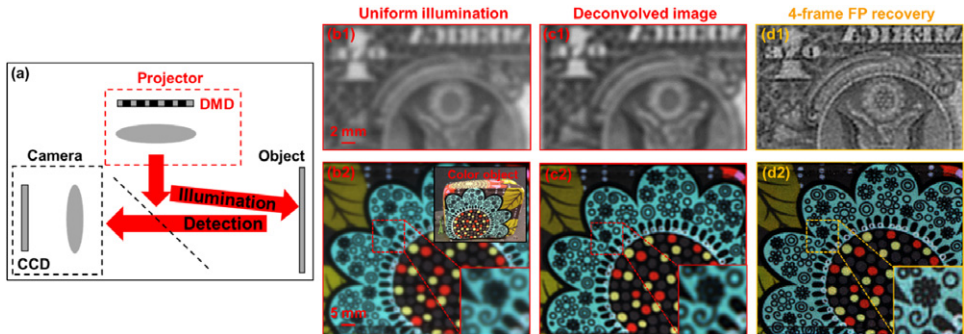


Figure 4.7. 4-frame resolution doubling using the pattern-illuminated FP scheme (experiment). (a) The experimental setup. (b) Diffraction-limited images of two different samples. (c) Deconvolved images of (b). (d) The resolution-doubled images using the 4-frame FP scheme. Adapted from [3].

shorten the acquisition time of SIM experiments and reduce phototoxicity for biological samples.

4.3 Recovering higher dimensional data

The multiplexing idea from the ptychography community [17, 18] can also be applied to the incoherent FP imaging setting. In this case, we project non-uniform intensity patterns onto the sample and capture the corresponding 2D intensity images. These captured images represent a mixture of higher dimensional information, such as data at different z -sections or data at the different spectral bands. In the reconstruction process, we can use the multi-state FP algorithm (section 2.6) to improve the spatial resolution and to recover the lost higher dimensional data at the same time, as shown in figure 4.8. We term this scheme multiplexed structured illumination or multiplexed-SI [4].

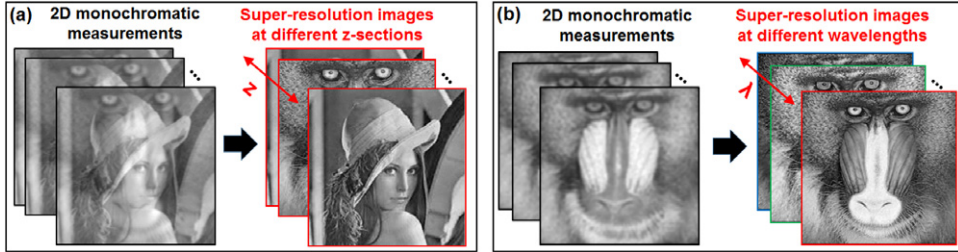


Figure 4.8. The multiplexed structured illumination framework using multi-state FP modeling. (a) Images corresponding to different illumination patterns are used to recover super-resolution images at different z sections (a) and super-resolution images at different wavelengths (b). Adapted from [4].

The forward imaging model of the multiplexed structured illumination scheme can be described as follows:

$$\mathcal{F}(I_n) = \sum_m \text{OTF}_m \cdot \mathcal{F}(I_{\text{obj},m} \cdot P_{mn}), \quad (4.6)$$

where \mathcal{F} stands for Fourier transform, I_n stands for 2D image measurements, OTF_m stands for the incoherent optical transfer function of the objective lens, $I_{\text{obj},m}$ stands for the ground-truth image of the sample, and P_{mn} stands for the illumination pattern. In equation (4.6), the summation over subscript ‘ m ’ stands for the mixture of higher dimensional data. For example, we can model the captured images I_n as a summation of red, green, blue channels with $m = 1, m = 2$, and $m = 3$. For each mode ‘ m ’, we have ‘ n ’ different intensity patterns for sample illumination, and thus, we have two subscripts for ‘ P_{mn} ’. In our implementation, we will translate the unknown illumination pattern to ‘ n ’ different spatial positions to get the corresponding 2D image measurements. As a result, we have ‘ m ’ unknown illumination patterns. The goal here is to recover different modes of the object $I_{\text{obj},m}$ and the unknown illumination patterns P_{mn} ($m = 1, 2, \dots$) from the 2D image measurements I_n . If $m = 1$, equation (4.6) reduces to the forward imaging model of the pattern-illuminated FP scheme discussed in section 4.1.

The recovery process of the multiplexed structured illumination framework starts with the initial guess of different object modes $I_{\text{obj},m}$ and the unknown illumination pattern P_{mn} ($m = 1, 2, \dots$). We then define I_{pm} and I_{tm} as follows:

$$I_{pm} = I_{\text{obj},m} \cdot P_{mn} \quad (4.7)$$

$$\mathcal{F}(I_{tm}) = \text{OTF}_m \cdot \mathcal{F}(I_{pm}) \quad (4.8)$$

Based on the initial guess and the measurement I_n , we have the following updating procedures for each incoherent mode:

$$I_{tm}^{\text{updated}} = \frac{I_{tm} \cdot I_n}{\sum_m I_{tm}} \quad (4.9)$$

$$\mathcal{F}(I_{pm}^{\text{updated}}) = \mathcal{F}(I_{pm}) + \text{OTF}_m \cdot (\mathcal{F}(I_{tm}^{\text{updated}}) - \mathcal{F}(I_{tm})) \quad (4.10)$$

$$I_{\text{obj_}m}^{\text{updated}} = I_{\text{obj_}m} + \frac{P_{mn}}{(\max(P_{mn}))^2} \cdot (I_{pm}^{\text{updated}} - I_{pm}) \quad (4.11)$$

$$P_{mn}^{\text{updated}} = P_{mn} + \frac{I_{\text{obj_}m}^{\text{updated}}}{\left(\max(I_{\text{obj_}m}^{\text{updated}})\right)^2} \cdot (I_{pm}^{\text{updated}} - I_{pm}) \quad (4.12)$$

Depending on the total number of modes m , equations (4.7)–(4.12) represent $6m$ equations. The updating process will be repeated for all n measurements corresponding to different illumination patterns and the entire process will be repeated until the solution converges. In a practical implementation, we can simply terminate it with a predefined loop number, typically 10–150.

The following MATLAB code simulates the multiplexed structure illumination framework discussed above. In lines 1–6, we simulate the input high-resolution color object at red, green and blue channels (the color baboon image). In lines 7–37, we set up the incoherent transfer functions for three channels. In lines 38–61, we generate three sets of speckle patterns for sample illumination. In lines 62–75, we use the forward imaging model to simulate the captured low-resolution monochromatic images ‘imSeqLowRes_t’.

```

1 %% input high-resolution color image
2 imsize=256;
3 imtemp=double(imread('baboon.jpg'));
4 objectIntensity_r = imresize(imtemp(:,:,1),[imsize imsize]);
5 objectIntensity_g = imresize(imtemp(:,:,2),[imsize imsize]);
6 objectIntensity_b = imresize(imtemp(:,:,3),[imsize imsize]);
7 %% setup the incoherent imaging system
8 wavelength_r = 0.63e-6;
9 wavelength_g = 0.53e-6;
10 wavelength_b = 0.47e-6;
11 psize = 0.5e-6; % sampling pixel size
12 NA = 0.15;
13 k0_r = 2*pi/wavelength_r;
14 k0_g = 2*pi/wavelength_g;
15 k0_b = 2*pi/wavelength_b;
16 cutoffFrequency_r = NA * k0_r;
17 cutoffFrequency_g = NA * k0_g;
18 cutoffFrequency_b = NA * k0_b;
19 [m n] = size(objectIntensity_r);
20 kx = -pi/psize:2*pi/(psize*(n-1)):pi/psize;
21 ky = -pi/psize:2*pi/(psize*(n-1)):pi/psize;
22 [kxm kym] = meshgrid(kx,ky);
23 CTF_r = double(((kxm.^2+kym.^2)<cutoffFrequency_r^2));
24 CTF_g = double(((kxm.^2+kym.^2)<cutoffFrequency_g^2));
25 CTF_b = double(((kxm.^2+kym.^2)<cutoffFrequency_b^2));
26 cpsf_r = fftshift(ifft2(ifftshift(CTF_r))); % coherent PSF
27 cpsf_g = fftshift(ifft2(ifftshift(CTF_g)));
28 cpsf_b = fftshift(ifft2(ifftshift(CTF_b)));

```

```

29 ipsf_r = (abs(cpsf_r)).^2; % incoherent PSF
30 ipsf_g = (abs(cpsf_g)).^2;
31 ipsf_b = (abs(cpsf_b)).^2;
32 OTF_r = abs(fftshift(fft2(ifftshift(ipsf_r)))); % incoherent OTF
33 OTF_r = OTF_r./max(max(OTF_r));
34 OTF_g = abs(fftshift(fft2(ifftshift(ipsf_g)))); % incoherent OTF
35 OTF_g = OTF_g./max(max(OTF_g));
36 OTF_b = abs(fftshift(fft2(ifftshift(ipsf_b)))); % incoherent OTF
37 OTF_b = OTF_b./max(max(OTF_b));
38 %% define illumination pattern
39 pattern_r = imnoise(ones(m,n),'speckle',0.5);
40 pattern_g = imnoise(ones(m,n),'speckle',0.5);
41 pattern_b = imnoise(ones(m,n),'speckle',0.5);
42 patternNum = 169; % number of speckle patterns
43 % define the scanning path of the speckle pattern
44 arraySize = 15;
45 xLocation = zeros(1,arraySize^2);
46 yLocation = zeros(1,arraySize^2);
47 scanStep = 2;
48 for i=1:arraySize
49     xLocation(1,1+arraySize*(i-1):15+arraySize*(i-1))
50         = (- (arraySize-1)/2:1:(arraySize-1)/2)*scanStep;
51     yLocation(1,1+arraySize*(i-1):15+arraySize*(i-1))
52         = ((arraySize-1)/2-(i-1))*scanStep;
53 end;
54 snakeSeq = gseq(arraySize);
55 patternSeq_r = zeros(m,n,patternNum);
56 patternSeq_g = zeros(m,n,patternNum);
57 patternSeq_b = zeros(m,n,patternNum);

58 % shift one speckle pattern to generate a sequence speckle patterns
59 for i=1:patternNum
60     patternSeq_r(:,:,i) =
61         circshift(pattern_r,[xLocation(snakeSeq(i)) yLocation(snakeSeq(i))]);
62     patternSeq_g(:,:,i) =
63         circshift(pattern_g,[xLocation(snakeSeq(i)) yLocation(snakeSeq(i))]);
64     patternSeq_b(:,:,i) =
65         circshift(pattern_b,[xLocation(snakeSeq(i)) yLocation(snakeSeq(i))]);
66 end
67 %% forward imaging model
68 imSeqLowRes_r = zeros(m,n,patternNum);
69 imSeqLowRes_g = zeros(m,n,patternNum);
70 imSeqLowRes_b = zeros(m,n,patternNum);
71 imSeqLowRes_t = zeros(m,n,patternNum);
72 for i=1:patternNum
73     lowResFT_r = OTF_r
74         .*fftshift(fft2(objectIntensity_r.*patternSeq_r(:,:,i)));
75     imSeqLowRes_r(:,:,i) = abs(ifft2(ifftshift(lowResFT_r)));
76     lowResFT_g = OTF_g
77         .*fftshift(fft2(objectIntensity_g.*patternSeq_g(:,:,i)));
78     imSeqLowRes_g(:,:,i) = abs(ifft2(ifftshift(lowResFT_g)));
79     lowResFT_b = OTF_b
80         .*fftshift(fft2(objectIntensity_b.*patternSeq_b(:,:,i)));
81     imSeqLowRes_b(:,:,i) = abs(ifft2(ifftshift(lowResFT_b)));
82     imSeqLowRes_t(:,:,i) = imSeqLowRes_r(:,:,i)
83         + imSeqLowRes_g(:,:,i) + imSeqLowRes_b(:,:,i);
84 end

```

In lines 76–120, we use the multiplexed structured illumination scheme to recover the high-resolution images at three channels. In particular, we generate

the initial guess in lines 77–79. Lines 98–100 correspond to equation (4.9). Lines 104–106 correspond to equation (4.10). Lines 110–112 correspond to equation (4.11). In this simulation example, we assume the illumination patterns are known. If they are unknown, one can also recover the patterns using equation (4.12).

```

76  %% multiplexed structured illumination recovering scheme
77  objectRecover_r = sum(imSeqLowRes_t,3)/(3*patternNum); % initial guess
78  objectRecover_g = sum(imSeqLowRes_t,3)/(3*patternNum);
79  objectRecover_b = sum(imSeqLowRes_t,3)/(3*patternNum);
80  for loopnum=1:5
81      for i=1:patternNum
82          object_pattern_r=objectRecover_r.*patternSeq_r(:,:,i);
83          object_pattern_g=objectRecover_g.*patternSeq_g(:,:,i);
84          object_pattern_b=objectRecover_b.*patternSeq_b(:,:,i);
85          object_pattern2_r=object_pattern_r;
86          object_pattern2_g=object_pattern_g;
87          object_pattern2_b=object_pattern_b;
88          object_patternFT_r=fftshift(fft2(object_pattern_r));
89          object_patternFT_g=fftshift(fft2(object_pattern_g));
90          object_patternFT_b=fftshift(fft2(object_pattern_b));
91          lowResFT1_r=OTF_r.*object_patternFT_r;
92          lowResFT1_g=OTF_r.*object_patternFT_g;
93          lowResFT1_b=OTF_r.*object_patternFT_b;
94          im_lowRes_r=ifft2(ifftshift(lowResFT1_r));
95          im_lowRes_g=ifft2(ifftshift(lowResFT1_g));
96          im_lowRes_b=ifft2(ifftshift(lowResFT1_b));
97          intensity = im_lowRes_r + im_lowRes_g + im_lowRes_b;
98          im_lowRes_r=imSeqLowRes_t(:,:,i).*im_lowRes_r
99              .//intensity.*exp(li.*angle(im_lowRes_r));
100         im_lowRes_g=imSeqLowRes_t(:,:,i).*im_lowRes_g
101             .//intensity.*exp(li.*angle(im_lowRes_g));
102         im_lowRes_b=imSeqLowRes_t(:,:,i).*im_lowRes_b
103             .//intensity.*exp(li.*angle(im_lowRes_b));
104         lowResFT2_r=fftshift(fft2(im_lowRes_r));
105         lowResFT2_g=fftshift(fft2(im_lowRes_g));
106         lowResFT2_b=fftshift(fft2(im_lowRes_b));
107         object_patternFT_r=object_patternFT_r
108             + (OTF_r)./(max(max((abs(OTF_r)).^2))).*(lowResFT2_r-lowResFT1_r);
109         object_patternFT_g=object_patternFT_g
110             + (OTF_g)./(max(max((abs(OTF_g)).^2))).*(lowResFT2_g-lowResFT1_g);
111         object_patternFT_b = object_patternFT_b
112             + (OTF_b)./(max(max((abs(OTF_b)).^2))).*(lowResFT2_b-lowResFT1_b);
113         object_pattern_r = ifft2(ifftshift(object_patternFT_r));
114         object_pattern_g = ifft2(ifftshift(object_patternFT_g));
115         object_pattern_b = ifft2(ifftshift(object_patternFT_b));
116         objectRecover_r = objectRecover_r + patternSeq_r(:,:,i)
117             .* (object_pattern_r - object_pattern2_r)
118                 ./ (max(max(patternSeq_r(:,:,i)))).^2;
119         objectRecover_g = objectRecover_g + patternSeq_g(:,:,i)
120             .* (object_pattern_g - object_pattern2_g)
121                 ./ (max(max(patternSeq_g(:,:,i)))).^2;
122         objectRecover_b=objectRecover_b + patternSeq_b(:,:,i)
123             .* (object_pattern_b - object_pattern2_b)
124                 ./ (max(max(patternSeq_b(:,:,i)))).^2;
125     end
126 end;
127 figure;imshow(abs(objectRecover_r),[]);
128 title('Multiplexed-SI recovery (red)');
129 figure;imshow(abs(objectRecover_g),[]);
130 title('Multiplexed-SI recovery (green)');
131 figure;imshow(abs(objectRecover_b),[]);
132 title('Multiplexed-SI recovery (blue)');

```

Figure 4.9 demonstrates the simulation result of the recovery procedures above. In this example, we assume the object contains three different color channels (red, green, and blue), and the captured images represent a mixture of these three channels, as described by equation (4.6). Figure 4.9(a) shows the raw image under speckle illumination and its Fourier spectrum. We have added 1% noise in the raw images in this simulation. For the monochromatic raw image shown in figure 4.9(a), we cannot see any spectral information of the sample. We then translated the speckle patterns to 220 different positions and generated the corresponding mixtures. The ground truth of the three color channels and the color combination are shown in figure 4.9(b1)–(b4). The recovered objects and speckles using the multiplexed structured illumination scheme are shown in figure 4.9(c) and (d). The Fourier spectrums are also shown in the inset of figure 4.9(c).

Figure 4.10 shows the experimental result of the multiplexed structured illumination scheme. In this experiment, we used a video projector (figure 4.10(a)) to project an unknown color speckle pattern on a color sample. We then translated the unknown pattern to 114 positions and captured the corresponding images using a monochromatic CCD camera. Figure 4.10(b) shows a low-resolution monochromatic measurement of the color object. Figures 4.10(c1)–(c3) show the diffraction-limited images under uniform red/green/blue illuminations. Figures 4.10(d1)–(d3) show the recovered images (at red/green/blue channels) using the multiplexed structured illumination scheme. Figures 4.10(e1)–(e3) show the recovered speckles at red/green/blue channels. As a comparison, the ground-truth image of the sample is shown in figure 4.10(f) and the corresponding line traces are shown in figure 4.10(g). From this experiment, we can see that the multiplexed structured illumination scheme is able to recover the sample's spectral information and improve the spatial resolution at the same time.

The multiplexed structured illumination scheme can also be used to recover different z -sections of a 3D sample. In this case, the captured images represent incoherent mixtures of different sections along the optical axis. In figure 4.11, we used two pathology sections as the object and put this two-layer object close to a diffuser. The transmitted light from the diffuser formed an unknown speckle pattern on the two-layer object. We then translated the object to 224 different positions and captured the corresponding images using a microscope system, as shown in figure 4.11(a). Figure 4.11(b) shows one captured raw image of the two-layer object. Figure 4.11(c) shows the diffraction-limited images under uniform illumination. In particular, we took the images of the two sections individually in figures 4.11(c1) and (c2). Figure 4.11(d) shows the recovered images using the multiplexed structured illumination scheme. As a comparison, the ground-truth images of the two sections are shown in figure 4.11(e) and the corresponding line traces are shown in figure 4.11(f). Finally, we note that, we did not model the interaction between different modes in the multiplexed structured illumination framework. In other words, we assume different modes are independent of each other. This assumption is valid for information at different spectral bands. For information at different z sections, this assumption is only valid for transparent sample, where emission from one section is independent of

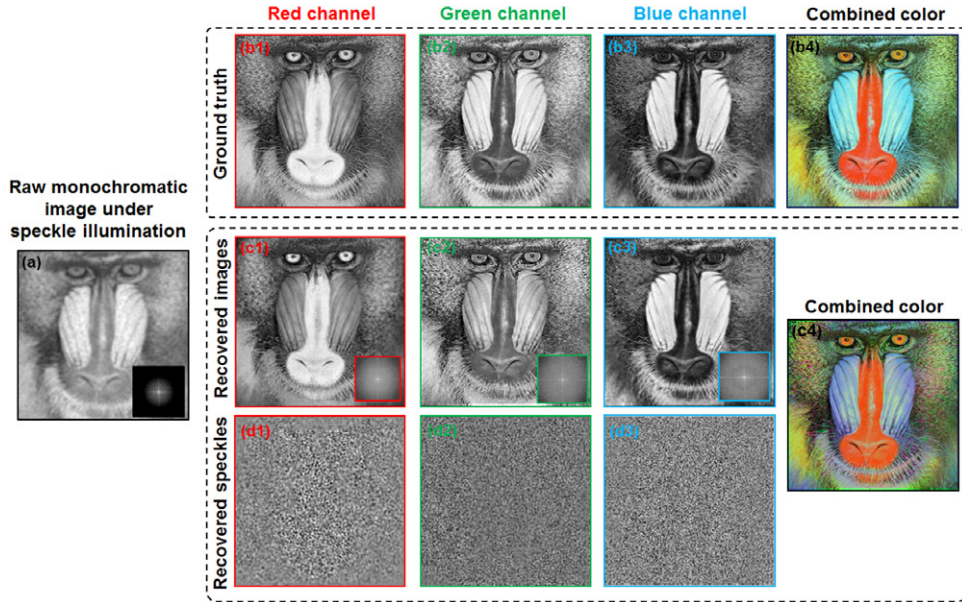


Figure 4.9. Recovery of different spectral bands using the multiplexed structured illumination scheme (simulation). (a) The low-resolution acquisition under unknown speckle illumination. Insets show the corresponding Fourier spectrum. (b) The input ground truth. (c) The recovered images using the multiplexed structured illumination scheme. (d) The recovered speckles at three different spectral bands. Adapted from [4].

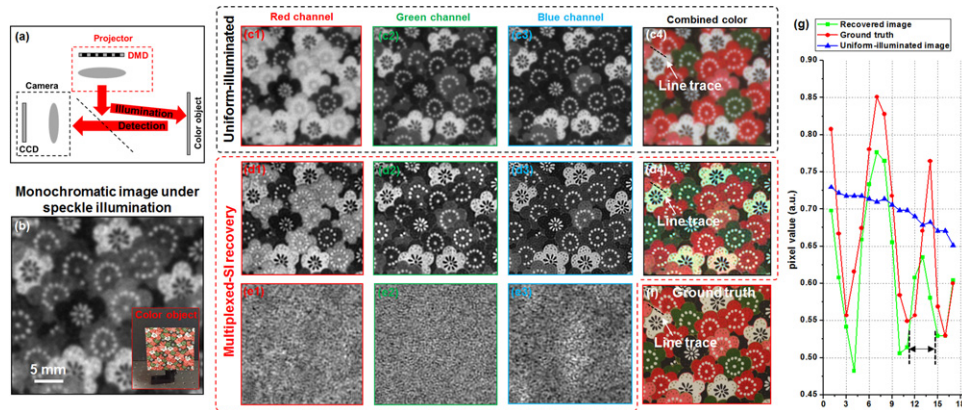


Figure 4.10. Recovery of different spectral bands using the multiplexed structured illumination scheme (experiment). (a) The experimental setup. A video projector was used to project translated unknown color speckles on the sample. (b) The raw monochromatric measurement of the color object. (c) The diffraction-limited images under uniform illuminations. The recovered sample images (d) and speckle patterns (e) using the multiplexed structure illumination scheme. (f) The ground truth of the object. (g) Lines traces of (c4), (d4), and (f). Adapted from [4].

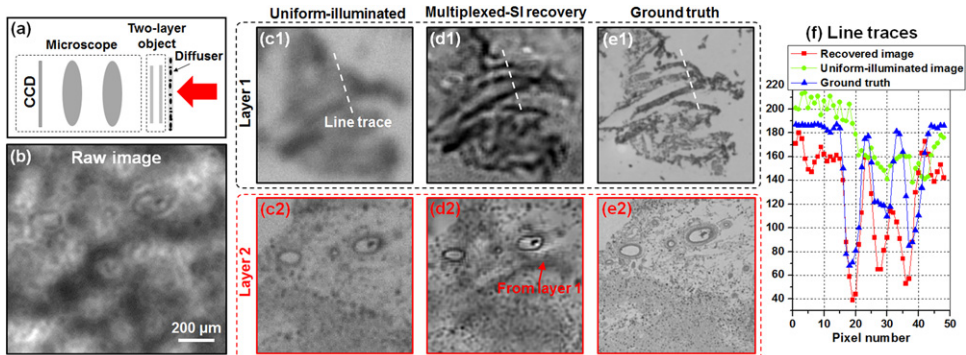


Figure 4.11. Recovery of different z sections using the multiplexed structured illumination scheme (experiment). (a) The imaging setup. (b) One raw measurement, representing an incoherent mixture of the two sections. (c) The diffraction-limited images under uniform illumination. (d) The recovered images using the multiplexed structured illumination scheme. (e) The ground-truth images of the two sections. (f) Line traces of a small feature in (c1)–(e1). Adapted from [4].

other sections. One future direction of the multiplexed structured illumination scheme is to model the interaction between different incoherent modes. If successful, we can use it to model a diffused sample and perform deep-tissue imaging.

Bibliography

- [1] Dong S, Nanda P, Shiradkar R, Guo K and Zheng G 2014 High-resolution fluorescence imaging via pattern-illuminated Fourier ptychography *Opt. Exp.* **22** 20856–70
- [2] Chakrova N, Heintzmann R, Rieger B and Stallinga S 2015 Studying different illumination patterns for resolution improvement in fluorescence microscopy *Opt. Exp.* **23** 31367–83
- [3] Dong S, Liao J, Guo K, Bian L, Suo J and Zheng G 2015 Resolution doubling with a reduced number of image acquisitions *Biomed. Opt. Exp.* **6** 2946–52
- [4] Dong S, Guo K, Jiang S and Zheng G 2015 Recovering higher dimensional image data using multiplexed structured illumination *Opt. Exp.* **23** 30393–8
- [5] Dong S, Nanda P, Guo K, Liao J and Zheng G 2015 Incoherent Fourier ptychographic photography using structured light *Photonics Res.* **3** 19–23
- [6] Gustafsson M G 2000 Surpassing the lateral resolution limit by a factor of two using structured illumination microscopy *J. Microsc.* **198** 82–7
- [7] Gustafsson M G 2005 Nonlinear structured-illumination microscopy: wide-field fluorescence imaging with theoretically unlimited resolution *Proc. Natl Acad. Sci. USA* **102** 13081–6
- [8] Gustafsson M G, Shao L, Carlton P M, Wang C, Golubovskaya I N and Cande W Z *et al* 2008 Three-dimensional resolution doubling in wide-field fluorescence microscopy by structured illumination *Biophys. J.* **94** 4957–70
- [9] Heintzmann R and Gustafsson M G 2009 Subdiffraction resolution in continuous samples *Nat. Photonics* **3** 362–4
- [10] Kner P, Chhun B B, Griffis E R, Winoto L and Gustafsson M G 2009 Super-resolution video microscopy of live cells by structured illumination *Nat. Methods* **6** 339–42
- [11] Mudry E, Belkebir K, Girard J, Savatier J, Le Moal E and Nicoletti C *et al* 2012 Structured illumination microscopy using unknown speckle patterns *Nat. Photonics* **6** 312–5

- [12] Jost A and Heintzmann R 2013 Superresolution multidimensional imaging with structured illumination microscopy *Annual Rev. Mater. Res.* **43** 261–82
- [13] Min J, Jang J, Keum D, Ryu S-W, Choi C and Jeong K-H *et al* 2013 Fluorescent microscopy beyond diffraction limits using speckle illumination and joint support recovery *Scientific Reports* **3**
- [14] So P T C, Kwon H-S and Dong C Y 2001 Resolution enhancement in standing-wave total internal reflection microscopy: a point-spread-function engineering approach *J. Opt. Soc. Am.* **18** 2833–45
- [15] Ou X, Zheng G and Yang C 2014 Embedded pupil function recovery for Fourier ptychographic microscopy *Opt. Exp.* **22** 4960–72
- [16] Gustafsson M G, Shao L, Carlton P M, Wang C R, Golubovskaya I N and Cande W Z *et al* 2008 Three-dimensional resolution doubling in wide-field fluorescence microscopy by structured illumination *Biophys. J.* **94** 4957–70
- [17] Thibault P and Menzel A 2013 Reconstructing state mixtures from diffraction measurements *Nature* **494** 68–71
- [18] Batey D J, Claus D and Rodenburg J M 2014 Information multiplexing in ptychography *Ultramicroscopy* **138** 13–21

Fourier Ptychographic Imaging

A MATLAB® tutorial
Guoan Zheng

Chapter 5

Summary and outlook

We have reviewed and discussed the Fourier ptychography framework and its recent developments in various imaging settings. In particular, we have provided several simulation examples for implementing the FP concept in different forms, including the original FP recovery scheme (sections 2.1 and 2.2), the aberration-correction scheme (section 2.3), the state-multiplexed scheme (section 2.6), the pattern-illuminated FP scheme (section 4.1), the 4-frame resolution-doubling scheme (section 4.2), and the multiplexed structured illumination scheme (section 4.3). We have also discussed the experimental implementation and different imaging modalities of FP.

The FP framework may find applications in the following areas.

- 1) The coherent FP imaging platform may find applications in digital pathology [1], high-throughput rare cell screening [2], and automatic blood analysis [3]. In particular, this platform is able to achieve both large field of view and high resolution at the same time. It may provide a solution for digital pathology which would free pathologists from manually moving the sample using the microscope stage [4].
- 2) The coherent FP imaging platform is also capable of recovering the quantitative phase information of specimens, which can be used for cell culture monitoring or imaging label-free biological samples [5].
- 3) The epi-illuminated FP platform can be used for surface inspection, with a long working distance and a resolution better than the diffraction limit of the employed optics [6]. It can also be used in endoscopy platform for wide-field, high-resolution reflective imaging [7].
- 4) The darkfield FP platform can be used for high-throughput, high-resolution imaging applications where low-frequency information is not needed for characterizing the object, such as in wafer inspection.
- 5) Since FP is able to recover both the aberrations and the high-resolution object images, we envision its applications in characterizing unknown optical aberrations of lenses [8–10].

- 6) The aperture-scanning FP scheme can be used for 3D holographic imaging. By scanning the entire camera to different positions it may also find applications in remote sensing and its final achievable resolution is determined by how far we can translate the camera, not by the size of camera aperture [11].
- 7) For incoherent imaging settings, the pattern-illuminated FP scheme can be used for super-resolution fluorescence microscopy with speckle illumination [12]. It is possible to jointly recover the super-resolution object image and the sample-induced optical aberrations at the same time.
- 8) We can also use the pattern-illuminated FP scheme for reducing the number of image acquisitions in structured illumination microscopy [13]. As such, we can reduce the phototoxicity of the biological sample in a fluorescence microscopy experiment.
- 9) By adopting the multi-state modeling concept to the incoherent imaging setting, we can develop a multiplexed scheme to improve the spatial resolution and recover higher dimensional information at the same time [14]. This multiplexed structured illumination scheme may find applications in general incoherent imaging settings where higher dimensional data is mixed in 2D image measurements. In particular, if we can properly model the interaction between different incoherent modes of the sample, we can use this scheme to image 3D diffused sample.

From the technology point of view, we have the following directions for enriching and improving the FP framework.

- 1) The developments in real-space ptychography can be directly translated into the FP imaging platforms. Spectrum-multiplexing FP [15–18] and multi-slice FP [19–22] are two good examples to this end. We envision the development of single-shot FP based on the recent demonstration in real-space ptychography [23].
- 2) To further improve the imaging throughput, a better illuminator design may be needed. We can, for example, combine the strategies of the LED-array approach and the LCD-modulation approach to increase the photon budget and maintain a good spatial coherence.
- 3) For incoherent imaging settings, current developments are based on 2D image recovery [12, 24]. We can model the sample and illumination patterns in 3D in the FP recovery process.
- 4) The original concept of real-space ptychography comes from electron microscopy. We believe that the FP scheme can also be applied to transmission electron microscopy. For example, we can scan the aperture at the back focal plane to perform aperture-scanning FP imaging.
- 5) Following the same logic, FP can be useful for x-ray microscopy as well. System aberrations of x-ray optics can be corrected in the FP recovery process.

In summary, FP transforms the general challenge of high-throughput, high-resolution imaging from one that is coupled to the physical limitations of the optics to one that is solvable through computation. It is a promising computational framework for both coherent and incoherent imaging settings, with a variety of benefits within and outside microscopy applications.

Bibliography

- [1] Horstmeyer R, Ou X, Zheng G, Willems P and Yang C 2015 Digital pathology with Fourier ptychography *Comput. Med. Imaging Graph.* **42** 38–43
- [2] Williams A, Chung J, Ou X, Zheng G, Rawal S and Ao Z *et al* 2014 Fourier ptychographic microscopy for filtration-based circulating tumor cell enumeration and analysis *J. Biomed. Opt.* **19** 066007
- [3] Chung J, Ou X, Kulkarni R P and Yang C 2015 Counting white blood cells from a blood smear using fourier ptychographic microscopy *PloS one* **10**
- [4] Zheng G, Ou X, Horstmeyer R, Chung J and Yang C 2014 Fourier Ptychographic Microscopy: A Gigapixel Superscope for Biomedicine *Opt. Photonics News* April Issue 26–33
- [5] Ou X, Horstmeyer R, Yang C and Zheng G 2013 Quantitative phase imaging via Fourier ptychographic microscopy *Opt. Lett.* **38** 4845–8
- [6] Guo K, Dong S and Zheng G 2016 Fourier Ptychography for Brightfield, Phase, Darkfield, Reflective, Multi-slice, and Fluorescence Imaging *IEEE J. Select. Topics Quant. Electr.* at press
- [7] Pacheco S, Zheng G and Liang R 2016 Reflective Fourier ptychography *J. Biomed. Opt.* **21** 026010
- [8] Bian Z, Dong S and Zheng G 2013 Adaptive system correction for robust Fourier ptychographic imaging *Opt. Exp.* **21** 32400–10
- [9] Ou X, Zheng G and Yang C 2014 Embedded pupil function recovery for Fourier ptychographic microscopy *Opt. Exp.* **22** 4960–72
- [10] Konda P C, Taylor J M and Harvey A R 2015 High-resolution microscopy with low-resolution objectives: correcting phase aberrations in Fourier ptychography in *SPIE* 96300X–8
- [11] Dong S, Horstmeyer R, Shiradkar R, Guo K, Ou X and Bian Z *et al* 2014 Aperture-scanning Fourier ptychography for 3D refocusing and super-resolution macroscopic imaging *Opt. Exp.* **22** 13586–99
- [12] Dong S, Nanda P, Shiradkar R, Guo K and Zheng G 2014 High-resolution fluorescence imaging via pattern-illuminated Fourier ptychography *Opt. Exp.* **22** 20856–70
- [13] Dong S, Liao J, Guo K, Bian L, Suo J and Zheng G 2015 Resolution doubling with a reduced number of image acquisitions *Biomed. Opt. Exp.* **6** 2946–52
- [14] Dong S, Guo K, Jiang S and Zheng G 2015 Recovering higher dimensional image data using multiplexed structured illumination *Opt. Exp.* **23** 30393–8
- [15] Thibault P and Menzel A 2013 Reconstructing state mixtures from diffraction measurements *Nature* **494** 68–71
- [16] Batey D J, Claus D and Rodenburg J M 2014 Information multiplexing in ptychography *Ultramicroscopy* **138** 13–21
- [17] Dong S, Shiradkar R, Nanda P and Zheng G 2014 Spectral multiplexing and coherent-state decomposition in Fourier ptychographic imaging *Biomed. Opt. Exp.* **5** 1757–67

- [18] Tian L, Li X, Ramchandran K and Waller L 2014 Multiplexed coded illumination for Fourier Ptychography with an LED array microscope *Biomed. Opt. Exp.* **5** 2376–89
- [19] Maiden A M, Humphry M J and Rodenburg J M 2012 Ptychographic transmission microscopy in three dimensions using a multi-slice approach *J. Opt. Soc. America A* **29** 1606–14
- [20] Godden T, Suman R, Humphry M, Rodenburg J and Maiden A 2014 Ptychographic microscope for three-dimensional imaging *Opt. Exp.* **22** 12513
- [21] Li P, Batey D J, Edo T B and Rodenburg J M 2015 Separation of three-dimensional scattering effects in tilt-series Fourier ptychography *Ultramicroscopy* **158** 1–7
- [22] Tian L and Waller L 2015 3D intensity and phase imaging from light field measurements in an LED array microscope *Optica* **2** 104–11
- [23] Sidorenko P and Cohen O 2016 Single-shot ptychography *Optica* **3** 9–14
- [24] Dong S, Nanda P, Guo K, Liao J and Zheng G 2015 Incoherent Fourier ptychographic photography using structured light *Photonics Res.* **3** 19–23
- [25] Guo K, Liao J, Bian Z, Heng X and Zheng G 2015 InstantScope: a low-cost whole slide imaging system with instant focal plane detection *Biomed. Opt. Exp.* **6** at press